

**NEW METHODS OF CHARACTERIZING
SPATIO-TEMPORAL PATTERNS IN LABORATORY
EXPERIMENTS**

A Thesis
Presented to
The Academic Faculty

by

Hüseyin Kurtuldu

In Partial Fulfillment
of the Requirements for the Degree
Doctor of Philosophy in the
School of Physics

Georgia Institute of Technology
December 2010

**NEW METHODS OF CHARACTERIZING
SPATIO-TEMPORAL PATTERNS IN LABORATORY
EXPERIMENTS**

Approved by:

Dr. Michael F. Schatz, Advisor
School of Physics
Georgia Institute of Technology

Dr. Konstantin Mischaikow
Department of Mathematics
Rutgers University

Dr. Daniel Goldman
School of Physics
Georgia Institute of Technology

Dr. James L. Gole
School of Physics
Georgia Institute of Technology

Dr. Predrag Cvitanović
School of Physics
Georgia Institute of Technology

Date Approved: July 27, 2010

To my Family.

ACKNOWLEDGEMENTS

First and foremost I would like to thank my thesis advisor Michael F. Schatz for giving me the opportunity to work in his lab and for his generous support and guidance whenever I needed. Many thanks to Adam Perkins and Serdar Ozdemir for their friendship and lively discussions we had over the years about life and research. Last but not least I would like to thank my family for their continuous and inexhaustible support through the years.

TABLE OF CONTENTS

DEDICATION	iii
ACKNOWLEDGEMENTS	iv
LIST OF TABLES	vii
LIST OF FIGURES	ix
SUMMARY	xv
I INTRODUCTION	1
II EXPERIMENTAL AND CHARACTERIZATION TECHNIQUES	5
2.1 Apparatus	5
2.2 Data Visualization and Acquisition	8
2.3 Computational Homology	12
2.4 Karhunen-Loève Decomposition	17
2.5 Structure Factor	19
2.6 Curvature and Obliqueness	24
III DEPARTURES FROM THE OBERBECK-BOUSSINESQ APPROXIMATION	28
3.1 Introduction	28
3.2 Experiments	29
3.3 Homology Analysis	32
3.4 Other Analysis Methods	41
3.5 Numerical Simulations	45
3.6 Discussion	45
IV CHARACTERIZATION OF DYNAMICS	50
4.1 Extensive Chaos in Rayleigh-Bénard convection	50
4.1.1 Introduction	50
4.1.2 Experiments	51
4.1.3 Homology Dimension	52

4.1.4	Karhunen-Loève Decomposition Dimension	54
4.1.5	Extensive Scalings	57
4.2	Transition to Spiral Defect Chaos	61
4.2.1	Introduction	61
4.2.2	Other Analysis Methods	62
4.2.3	Information Entropy	63
V	CONCLUSION	70
APPENDIX A	NONDIMENSIONALIZED BOUSSINESQ EQUATIONS .	74
APPENDIX B	GAS PROPERTIES	77
REFERENCES	86

LIST OF TABLES

3.1	NOB effects with differing strengths are studied systematically by performing experiments under different conditions, E-I, E-II, E-III, and E-IV. As shown in the Table, each condition is characterized by a choice of fluid and lateral boundary along with key parameter values including the cell depth d , the aspect ratio Γ , the pressure P , the critical temperature difference across the cell ΔT_c , the vertical diffusion time $t_v = d^2/\kappa$, the Prandtl number σ , and the coefficients γ_i^c used to calculate the Busse parameter Q^c at onset.	30
3.2	Key conditions are shown for experimental runs R-I, R-II, R-III, R-IV, R-V and R-VI to probe NOB effects in SDC. Q is estimated from Eq. 3.1 with the fluid properties (see Appendix) evaluated at ϵ values. The number of images N is acquired in experiments in observation times t_{obs} in units of the horizontal diffusion time t_h ($t_h = \Gamma^2 t_v$). . . .	32
4.1	SDC data taken in three different experimental cells at $\epsilon = 0.8$ with the aspect ratio $\Gamma = r/d$ (radius to depth ratio), the fluid and the sidewall used. Pr is the Prandtl number and t is the observation time in units of the horizontal diffusion time $t_h = \Gamma^2 t_v$. The vertical diffusion time t_v is order of seconds. N is the number of images captured for computations.	52
B.1	Coefficients a_{ij}^λ for carbon dioxide are obtained from a fit of the polynomial in Eq.(B.10) to the data in Ref. [54] with 31 points. The max and mean percent deviations between the data and the conductivities acquired from Eq.(B.10) are 0.054% and 0.014%, respectively.	80
B.2	Coefficients a_{ij}^μ for carbon dioxide are obtained from a fit of the polynomial in Eq.(B.11) to the data in Ref. [54] with 39 points. The max and mean percent deviations between the data and the shear viscosities acquired from Eq.(B.11) are 0.493% and 0.138%, respectively.	80
B.3	Thermophysical Properties of CO ₂ at given temperature and pressure.	82
B.4	Coefficients c_{ik} are obtained from a fit of the polynomial in Eq.(B.15) to the virial coefficient data in Ref. [23].	83
B.5	Coefficients a_{ij}^λ for sulfur hexafluoride are obtained from a fit of the polynomial in Eq.(B.10) to the data in Ref. [51] and Ref. [3] with 33 points. The max and mean percent deviations between the combined data and the conductivities acquired from Eq.(B.10) are 1.651% and 0.425%, respectively.	84

B.6	Coefficients a_{ij}^μ for sulfur hexafluoride are obtained from a fit of the polynomial in Eq.(B.11) to the data in Ref. [34] and Ref. [55] with 174 points. The max and mean percent deviations between the combined data and the shear viscosities acquired from Eq.(B.11) are 0.161% and 0.028%, respectively.	84
B.7	Thermophysical Properties of SF ₆ at given temperature and pressure.	85

LIST OF FIGURES

1.1	A schematic illustration of onset in Rayleigh-Bénard convection where a thin layer of fluid is confined between two parallel plates. $T_b = T_t + \Delta T$ and T_t are the bottom and the top plate temperatures, respectively. The onset of fluid motion, as illustrated, occurs at sufficiently large temperature difference ΔT_c . The convection pattern at the onset appears in the form of straight hot and cold rolls as the cell is viewed from above.	2
2.1	A schematic diagram of the apparatus used in convection experiments.	7
2.2	A schematic diagram of the shadowgraph technique.	8
2.3	Shadowgraph images captured at increasing ϵ values in an experiment performed with SF_6 in a cylindrical cell of aspect ratio $\Gamma = 30$; (a) $\epsilon = 0.2$, (b) $\epsilon = 0.4$, (c) $\epsilon = 0.6$ (spiral defect chaos sets in), (d) $\epsilon = 0.8$, (e) $\epsilon = 1.0$, and (f) $\epsilon = 2.0$. Dark and bright regions in images represent hot and cold flows, respectively.	9
2.4	Shadowgraph images captured at $\epsilon = 1.0$ demonstrate the spatio-temporal chaotic behavior. The images are separated by about $10t_v$, where t_v is the vertical diffusion time and is about $1.8s$	10
2.5	The effective optical distance z_1 is shown as a function of D (the distance between the camera lens and the convex lens) for different focal lengths f of the camera lens. Shadowgraph images are captured for (a) $f = 35mm$, (b) $f = 50mm$, and (c) $f = 80mm$ by fixing $D \approx 50cm$	11
2.6	Homology yields (a) $\beta_0 = 1, \beta_1 = 1, \beta_2 = 0$ for open ended cylinder, (b) $\beta_0 = 1, \beta_1 = 0, \beta_2 = 1$ for the hollow sphere and (c) $\beta_0 = 1, \beta_1 = 2, \beta_2 = 1$ for the torus. The surface of each shape defines the topological space of interest.	14
2.7	(a) A shadowgraph image captured at $\epsilon = 0.8$ in an experiment performed with SF_6 . Dark and bright regions in the image represent hot and cold flows, respectively. Two distinct binary images for (b) cold and (c) hot flows are obtained by thresholding the image at the median intensity value. Binary images defines cold X_c and hot X_h topological spaces shown by white (non-zero) pixels. Zero pixels are disregarded in computations. Computational homology yields the number of distinct components defined by the zeroth betti number for cold flows (d) $\beta_{0c} = 54$ and for hot flows (e) $\beta_{0h} = 29$, and the number of holes for cold flows (f) $\beta_{1c} = 1$ and for hot flows (g) $\beta_{1h} = 9$. The distinct components are shown in different colors and the holes are colored in red.	16

2.8	The mean Betti numbers are shown as a function of the effective optical distance z_1 of the shadowgraph system in the experiment performed at $\epsilon = 2.0$ with \mathbf{CO}_2 . Each data point corresponds to a time average of Betti numbers from analysis of 500 images.	17
2.9	$y_k(t_j)$ associated with λ_k for $\epsilon = 0.375$ (top) and $\epsilon = 0.875$ (bottom). $y_1(t_j)$, $y_{100}(t_j)$ $y_{500}(t_j)$ corresponding to the largest, the 100th and 500th largest eigenvalues, respectively.	20
2.10	Time averaged structure function $S(\mathbf{k})$, acquired from $T = 100$ images, is shown for (a) $\epsilon = 0.4$ and (b) $\epsilon = 0.8$. Wave number components are given in units of $1/d$, where d is the depth of the convection cell. .	22
2.11	Examples of Fourier filters used to preprocess shadowgraph images: (a) a Gaussian filter $G(k)$ centered at $k \equiv k = 0$ with a variance $\sigma = 6/d$ where d is the depth of the convection cell, (b) a Hann Filter $H(k)$ produced by a combination of $H_1(k)$ in Eq. 2.5 for $k_1 = 0.1/d$, $k_2 = 1/d$ and $H_2(k)$ in Eq. 2.5 for $k_1 = 4.5/d$, $k_2 = 12/d$	23
2.12	Skeleton-line representations extracted from the pattern in Fig. 2.7(a) are shown for (a) cold and (b) hot flows. The points, where the unit normal vector \mathbf{n} is undefined, are removed from the representations. The distinct roll pieces are shown in different colors; the black points indicate the end points of the pieces. The curvature \mathcal{C} is computed along the points on (c) cold and (d) hot roll pieces. In (e) and (f), the roll pieces in (a) and (b) are greyscale coded based on the average roll curvature on each piece.	26
2.13	The unit sidewall (\mathbf{s}) and roll (\mathbf{n}) normal vectors, in a narrow band next to the sidewall, are shown for cold flow representation in Fig. 2.7(a). A square region is magnified for better visualization of the vectors. The closest pairs of \mathbf{n} (shown in blue) and \mathbf{s} (shown in red) vectors are identified. (Their locations are shown with open black circles.) For more accurate measurement, an additional closest 8 pairs of vectors are determined. (The pairs are connected with yellow lines.) The averaged obliqueness is measured via the dot product of the chosen vectors \mathbf{s} and \mathbf{n}	27
3.1	Shadowgraph patterns at fixed $\epsilon = 0.8$ and different Q illustrate that variations in NOB effects are indistinguishable by eye. The images are shown for experimental runs (a) R-I, (b) R-II, (c) R-III, and (d) R-IV (Tab. 3.2). Dark and bright regions in images represent hot and cold flows, respectively. Homology computations yield the following set of Betti numbers for these patterns $\{\beta_{0c}, \beta_{0h}, \beta_{1c}, \beta_{1h}\}$; (a) $\{54, 29, 1, 9\}$, (b) $\{42, 28, 3, 8\}$, (c) $\{43, 34, 0, 4\}$, (d) $\{43, 44, 4, 4\}$ (for details see Section 2.3).	33
3.2	Time series of the zeroth Betti numbers are shown for (a) R-IV (b) R-I.	33

3.3	Topological asymmetries increase with the Busse parameter Q at constant ϵ . (a) The mean zeroth Betti numbers $\langle\beta_{0c}\rangle$ (filled circles) and $\langle\beta_{0h}\rangle$ (open circles); (b) the mean first Betti numbers $\langle\beta_{1c}\rangle$ (filled diamonds) and $\langle\beta_{1h}\rangle$ (open diamonds) are calculated from the time series of Betti numbers for the experimental runs (Tab. 3.2) at $\epsilon = 0.8$. In computations, 5000 images are analyzed for the runs R-I, R-III, and R-IV while 15000 images are used in computations for the run R-II.	34
3.4	Temporal convergence of the mean zeroth Betti number in R-II. $\langle\beta_{0c}\rangle$ (filled triangles) and $\langle\beta_{0h}\rangle$ (open triangles) are shown as a function of observation time. Each data point corresponds to an average of Betti numbers from analysis of 3000 images. The results for the original data of 15000 images in $50t_h$ (Fig. 3.3(a)) are shown with circles.	35
3.5	Robustness of the measurement of the mean zeroth Betti number with respect to wave number distribution. The zeroth Betti numbers, $\langle\beta_{0c}\rangle$ and $\langle\beta_{0h}\rangle$, computed for the images filtered with a two dimensional Gaussian filter of variance η in units of k . Computations are performed for two data sets, R-I (circles) and R-IV (squares). Filters with $\eta(k = 2.45)$ and $\eta(k = 7.83)$ keep %59 and %95 of the total power, respectively. k is measured in units of d^{-1}	36
3.6	Scaling of the topological symmetry and asymmetry with system size. The zeroth mean Betti numbers are shown as a function of area of circular subregions of radius r (r is in units of the cell depth d). In run R-II ($Q = 1.75$) indicated by circles, $\langle\beta_{0c}\rangle$ and $\langle\beta_{0h}\rangle$ are obtained by analyzing 15000 images in increasing size of subregions formed by an increment d in r . In R-IV ($Q = 0.65$) indicated by squares, 5000 images are used to calculate the zeroth Betti numbers for five subregions of different sizes ($r = 5d, 15d, 20d, 25d, 30d$). (b) The order parameter $\langle\Delta\beta_0\rangle = \langle\beta_{0c} - \beta_{0h}\rangle$ is shown as a function of subregion area for R-II (closed symbols) and R-IV (open symbols).	38
3.7	Topological asymmetries grow with the Rayleigh number. (a) $\langle\beta_{0c}\rangle$ (filled symbols) and $\langle\beta_{0h}\rangle$ (empty symbols) are shown as a function of ϵ for the run R-V (circles) and R-VI (squares). Each data point is obtained by averaging the Betti numbers from analysis of 5000 images corresponding to an observation time of $10t_h$ at each ϵ (b) The zeroth Betti numbers are shown as a function of Q estimated at the ϵ values in R-V and R-VI.	39
3.8	The zeroth Betti number data for <i>all</i> our experimental runs (Tab. 3.2) are represented by a single graph of $\langle\Delta\beta_0\rangle = \langle\beta_{0c} - \beta_{0h}\rangle$ plotted solely as a function of the NOB parameter Q . Data are shown for experimental runs R-I (open diamond), R-II (open triangle), R-III (open square), R-IV (open circle), R-V (closed circles) and R-VI (closed squares).	40

- 3.9 The analysis based on two-dimensional discrete Fourier transform produce nearly identical results for the patterns, on which NOB effects are varied. (a) The azimuthally and time-averaged structure factor $S(\mathbf{k})$ corresponding to the runs at $\epsilon = 0.8$. (b) the mean wave number $\langle k \rangle$ as a function of Q , the vertical bars extend by $\pm \xi^{-1}$ 42
- 3.10 Measures calculated from the texture of the patterns for the runs at $\epsilon = 0.8$ show no distinction between cold and hot flow patterns as a function of Q . The number of images used at each point is given in Tab. 3.2. The subscripts c and h indicates the obtained quantities for cold and hot flows, respectively. (a) The time averaged radius of curvatures $\langle \mathcal{R} \rangle$ calculated for full system size and for a circular region of radius $r = 20d$ inside the cell (b) the time averaged angle of obliqueness $\langle \theta \rangle$ (c) the time averaged roll length $\langle L \rangle$ shown for full system size and for a circular region of radius $r = 20d$ 43
- 3.11 Simulations in a square domain are shown for the midplane temperature fields (a,b) and the midplane vertical velocity fields (c,d) at $\epsilon = 1.4$. In NOB simulations (a-c), all the γ_i^c are retained, while in OB simulations (b-d), all the γ_i^c are set to 0. The coefficients are $\gamma_0^c = 0.1714$, $\gamma_1^c = -0.2118$, $\gamma_2^c = 0.2836$, $\gamma_3^c = 0.1905$, $\gamma_4^c = 0.0624$ corresponding to $Q = 4.2$. The side length is equal to 16 times the pattern wavelength at onset. Computations, where the threshold is chosen as the median value of temperature or velocity field at each image, yield following set of betti numbers $\{\beta_{0c}, \beta_{0h}, \beta_{1c}, \beta_{1h}\}$; (a) $\{44, 12, 0, 22\}$, (b) $\{22, 22, 6, 6\}$, (c) $\{42, 14, 2, 19\}$, (d) $\{20, 21, 3, 3\}$ 46
- 3.12 The temperature fields (a-b) and the vertical velocity fields (c-d) at $z = 0$ and $z = \pm 0.25$ from OB and NOB simulations are used to obtain the mean zeroth Betti numbers $\langle \beta_0 \rangle$ (a-c) and the mean first Betti numbers $\langle \beta_1 \rangle$ (b-d) for cold and hot flows. Each data point is obtained by averaging the Betti numbers from analysis of 400 images corresponding to an observation time of $200t_v$. The midplane, the top and the bottom boundaries of the cell is located at $z = 0$, $z = 0.5$ and $z = -0.5$, respectively. 47
- 3.13 Contrary to convection in gases, patterns in liquids with negative Q have the asymmetry $\beta_{0h} > \beta_{0c}$, $\beta_{1c} > \beta_{1h}$. For instance, temperature fields from a NOB simulation in a circular cell of water are shown at (a) $\epsilon = 0.6$ and (b) $\epsilon = 1.0$, after [40]. All coefficients, $\gamma_0^c = 0.0036$, $\gamma_1^c = 0.2122$, $\gamma_2^c = -0.2725$, $\gamma_3^c = 0.0352$, and $\gamma_4^c = -0.0013$ corresponding to $Q^c = -1.84$, are retained. The diameter of the cell is equal to 16 times the pattern wavelength at onset. Computations yield the following set of Betti numbers $\{\beta_{0c}, \beta_{0h}, \beta_{1c}, \beta_{1h}\}$: (a) $\{11, 37, 6, 0\}$, (b) $\{5, 48, 10, 1\}$. 48

4.1	Shadowgraph patterns of SDC at $\epsilon = 0.8$. Bright and dark regions represent hot and cold flows respectively. (a)-(b) Two images from D-I separated by about $10t_h$, (c) from D-II and (d) from D-III. The median value of intensity in an image is used as a threshold value to form two distinct binary images that represent topological spaces for hot X_h and cold flows X_c , respectively. Homology, for instance, yields the following topological states for the images, $\{\beta_{0c}, \beta_{1c}, \beta_{0h}, \beta_{1h}\}$: (a) $\{64, 2, 29, 13\}$, (b) $\{65, 4, 36, 17\}$, (c) $\{42, 3, 28, 8\}$ and (d) $\{43, 4, 44, 4\}$	53
4.2	Probability distribution of CH states defined by $\{\beta_{0c}, \beta_{1c}, \beta_{0h}, \beta_{1h}\}$ is obtained from homology analysis of 100000 shadowgraph images in data set D-I. ($\sum_k p_k = 1$.) The first largest 1814 probabilities define 70% of the total probability, i.e, $D_{CH} = 1814$ for $f = 0.7$ (Eq. 4.1).	54
4.3	Eigenvalue spectrum is obtained from Fourier based KLD analysis applied on 100000 shadowgraph images in data set D-I. ($\sum_m \lambda_m = 1$.) The first largest 806 eigenvalues define 70% of the spectrum, i.e, $D_{KLD} = 806$ for $f = 0.7$ (Eq. 4.3).	55
4.4	The cumulative D_{KLD} (for $f = 0.7$) obtained from conventional KLD (dashed line) and fourier based KLD (solid line) is shown as a function of the number of images k used in computations. The image data is created by rotating a single shadowgraph image by increments of $\Delta\theta = 2\pi/180$	56
4.5	The cumulative D_{KLD} (for $f = 0.7$) acquired from conventional KLD (open circles) and Fourier based KLD (closed circles) are shown as a function of time. The red dashed line is the curve fit $D_{KLD} = D_\infty + ae^{-bt/t_h}$ ($a = -67.14, b = -0.0657$) for conventional KLD. The asymptotic value $D_\infty = 100.2$ for the conventional KLD is shown by the solid red line.	56
4.6	Extensive Scalings of D_{CH} and D_{KLD} for increasing subsystem sizes are obtained by computational homology (a) and a modified KLD algorithm based on a Fourier method (b), respectively for fraction $f = 0.7$ in D-I. The number of images, at given observation times, used at each data point in computations is labeled. The linear lines are drawn to guide the extensivities to eye. Choosing f very close to 1 may include experimental errors, whereas choosing it too small may exclude necessary modes and states necessary to describe the dynamics. But, for the range $0.5 \leq f \leq 0.9$, extensive scalings of dimensions normalized by the maximum dimension at each f nearly fall on a single curve.	58

4.7	The rates of increase ρ estimated from extensive scalings of D_{CH} (open symbols) and D_{KLD} (closed symbols) are shown as a function of r/Γ to indicate the sidewall effects in the experiments, D-I (squares), D-II (circles), D-III (diamonds), at $\epsilon = 0.8$. The number of images used for computations in D-II and D-III is given in Table 4.1. Also, ρ as dimension per area is obtained from conventional KLD algorithm (asterisks) by sampling the data of 10,000 images in D-I with an annular window of inner r and outer $r + 2d$ radius ($5d \leq r$).	59
4.8	Shadowgraph snapshots of convective patterns in the experiment taken at (a) $\epsilon = 0.625$ (below the onset of spiral defect chaos) and (b) $\epsilon = 0.75$ (above the onset of spiral defect chaos).	62
4.9	Angle-time plots of radially-averaged structure function: (a) $\epsilon = 0.375$, (b) $\epsilon = 5$, (c) $\epsilon = 0.625$, (d) $\epsilon = 0.750$, (e) $\epsilon = 0.875$, (f) $\epsilon = 1.0$. The power is greyscale coded with black corresponding to maximum power.	64
4.10	(a) the average roll curvature κ (b) the skewness S_3 and the excess kurtosis K_4 (c) the intermittency fraction F_I , as a function of ϵ detect the transition to SDC.	65
4.11	The 350 first largest probabilities p_i are shown on a logarithmic scale for five different increasing ϵ . 15,000 images corresponding to $50t_h$ have been used in computations at each ϵ .	66
4.12	The 350 first largest eigenvalues λ_k are shown on a logarithmic scale for five different increasing ϵ . 15,000 images corresponding to $50t_h$ have been used in computations at each ϵ .	67
4.13	Information entropies S_{KLD} and S_{CH} are shown as a function of ϵ in the experiments at different f . At each ϵ , 15,000 images recorded in $50t_h$ are used to compute the entropies. The error bars are the statistical standard error based on the eigenvalue spectra and the probability distributions.	68
5.1	A space-time block formed from a time series of binary images for hot flows and a slice taken from the block are shown. The homology for the space-time block yields the number of distinct components ($\beta_{0h} = 32$), the number of tunnels through the block ($\beta_{1h} = 55$), and the number of cavities enclosed ($\beta_{2h} = 10$).	72

SUMMARY

Complex patterns arise in many extended nonlinear nonequilibrium systems in physics, chemistry and biology. Information extraction from these complex patterns is a challenge and has been a main subject of research for many years. We study patterns in Rayleigh-Bénard convection (RBC) acquired from our laboratory experiments to develop new characterization techniques for complex spatio-temporal patterns. Computational homology, a new topological characterization technique, is applied to the experimental data to investigate dynamics by quantifying convective patterns in a unique way. The homology analysis is used to detect symmetry breakings between hot and cold flows as a function of thermal driving in experiments, where other conventional techniques, e.g., curvature and wave-number distribution, failed to reveal this asymmetry. Furthermore, quantitative information is acquired from the outputs of homology to identify different spatio-temporal states. We use this information to obtain a reduced dynamical description of spatio-temporal chaos to investigate extensivity and physical boundary effects in RBC. The results from homological analysis are also compared to other dimensionality reduction techniques such as Karhunen-Loève decomposition and Fourier analysis.

CHAPTER I

INTRODUCTION

Convective flow plays a key role in numerous technological processes and natural phenomena, including the growth of semiconductor materials and the dynamics of the Earth's atmosphere, ocean, and mantle [25]. Rayleigh [47]-Bénard [4, 5] convection of a horizontal fluid layer, confined between two thermally conducting plates and heated from below, is considered a paradigm to investigate the nature of convection, and has motivated numerous numerical and laboratory studies (see for example Ref. [15, 7] and references therein).

In Rayleigh-Bénard convection (RBC), a thin horizontal layer of fluid (convection cell) is confined between two parallel plates, as illustrated in Fig. 1.1, and is heated from below and cooled from above to achieve a temperature gradient ΔT across the layer. The temperature profile across the fluid is linear for small values of ΔT , provided that the thermal conduction of a still fluid is the only way to transport heat in the system. As the temperature difference reaches a critical value ΔT_c , the destabilizing mechanism (buoyancy) overcomes the stabilizing mechanisms (heat and momentum diffusion), and the onset of convection (fluid motion) occurs. The system undergoes a transition from a spatially uniform conduction state to a convection state with spatial variation. The convection pattern of spatial variation is composed of hot (upflow) and cold (downflow) cylindrical rolls. The pattern evolves into more complex configurations as ΔT is increased above the onset.

RBC experiments are described by three dimensionless quantities; the aspect ratio Γ , the Prandtl number σ and the Rayleigh number R . The aspect ratio Γ measures the geometry of the convection cell and is defined by $\Gamma = r/d$, where r is the radius and

d is the depth of a cylindrical convection cell. There are two important characteristic vertical diffusion times in convection; the thermal relaxation time $t_\kappa = d^2/\kappa$ and the viscous relaxation time $t_\nu = d^2/\nu$, where κ is the thermal diffusivity and ν is the kinematic viscosity. The ratio of these times defines the Prandtl number

$$\sigma = \frac{\nu}{\kappa}$$

which measures the relative importance of the temperature advection and the momentum convection terms in the equations governing the fluid motion (see for instance Eq. A.9 in Appendix A). At the onset of convection, a warmer parcel of fluid at

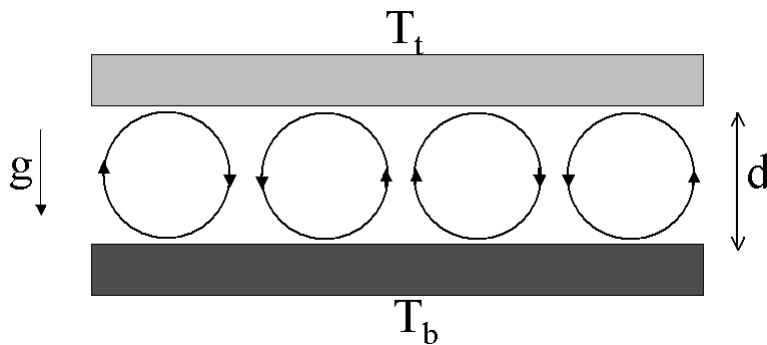


Figure 1.1: A schematic illustration of onset in Rayleigh-Bénard convection where a thin layer of fluid is confined between two parallel plates. $T_b = T_t + \Delta T$ and T_t are the bottom and the top plate temperatures, respectively. The onset of fluid motion, as illustrated, occurs at sufficiently large temperature difference ΔT_c . The convection pattern at the onset appears in the form of straight hot and cold rolls as the cell is viewed from above.

the bottom of the layer rises and exchanges heat conductively with the surrounding fluid, at the same time, a colder parcel of fluid at the top of the layer sinks and exchanges heat with the surrounding fluid (Fig. 1.1). If we consider a parcel of fluid as a spherical fluid particle of radius a moving with a speed V , then there are two forces, namely the buoyant force and the viscous drag force, acting on this sphere in opposite directions. The buoyant force per unit volume is proportional to the acceleration of gravity g and the density gradient $\Delta\rho$. The buoyant force F_b and the viscous force

F_v from Stokes' law are given by

$$F_b = \frac{4\pi}{3}\alpha g\rho\Delta T a^3, F_v = 6\pi\rho\nu Va$$

where ν and α are the kinematic viscosity and the volumetric thermal expansion coefficient, respectively. Therefore, the sphere, at the onset of convection, moves with a speed $V \propto \alpha g\Delta T d^2\nu^{-1}$ (assuming the radius a is on the order of d). The motion of the sphere across the layer is sustainable as long as the time for the sphere to travel the depth d is smaller than the time (t_κ) for a thermal perturbation to travel the same distance d , that is, $V > \kappa/d$. Then, the dimensionless number R ,

$$R = \frac{\alpha g d^3 \Delta T}{\kappa \nu}, \quad (1.1)$$

needs to be larger than a critical constant R_c in order to sustain the convective motion in the cell. R is called the Rayleigh number named after Lord Rayleigh [47]. The exact value of the constant R_c (critical Rayleigh number) can be obtained from a linear stability analysis performed on the equations describing the state of a fluid. This analysis can be found in Ref. [11]. For a solid and perfectly conducting top and bottom plates, the value of R_c is equal to 1707.76 at the onset for any fluid. It is convenient to define a control parameter, a reduced Rayleigh number, by

$$\epsilon = \frac{R - R_c}{R_c}, \quad (1.2)$$

to measure dimensionless distance from the onset [15]. As the system is driven away from the onset, e.g, by increasing the temperature gradient ΔT between the layers, the pattern of convective hot and cold flows becomes time dependent and exhibits complex spatial structure. In particular, as discussed later, for the $\sigma \approx 1$ case and sufficiently large ϵ , the system exhibits a transition to the state known as spiral defect chaos (first observed by Morris et al. [43]), where the convection pattern of hot and cold rolls with a spatio-temporally chaotic behavior is deformed into rotating spirals

and riddled with dislocations, disclinations, and grain boundaries. (For example see Fig. 2.4 in Chapter 2.)

This dissertation is organized as follows: Chapter 2 describes both experimental and characterization techniques used in investigating complex time-dependent patterns in Rayleigh-Bénard convection of compressed gases with $\sigma \approx 1$. The experimental and the optical setups, needed to visualize cold and hot flows and to acquire chaotic data under controlled conditions, are described. This chapter also describes how computational homology is employed to characterize spiral defect chaos patterns. In Chapter 3 homology and alternative characterization techniques are used to study the breakdown of the reflection symmetry about the midplane of the layer. Chapter 4 introduces quantitative measures obtained from computational homology and Karhunen-Loève decomposition to characterize spatio-temporally chaotic dynamics in experiments.

CHAPTER II

EXPERIMENTAL AND CHARACTERIZATION TECHNIQUES

2.1 Apparatus

We measure convective flows experimentally in a horizontal layer of compressed gas cooled from above and heated from below in a cylindrical convection cell. Compressed single phase gases CO_2 and SF_6 are used as convective fluids, bounded by circular lateral walls. The experiments are performed at pressure ranging from 9 – 32 bar and at top and bottom temperatures ranging from 10 – 50 °C. The top and bottom temperatures of the convection cell are controlled within ± 0.02 °C while the pressure is controlled within ± 0.04 bar in experiments. The convective flow patterns are visualized by using the shadowgraph technique that measures the variations in vertically averaged index of refraction.

The experimental apparatus (a similar apparatus is also described in de Bruyn et al. [15]) used to study Rayleigh-Bénard convection in compressed gases is shown in Fig. 2.1. The top and bottom plates need to be highly conductive, relative to the experimental convective fluid, to prevent any horizontal temperature gradient at the top and the bottom layer of the convection cell. On the other hand, one of the plates should be transparent to visible light for shadowgraph measurements. For these reasons, we use a 2.54 cm thick cylindrical sapphire window as the top plate and a 0.6 cm thick cylindrical aluminum as the bottom plate in experiments. The top surface of the aluminum plate is a gold coated mirror of radius 5 cm. The thermal conductivities of the top and the bottom plate are $46 \text{ Wm}^{-1}\text{K}^{-1}$ and $237 \text{ Wm}^{-1}\text{K}^{-1}$, respectively; these conductivities are three orders of magnitude larger

than the thermal conductivities of CO_2 and SF_6 (for example, see Tab. B.3 and Tab. B.7 in Appendix B). The convection cell is bounded by a precisely cut and roughly half of a millimeter thick circular sidewall which is placed and compressed between the plates. The material from which the sidewall is made should be chosen carefully. The mismatch in the thermal conductivities of the sidewall and the fluid causes sidewall forcing in the convective flow as a result of a vertical temperature gradient near the edge of sidewall. We use two different types of sidewalls, filter paper and plastic (polyethersulfone), to study convection with strong and weak sidewall forcing. The thermal conductivities of the paper and of the plastic walls are about a factor of 4 and 10 times larger than the thermal conductivity of the fluid used in experiments, respectively. In order to achieve a temperature gradient across the convection cell, the top layer of the cell is cooled by circulating chilled water over the top surface of the sapphire window, and the bottom layer of the cell is heated by a thin electrical resistive heater placed under the bottom plate. The convection cell is placed inside an aluminum pressure container (Fig. 2.1). Two thermistors for temperature measurements are implanted in the bottom plate and in the top part of the container near the sapphire window. There are three feedthroughs on the container; one of them is for the heater and the thermistor wirings and the other two are for gas inlet and outlet lines. The bottom plate rests on a steel plate mount with the help of four leveling screws. One of the screws is hooked up to the center of the mount in order to compress the sidewall to reach a desired depth. Three screws mounted to a steel plate via three steel balls are used for cell alignment. The alignment is checked by an interferometric technique with a He-Ne laser beam. Based on interferometry, the variation of the depth under pressure is kept less than $5 \mu\text{m}$ along the cell in experiments.

The thin heater (MINCO HK5547R47) is linked to a power supply (KEPCO 0-36V 0-3A) whose output is controlled by sending an analog voltage from a connector

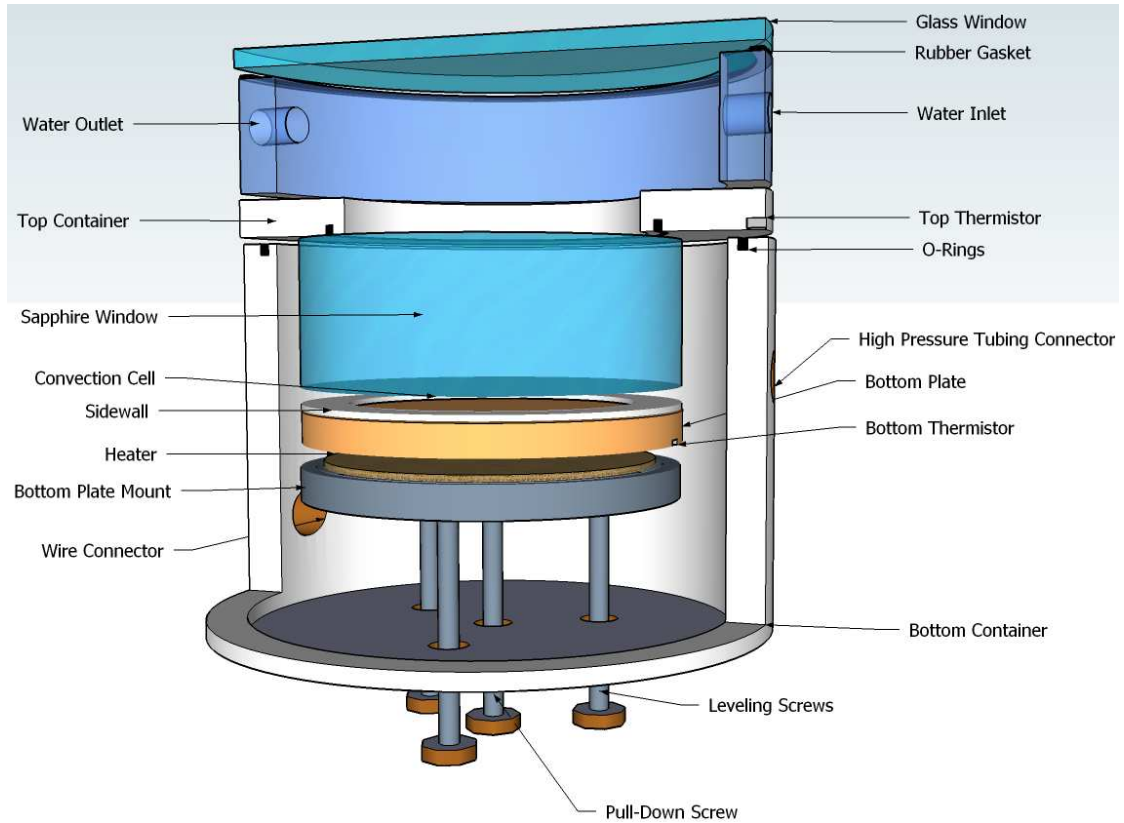


Figure 2.1: A schematic diagram of the apparatus used in convection experiments.

block (NI BNC-2110), controlled by Labview. The connector block is hooked up to a data acquisition card (NI PCI-6014) in the computer. Top and bottom thermistors are connected to a multimeter (HP 34401A) through a time delay relay so that the resistance values of the thermistors can be measured sequentially by sending digital signals from the connector. The resistance is read by Labview through a GPIB interface. A water bath (NESLAB RTE-221) with an analog interface is used to circulate water. The bath interfaced to Labview is calibrated with respect to the top thermistor. The bottom and the top plate temperatures are controlled by control loop feedback mechanisms (PID) implemented in Labview. The temperature difference between the plates is maintained with high precision (within ± 0.02 °C). A small pressure vessel is connected to the container pressure inlet via tubing. The vessel and the container are pressurized from a gas tank with a regulator. A heater attached

to the vessel is used to regulate the pressure fluctuations in the container. A valve, linked to the container pressure outlet through a pressure transducer, can be opened to reduce the container pressure. Another PID controller is implemented to keep the pressure variations inside the cell less than 40 mbar.

2.2 Data Visualization and Acquisition

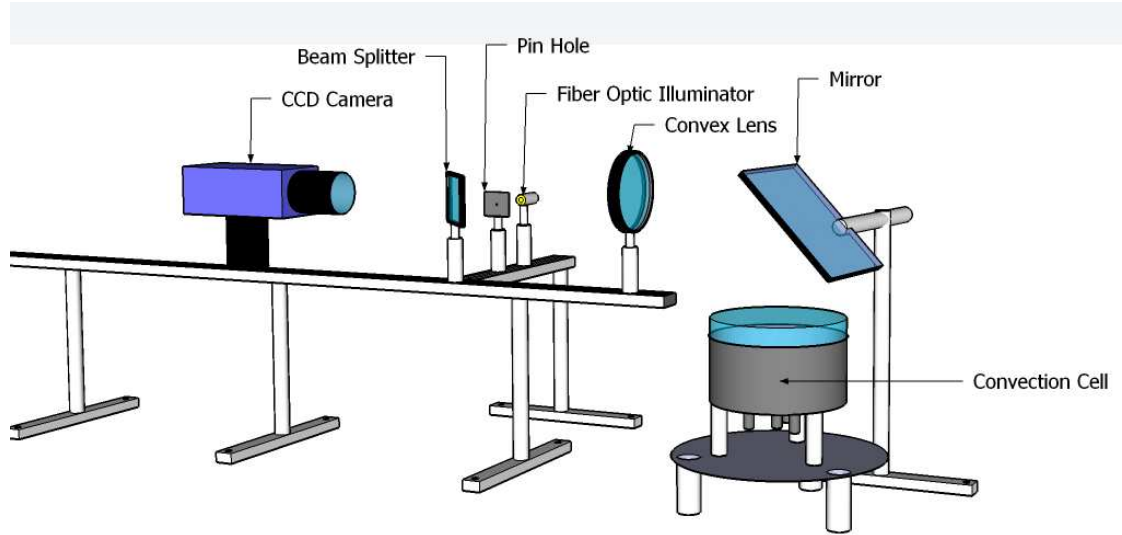


Figure 2.2: A schematic diagram of the shadowgraph technique.

The convective flows in experiments are visualized by the shadowgraph technique [50, 26, 30, 15]. This technique measures the optical non-uniformities due to the variations of the second derivative of the index of refraction, averaged over the thickness of the cell, in the lateral directions. For shadowgraph visualization, collimated light is sent through the fluid in the cell. In the presence of convection, the beam of light is refracted by the hot and cold cylindrical rolls acting as an array of lenses. A two dimensional shadowgraph image describing the convective flow pattern, as the cell is visualized from above, can be captured by imaging the refracted beam of light (for example see sample images in Fig. 2.3 and Fig. 2.4). The shadowgraph setup used in our experiments is shown in Fig. 2.2. A parallel beam of light is generated by

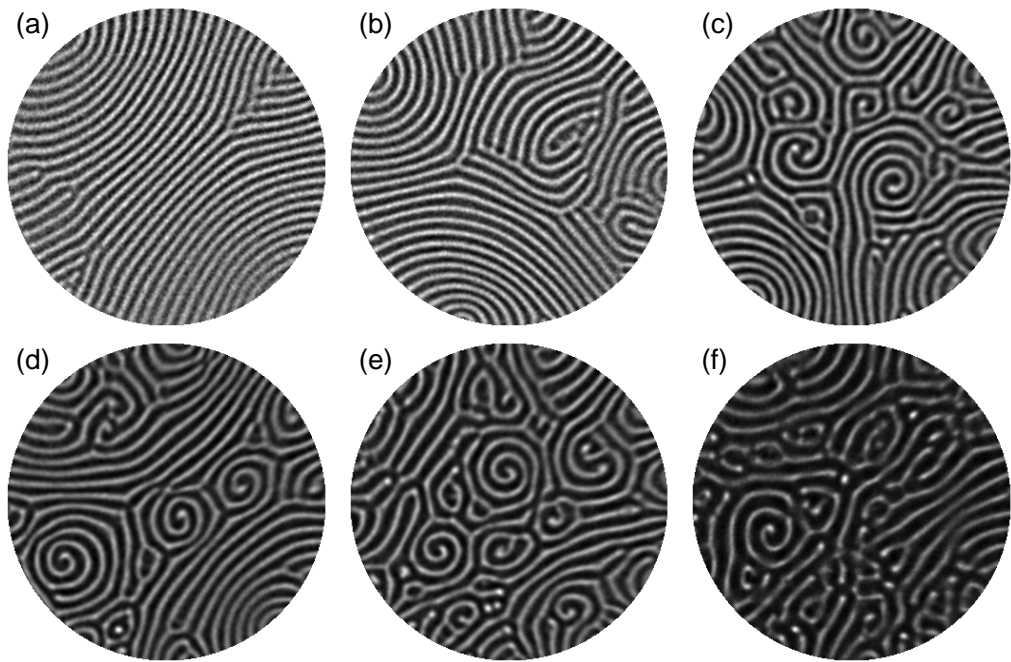


Figure 2.3: Shadowgraph images captured at increasing ϵ values in an experiment performed with SF_6 in a cylindrical cell of aspect ratio $\Gamma = 30$; (a) $\epsilon = 0.2$, (b) $\epsilon = 0.4$, (c) $\epsilon = 0.6$ (spiral defect chaos sets in), (d) $\epsilon = 0.8$, (e) $\epsilon = 1.0$, and (f) $\epsilon = 2.0$. Dark and bright regions in images represent hot and cold flows, respectively.

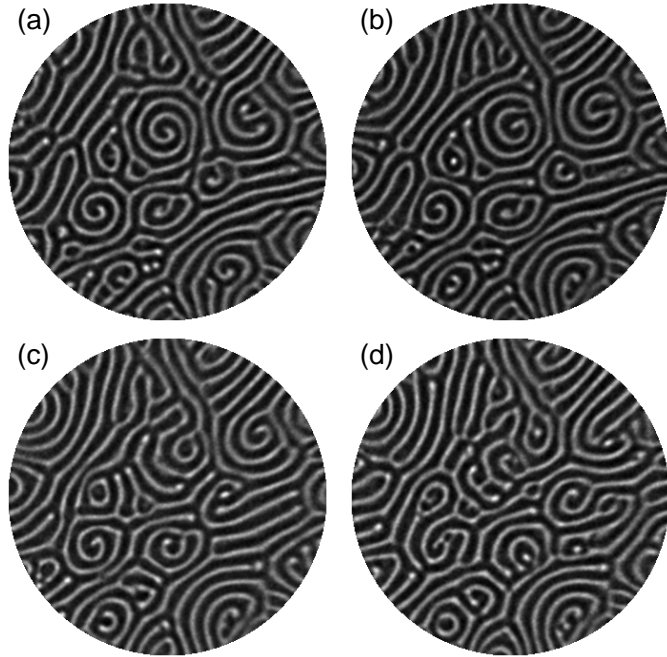


Figure 2.4: Shadowgraph images captured at $\epsilon = 1.0$ demonstrate the spatio-temporal chaotic behavior. The images are separated by about $10t_v$, where t_v is the vertical diffusion time and is about $1.8s$.

a combination of a pinhole and a fiber optic illuminator positioned at the focal length of a convex lens. The collimated light is then sent through the sapphire window into the convection cell. The reflected light from the bottom plate is returned back to the optics and imaged by a CCD camera (DMK 31BU03 1024x768). Hardware triggering of the camera as well as the image resolution and the frame rate are controlled by Matlab. In order to analyze convection under different controlled experimental conditions, the experiments with automated image acquisition are accomplished by the interface between Labview and Matlab.

The shadowgraph measurements can introduce strong nonlinearities, especially for ϵ near or above one, which may affect the visualization of cold and hot flows. The strength of these effects depends on the effective optical distance z_1 [15]. (The distance of the imaging plane from the convection cell.) The distance z_1 can be calculated directly from the optical arrangement in a shadowgraph system [30]. The

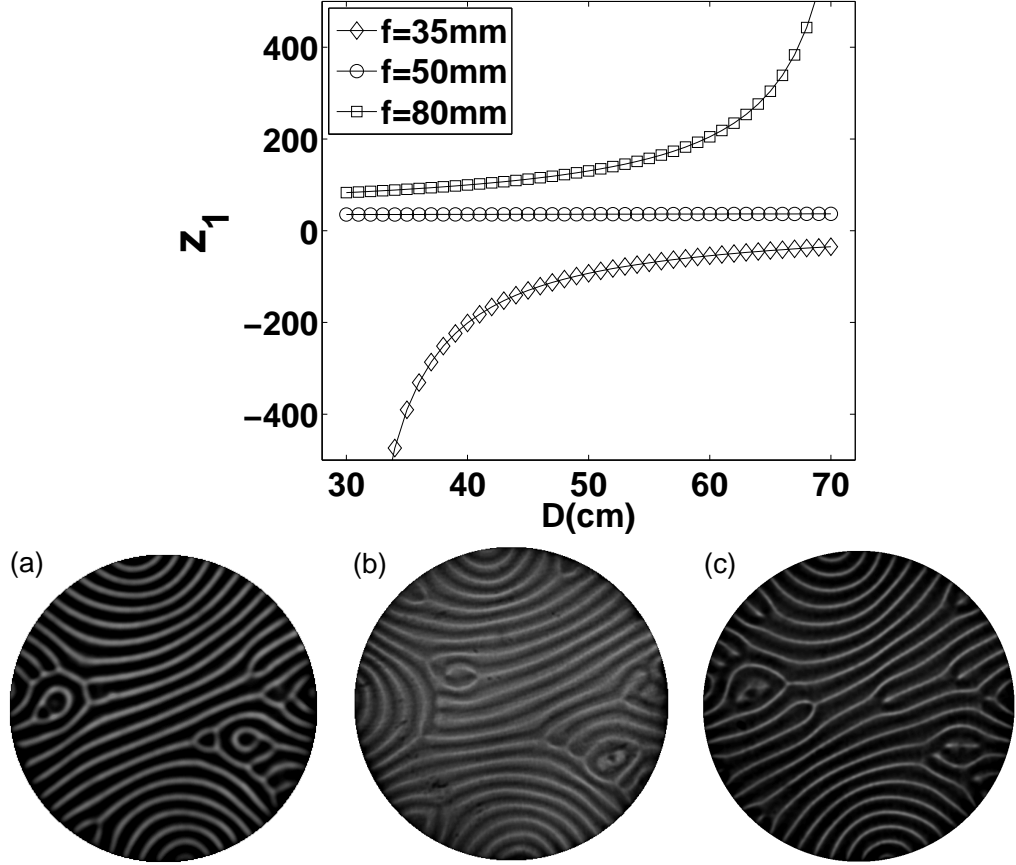


Figure 2.5: The effective optical distance z_1 is shown as a function of D (the distance between the camera lens and the convex lens) for different focal lengths f of the camera lens. Shadowgraph images are captured for (a) $f = 35\text{mm}$, (b) $f = 50\text{mm}$, and (c) $f = 80\text{mm}$ by fixing $D \approx 50\text{cm}$.

optical setup can be arranged in a way that a wide range of z_1 values, as seen in Fig. 2.5, can be obtained by only altering the focal length of the camera lens and the distance between the camera lens and the convex lens. For positive (negative) values of z_1 , hot and cold flows appear as dark (bright) and bright (dark) regions, respectively, in a shadowgraph image.

For onset measurements, the temperature difference ΔT between the plates, below the onset of convection, is increased very slowly at a constant pressure and a constant mean temperature. At each value of ΔT , a time series of images are captured by the camera. The time averaged Fourier power of the images is used to detect any spatial

structure formed within the cell. The critical temperature difference ΔT_c is recorded as soon as the convection is detected by the Fourier signal. The depth of the cell d is calculated from Eq. 1.1 for critical Rayleigh number R_c with the fluid properties (see Appendix B) evaluated at the mean temperature of the cell. The accuracy of the depth measurement (with a mean deviation of less than .1%) is checked with the onset measurements performed at different mean temperatures at the same pressure value.

For different values of the reduced Rayleigh number ϵ (Eq. 1.2), we analyze the convection patterns above onset by recording long time series of shadowgraph images with a spatial resolution of 692×692 pixels at variable frame rates, ranging from .1 to 10 fps. As ϵ is increased by increasing ΔT , the pattern becomes unstable and evolves into more complex and time-dependent flow patterns, as demonstrated by the set of shadowgraph images in Fig. 2.3 and Fig. 2.4. For small ϵ , the convective pattern is composed of curved rolls due to several focus singularities and defects near sidewalls. For larger ϵ some moving defects are observed in the interior regions of the cell along with curved rolls. At a sufficiently large ϵ ($\epsilon = 0.6$), the state of spiral defect chaos is observed.

2.3 Computational Homology

Recent technical advances now make it possible to measure the dynamical behavior of physical systems with high resolution in both space and time. For example, in fluid dynamics, turbulent data are often represented by pixels of a raw image (two or three dimensional) in experiments and by temperature or velocity fields computed at grid points in simulations. The data sets produced by experiments and simulations can be enormous; as a result, characterizing such data sets becomes a significant challenge; therefore, fast and efficient characterization tools are needed.

We investigate characteristics of spatio-temporally chaotic flow patterns in RBC

by performing experiments over a wide range of ϵ values, and by capturing long sequences of shadowgraph images at given values of ϵ . Our data sets often contain hundreds of thousands of images, which takes up a couple of terabytes of disk space. In this section, we introduce a newly developed topological characterization tool called computational homology, which we will use later in the dissertation to analyze efficiently our large experimental data sets. Furthermore, later in this section, we briefly describe some widely used pattern characterization techniques, which we will also use to study convection patterns in our data sets.

Homology, a branch of algebraic topology, is a metric-independent characterization method to measure global geometric properties of complex structures (patterns) in a topological space [36]. In order to attain a computable quantitative measure for the complexity of a pattern, algebraic objects are assigned to the topological space extracted from the pattern. In homology theory, specifically, a sequence of Abelian groups $H_k(X)$, $k = 0, 1, 2, \dots, N - 1$ is systematically assigned to a topological space X of N dimensions. For topological spaces with dimension $N \leq 3$, these homology groups are given by $H_k(X) = \mathbb{Z}^{\beta_k(X)}$, where the non-negative integers $\beta_k(X)$, the output of the homology analysis, are known as Betti numbers. Each $\beta_k(X)$ describes a unique topological property of X (for more details see Ref. [36]). A given topological space X of a three dimensional pattern ($N = 3$) is characterized by three distinct Betti numbers. More precisely, the zeroth Betti number β_0 counts the number of connected (distinct) components, the first Betti number β_1 defines the number of tunnels, and the second Betti number β_2 indicates the number of cavities formed within X .

As an example of distinguishing structures by homology, we here consider three simple three dimensional structures; a hollow sphere, a hollow cylinder with open ends and a torus (Fig. 2.6). The surface of each structure defines the topological space X . Homology analysis simply yields $\beta_0 = 1$, $\beta_1 = 0$, $\beta_2 = 1$ for the sphere,

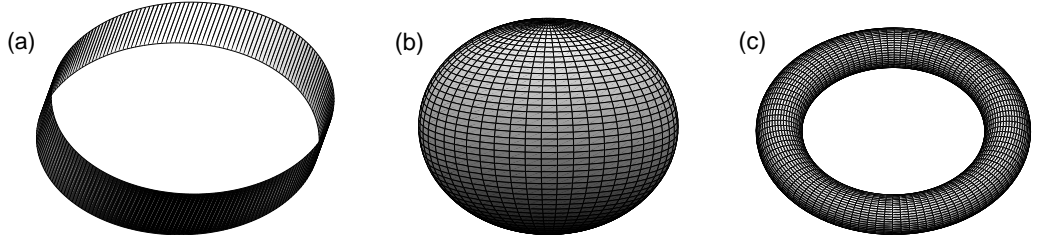


Figure 2.6: Homology yields (a) $\beta_0 = 1, \beta_1 = 1, \beta_2 = 0$ for open ended cylinder, (b) $\beta_0 = 1, \beta_1 = 0, \beta_2 = 1$ for the hollow sphere and (c) $\beta_0 = 1, \beta_1 = 2, \beta_2 = 1$ for the torus. The surface of each shape defines the topological space of interest.

$\beta_0 = 1, \beta_1 = 1, \beta_2 = 0$ for the cylinder and $\beta_0 = 1, \beta_1 = 2, \beta_2 = 1$ for the torus.

Topological space X of interest for a physical system can be identified by performing thresholding, one of the most common methods of image segmentation, on individual images in data sets. Individual pixels in an image compose X if their value is greater than some threshold value; other pixels smaller than the threshold value is considered background if there is only one X of interest. For example, visualization of the electrical activity on a cardiac tissue requires a voltage value, below which no region belongs to X . However, in microscopy where different types of cells can be captured in a single image at a time, a multiple level thresholding is required to identify different X for each type of cell imaged between different pixel ranges. A shadowgraph greyscale image from convection, on the other hand, defines two distinct X of interest: for cold flows X_c and hot flows X_h formed by a two-level thresholding. Specifically, any pixel value lower (higher) than a threshold value is set to belong to hot (cold) topological space X_h (X_c). The natural choice for threshold is the median value of intensity for all pixels in a shadowgraph image, thereby representing the cold and hot flows by the same number of pixels (the same amount of area). Similarly, in an image of temperature or velocity fields extracted from RBC simulations, the threshold is the median temperature or velocity of the field.

For the convection studies, the shadowgraph images are preprocessed for the homology analysis by first subtracting a background image taken below the onset from images and then by normalizing each image by the background to reduce nonuniformities due to the illumination. Then, a two-dimensional Fourier filter is applied to the images to remove high wave number components due to camera spatial noise (see Section 2.5). Then, two distinct binary images (for instance see Fig. 2.7(b)-(c)) that represent the regions of hot and cold flows are obtained from an image (Fig. 2.7(a)) by thresholding at the median value of intensity. The resulting binary images are then used to compute the Betti numbers as described below.

The direct computations of the homology groups of topological spaces, especially for two or three dimensional complex patterns in large data sets, are very time-consuming. (it requires an investigation on $3^N - 1$ connected neighborhood points.) We use a package of computer programs named CHomP [36] developed to perform computations of homology in arbitrary dimensions. Command line program CHomP is freely available for download via the Web [12]. The program accepts input files containing the integer coordinates of the non-zero pixels in cold and hot binary images (Fig. 2.7(b)-(c)), which describes the topological spaces X_c and X_h . In return, computations produce two Betti numbers for each space: β_{0c}, β_{1c} for the cold flows (see Fig. 2.7(d)-(f)) and β_{0h}, β_{1h} for the hot flows (see Fig. 2.7(e)-(g)) ($\beta_{2c} = \beta_{2h} = 0$ in two dimension). In particular, β_{0c} (β_{0h}) counts the number of distinct connected cold (hot) components, β_{1c} (β_{1h}) counts the number of cold (hot) holes formed within X_c (X_h). The set of nonnegative integers $\{\beta_{0c}, \beta_{0h}, \beta_{1c}, \beta_{1h}\}$ provides a reduced topological description of the pattern (Fig. 2.7).

The measurements of Betti numbers are robust with respect to the choice of threshold and the shadowgraph visualization conditions. Choosing the threshold larger than the median value by 5%, the computations for the pattern shown in Fig. 2.7 yields nearly identical results: $\{\beta_{0c} = 53, \beta_{0h} = 29, \beta_{1c} = 0, \beta_{1h} = 8\}$. We

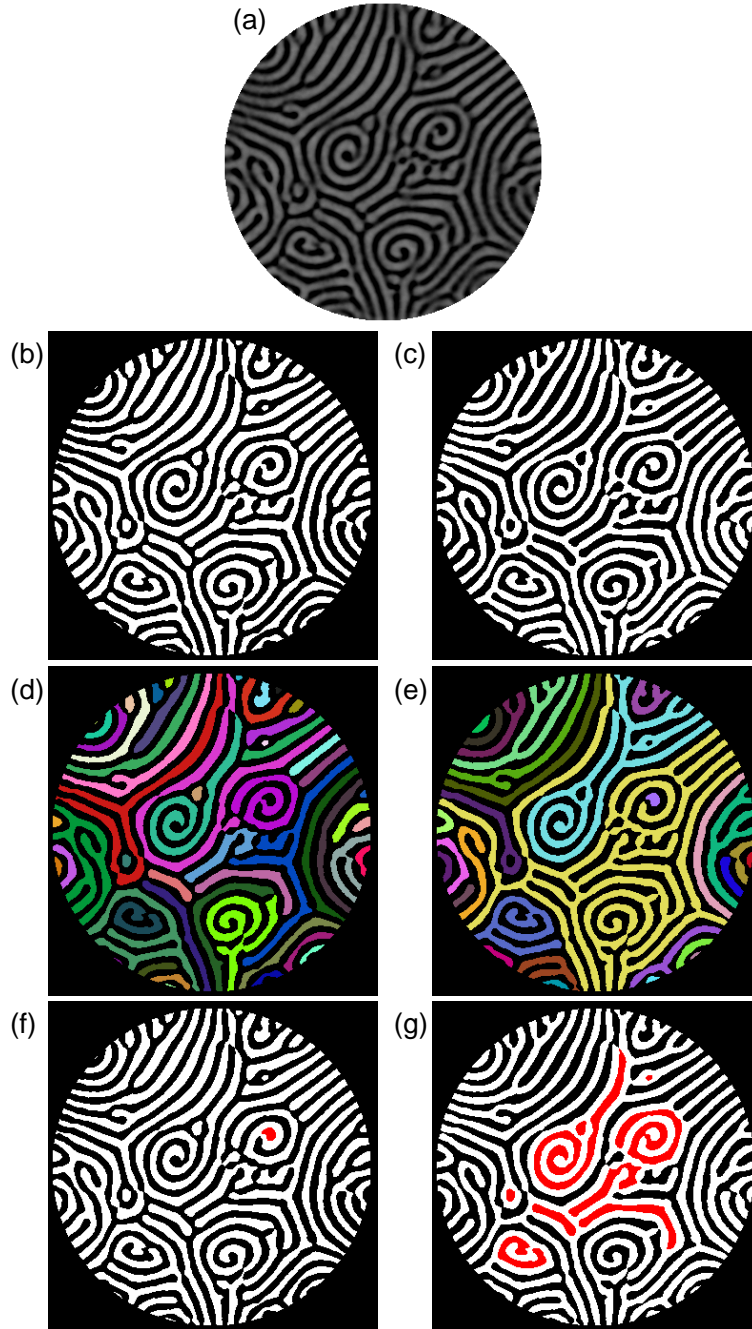


Figure 2.7: (a) A shadowgraph image captured at $\epsilon = 0.8$ in an experiment performed with SF_6 . Dark and bright regions in the image represent hot and cold flows, respectively. Two distinct binary images for (b) cold and (c) hot flows are obtained by thresholding the image at the median intensity value. Binary images defines cold X_c and hot X_h topological spaces shown by white (non-zero) pixels. Zero pixels are disregarded in computations. Computational homology yields the number of distinct components defined by the zeroth betti number for cold flows (d) $\beta_{0c} = 54$ and for hot flows (e) $\beta_{0h} = 29$, and the number of holes for cold flows (f) $\beta_{1c} = 1$ and for hot flows (g) $\beta_{1h} = 9$. The distinct components are shown in different colors and the holes are colored in red.

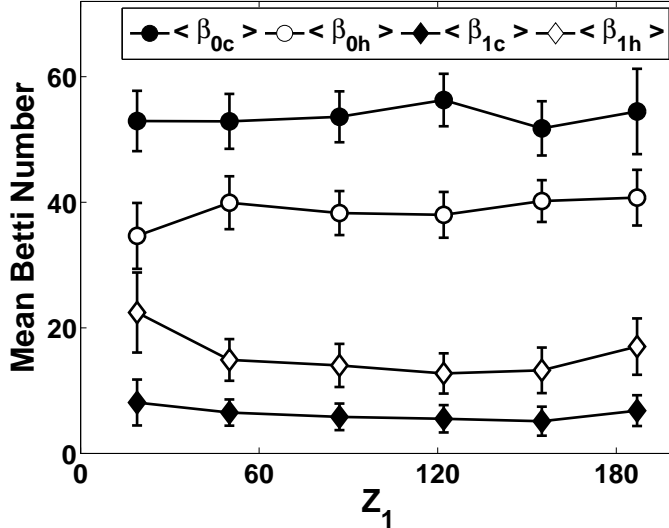


Figure 2.8: The mean Betti numbers are shown as a function of the effective optical distance z_1 of the shadowgraph system in the experiment performed at $\epsilon = 2.0$ with CO_2 . Each data point corresponds to a time average of Betti numbers from analysis of 500 images.

checked the sensitivity of the measurements of Betti numbers to shadowgraph visualization by conducting experiments at a fixed ϵ for different values of effective optical distance z_1 [30, 15]. Time averaged Betti numbers are obtained from successive computations in a time series of shadowgraph images at each value of z_1 . As seen in Fig. 2.8, the mean Betti numbers change slightly as z_1 is varied over an order of magnitude in the experiments.

2.4 Karhunen-Loève Decomposition

KLD is a characterization technique well-known in many disciplines to extract important modes from data sets. For this analysis, an ensemble of space-time data $\mathbf{u}(\mathbf{x}, t)$ from discrete arrays of intensity $\mathbf{u}(\mathbf{x}_i, t_j)$, which represent the pixel value recorded at position \mathbf{x}_i at time t_j , is first formed. A conventional KLD is given by the integral [16],

$$\int C(\mathbf{x}, \mathbf{x}') \Phi(\mathbf{x}') d^3x' = \lambda \Phi(\mathbf{x}), \quad (2.1)$$

where the kernel is $C(\mathbf{x}, \mathbf{x}') = \langle \mathbf{u}(\mathbf{x}, t) \otimes \mathbf{u}(\mathbf{x}', t) \rangle$ and built by the two-point correlation of the elements of $\mathbf{u}(\mathbf{x}, t)$ averaged over time. $\Phi(\mathbf{x})$ is the eigenvector defined as a KLD mode with associated eigenvalue λ . Solving the eigenvalue problem in Eq.(2.1) is computationally intense and generally done using a singular value decomposition (SVD) decomposition, as described below, and hence is of order n^3 where n is the number of pixels in both space and time.

For KLD analysis, we construct a $S \times T$ space-time data matrix \mathbf{U} from discrete arrays $u(x_i, t_j)$ [59]. S and T are the total number of observation sites (pixels) x_i and the total number of observation samples (number of images), respectively. First, we subtract the mean for each position x_i averaged over all j samples from that position x_i for all t_j . The $S \times S$ covariance matrix is then calculated with $\langle u(x_i, t_j)u(x_{i'}, t_j) \rangle$, where angle brackets refer to time averaging. The diagonal elements of the covariance matrix are the variances of particular observation sites and the off-diagonal elements are defined to be the covariances between different sites. The original data can be re-expressed as a new space time matrix \mathbf{Y} by a linear transformation including rotation and stretching. Therefore, the new covariance matrix for \mathbf{Y} can be constructed by having minimal covariance (redundancy) while the signal measured by the variances is maximized. The eigenvectors $\phi_k(x_i)$ of the matrix $\mathbf{U}\mathbf{U}^T$ are chosen as a new set of basis vectors for \mathbf{U} so that the covariance matrix for \mathbf{Y} is diagonal, i.e. $\mathbf{Y} = \Phi^T\mathbf{U}$. The $\phi_k(x_i)$ are orthonormal KLD modes that describe a spatial pattern of intensity over a measurement time and arranged as columns in the matrix Φ . For $S \gg T$, we compute eigenvalue decomposition of the matrix $\mathbf{U}^T\mathbf{U}$, instead of $\mathbf{U}\mathbf{U}^T$, with the corresponding orthonormal eigenvectors $v_k(t_j)$ and the eigenvalues λ_k . The matrices $\mathbf{U}^T\mathbf{U}$ and $\mathbf{U}\mathbf{U}^T$ have the same maximum $\min(S, T)$ number of non-negative eigenvalues. The eigenvectors $\phi_k(x_i)$ can also be obtained by the eigenvectors $v_k(t_j)$; $\phi_k(x_i) = \frac{1}{\sigma_k}u(x_i, t_j)v_k(t_j)$ where $\sigma_k \equiv \sqrt{\lambda_k}$ are the singular values, or equivalently $\Phi = \mathbf{U}\mathbf{V}\Sigma^{-1}$ where Σ is a diagonal matrix formed with entries σ_k . Hence, the SVD

of \mathbf{U} and the new data matrix \mathbf{Y} can be written as

$$\mathbf{U} = \Phi \Sigma \mathbf{V}^T, \mathbf{Y} = \Sigma \mathbf{V}^T \quad (2.2)$$

where $y_k(t_j)$ and $v_k(t_j)$ are arranged as rows in \mathbf{Y} and as columns in \mathbf{V} , respectively.

The original data can be written in terms of an expansion

$$u(x_i, t_j) = \sum_{k=1}^T \phi_k(x_i) y_k(t_j) \quad (2.3)$$

with $y_k(t_j) \cdot y_l(t_j) = \lambda_k \delta_{kl}$, δ_{kl} is the Kronecker delta function. Each $y_k(t_j)$ can be considered as a weight coefficient that measures the impact of the corresponding KLD mode on the original data. The first m eigenvectors corresponding to the largest m eigenvalues define the best m -dimensional approximation (dimensionality reduction) to the columns (observation sites) of X .

Fig. 2.9 demonstrates $y_1(t_j)$, $y_{100}(t_j)$ and $y_{500}(t_j)$ describing the time evolution of the spatial intensity in experimental data where $T = 15000$ shadowgraph images are analyzed at $\epsilon = 0.375$ and $\epsilon = 0.875$. $y_k(t_j)$ corresponds to the k th largest eigenvalue. At $\epsilon = 0.875$, the KLD modes are comparable in magnitude and more of them are needed to represent accurately the spatio-temporally chaotic dynamics, specifically the dynamics of SDC, in the data. On the other hand, at $\epsilon = 0.375$, when the nearly straight rolls and the defects near the sidewall move slowly throughout the pattern, fewer KL modes are necessary to describe the dynamics.

2.5 Structure Factor

The structure factor $S(\mathbf{k})$ is most often used to extract spatial information about the patterns [43, 44, 32]. The structure factor $S_t(\mathbf{k})$ of an shadowgraph image is obtained by the square of the modulus (the power) of the two dimensional Fourier transform of the image. The time averaged structure function $S(\mathbf{k})$ is given by an average over $S_t(\mathbf{k})$ in a time series of images captured at a fixed ϵ in experiments, i.e,

$$S(\mathbf{k}) = \frac{1}{T} \sum_{t=1}^{t=T} S_t(\mathbf{k}). \quad (2.4)$$

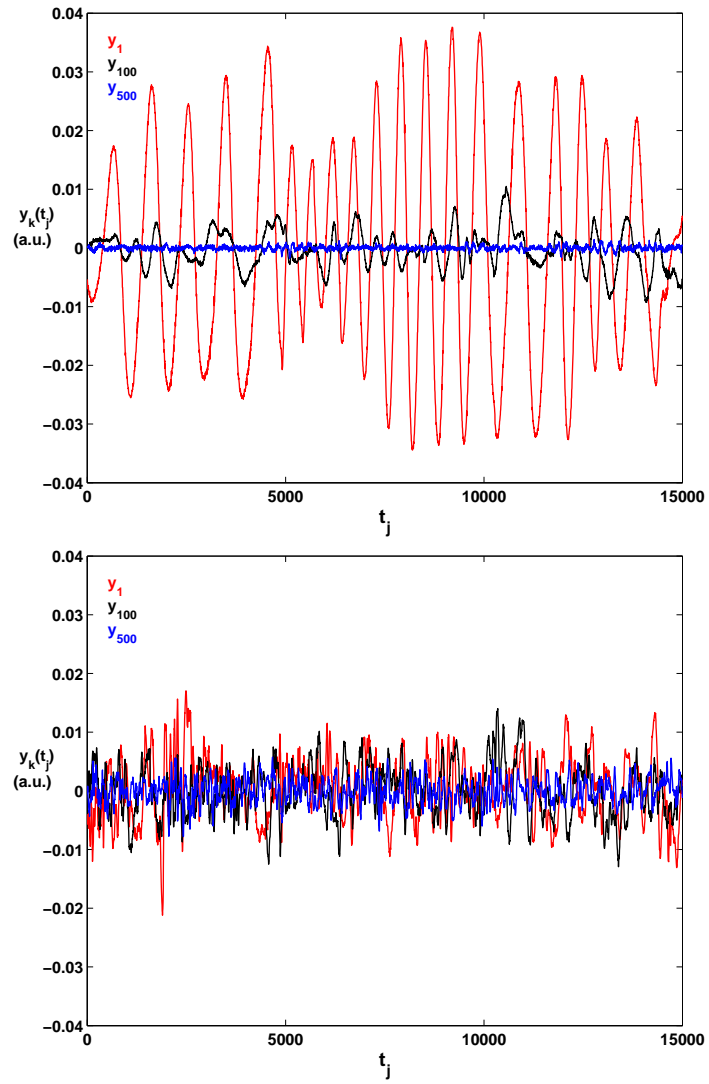


Figure 2.9: $y_k(t_j)$ associated with λ_k for $\epsilon = 0.375$ (top) and $\epsilon = 0.875$ (bottom). $y_1(t_j)$, $y_{100}(t_j)$ $y_{500}(t_j)$ corresponding to the largest, the 100th and 500th largest eigenvalues, respectively.

where T is the number of images on which discrete Fourier transforms are performed. As seen in Fig. 2.10 where $S(\mathbf{k})$ is shown for two different ϵ values, at $\epsilon = 0.4$, there is a prevailing range for roll orientation since the pattern consists of nearly straight rolls with small interior defects (for example see Fig. 2.3(b)). On the otherhand, as ϵ is set to a value for which the state of SDC is fully developed, e.g, at $\epsilon = 0.8$ (see Fig. 2.3(d)), the rotating and moving spirals throughout the pattern cover most of the possible roll orientations in time, resulting in a nearly azimuthally symmetric $S(\mathbf{k})$ distribution.

By performing an azimuthal average in wave vector \mathbf{k} -space on each discrete Fourier transform of the image, several important statistics used in pattern characterization can be achieved. For the azimuthally and time averaged $S(\mathbf{k})$, the average wave number $\langle k \rangle$ is defined by

$$\langle k \rangle = \frac{\int |\mathbf{k}| S(\mathbf{k}) d^2 \mathbf{k}}{\int S(\mathbf{k}) d^2 \mathbf{k}} = \frac{\int_0^\infty k^2 S(k) dk}{\int_0^\infty k S(k) dk}, \quad (2.5)$$

from which the skewness $S_3 = \mu_3 \xi^3$ and the excess kurtosis $K_4 = \mu_4 \xi^4 - 3$ as a measure of the degree of asymmetry and of the relative peakedness of the distribution, respectively, can be written by means of the the moments μ_n (n th central moment) of $S(\mathbf{k})$ [44, 43];

$$\mu_n = \frac{\int (|\mathbf{k}| - \langle k \rangle)^n S(\mathbf{k}) d^2 \mathbf{k}}{\int S(\mathbf{k}) d^2 \mathbf{k}} = \frac{\int_0^\infty (k - \langle k \rangle)^n S(k) dk}{\int_0^\infty k S(k) dk}, \quad (2.6)$$

$$(2.7)$$

and the correlation length ξ from the variance of the distribution;

$$\xi^{-2} = \mu_2^{-1/2} = \frac{\int_0^\infty (k - \langle k \rangle)^2 k S(k) dk}{\int_0^\infty k S(k) dk}. \quad (2.8)$$

For the statistics obtained in the power spectrum, one must take into account the effects due to the nonuniformities in illumination, the noise due to camera and the shadowgraph nonlinearities, or possible high wave-number components lying on each roll. Since all of these could introduce higher harmonics in the power distribution, we

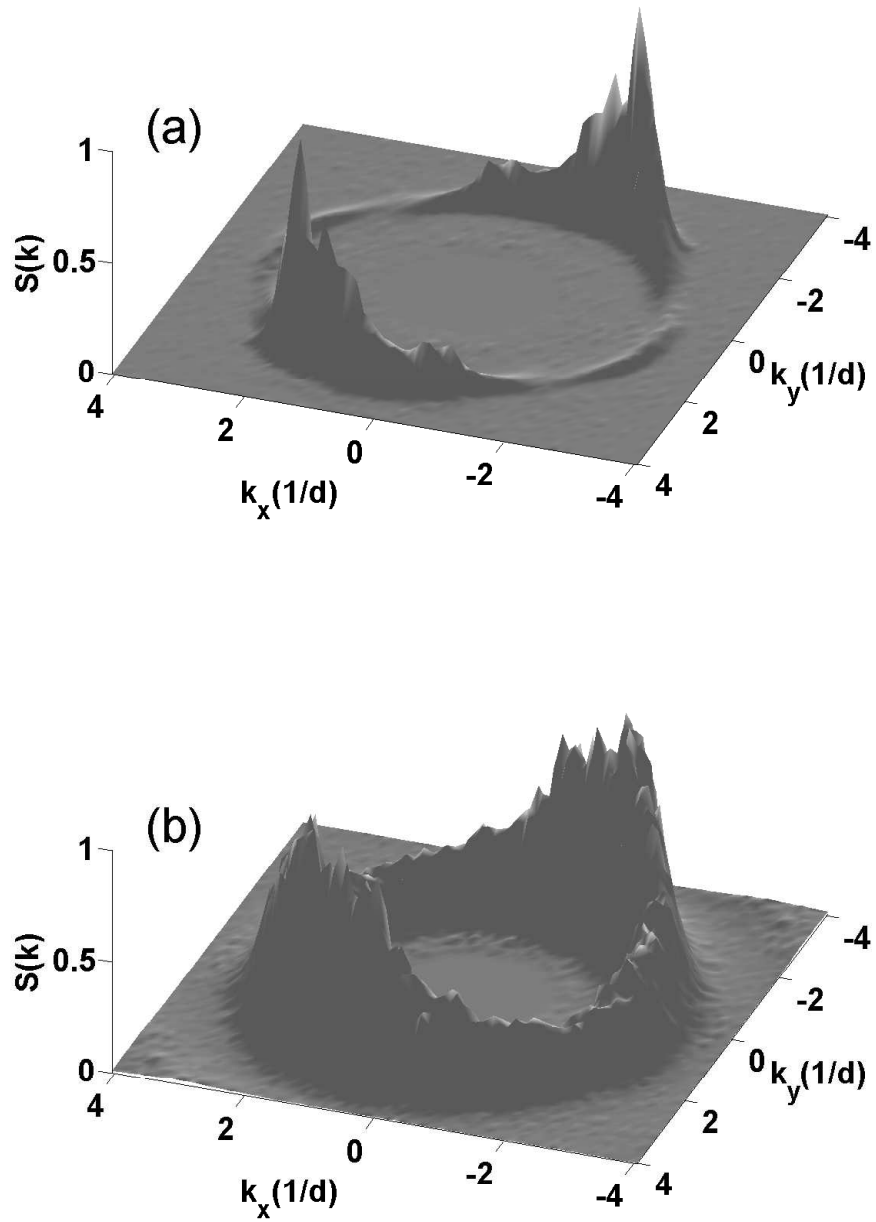


Figure 2.10: Time averaged structure function $S(\mathbf{k})$, acquired from $T = 100$ images, is shown for (a) $\epsilon = 0.4$ and (b) $\epsilon = 0.8$. Wave number components are given in units of $1/d$, where d is the depth of the convection cell.

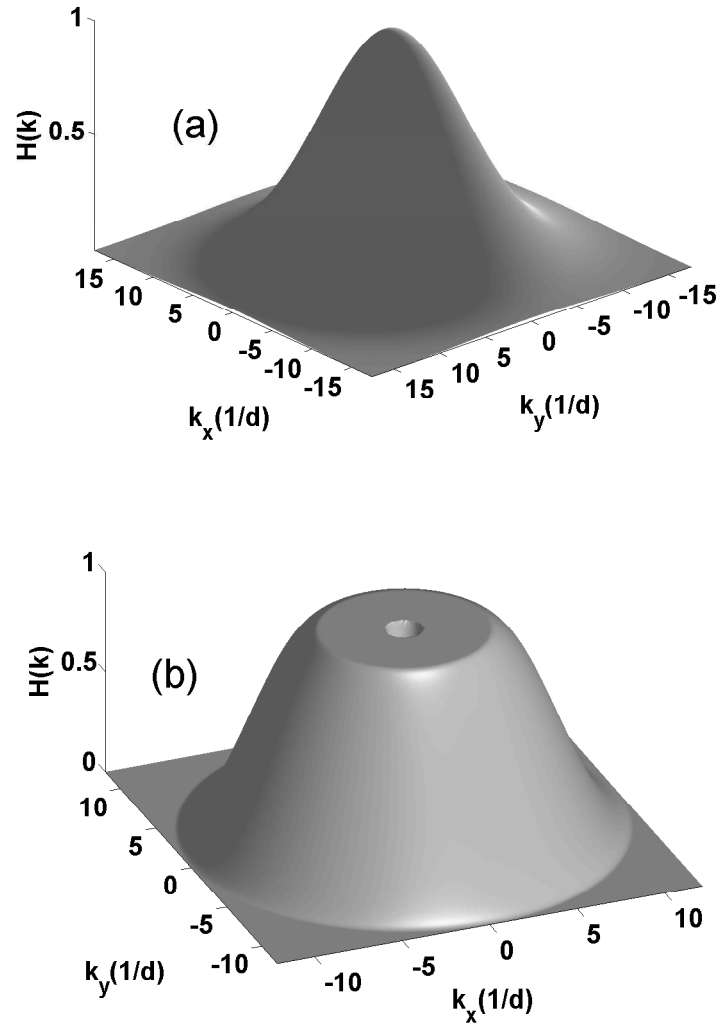


Figure 2.11: Examples of Fourier filters used to preprocess shadowgraph images: (a) a Gaussian filter $G(k)$ centered at $k \equiv |k| = 0$ with a variance $\sigma = 6/d$ where d is the depth of the convection cell, (b) a Hann Filter $H(k)$ produced by a combination of $H_1(k)$ in Eq. 2.5 for $k_1 = 0.1/d$, $k_2 = 1/d$ and $H_2(k)$ in Eq. 2.5 for $k_1 = 4.5/d$, $k_2 = 12/d$.

filter images in Fourier space by using several high and low pass filters before starting any analysis on the patterns. Two types of smooth filters we found very suitable and effective on shadowgraph images are shown in Fig. 2.11; a lowpass Gaussian filter centered at $\mathbf{k} = 0$ and given by

$$G(k) = e^{\frac{-k^2}{2\sigma}} \quad (2.9)$$

with a standard deviation σ and a filter $H(k) = H_1(k)H_2(k)$ from the combination of a lowpass Hann filter

$$H_1(k) = \begin{cases} \frac{1}{2}(1 + \cos(\pi \frac{k-k_2}{k_1-k_2})), & k_2 > k > k_1 \\ 1, & k > k_2 \\ 0, & k < k_1 \end{cases}$$

and a highpass Hann filter

$$H_2(k) = \begin{cases} \frac{1}{2}(1 + \cos(\pi \frac{k-k_1}{k_2-k_1})), & k_2 > k > k_1 \\ 0, & k > k_2 \\ 1, & k < k_1 \end{cases}$$

where k_1 and k_2 determines the position of $H(k)$ in the spectrum as demonstrated in Fig. 2.11.

2.6 Curvature and Obliqueness

In this section, we briefly describe two commonly used measures, curvature and obliqueness, obtained from textured convective flow patterns. The details of these texture analyses can be found in Ref. [28] and Ref. [32].

We extract the texture of a cold (hot) flow pattern from a skeleton-line (contour) representation corresponding to maximum (minimum) intensity regions in a shadowgraph image. We first detect the points of line defects (disclination and grain points), where the orientation is singular, and remove them from roll representations. After distinct roll pieces and the start and end points along each piece are identified, the

contours are smoothed by using a moving average filter and a high order polynomial fitting depending on the length of each contour (see Fig. 2.12(a)-(b)). Along each contour, we calculate the spatially varying roll curvature $\mathcal{C} = |\nabla \cdot \mathbf{n}|/2$ where \mathbf{n} is the unit normal vector parallel to the local wave vector (Fig. 2.12(c)-(d)). \mathcal{C} averaged over all roll pieces, or over individual pieces as seen in Fig. 2.12(e)-(f), is calculated.

The roll obliqueness is defined as $\cos(\theta) = |\mathbf{s} \cdot \mathbf{n}|$, where \mathbf{n} is the unit normal vector parallel to the local wave vector and \mathbf{s} is the sidewall normal vector. For this analysis, a narrow annular band next to the sidewall is considered. The normal vectors in the band are acquired from the texture analysis while the vectors on the sidewall are obtained on a circle defining the lateral boundary (see Fig. 2.13). The average angle θ is measured via dot product of the normal vectors \mathbf{n} and \mathbf{s} .

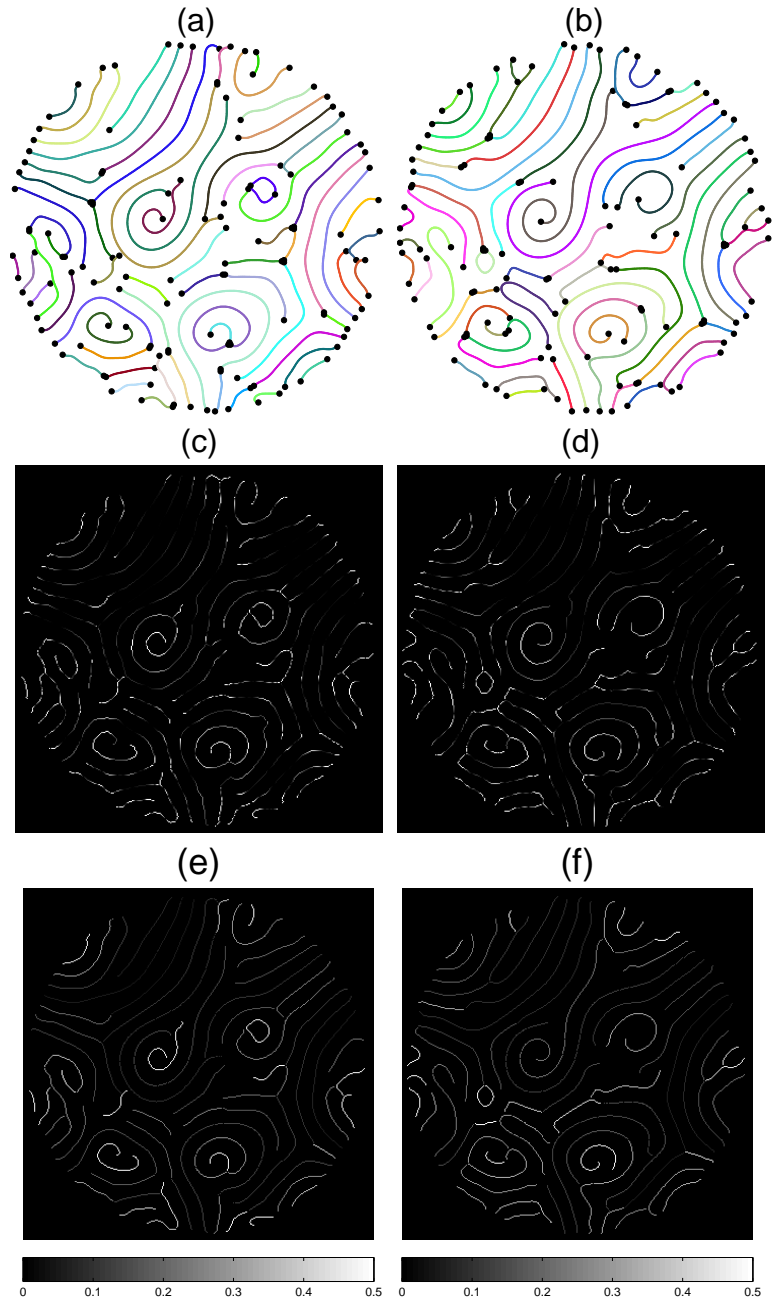


Figure 2.12: Skeleton-line representations extracted from the pattern in Fig. 2.7(a) are shown for (a) cold and (b) hot flows. The points, where the unit normal vector \mathbf{n} is undefined, are removed from the representations. The distinct roll pieces are shown in different colors; the black points indicate the end points of the pieces. The curvature \mathcal{C} is computed along the points on (c) cold and (d) hot roll pieces. In (e) and (f), the roll pieces in (a) and (b) are greyscale coded based on the average roll curvature on each piece.

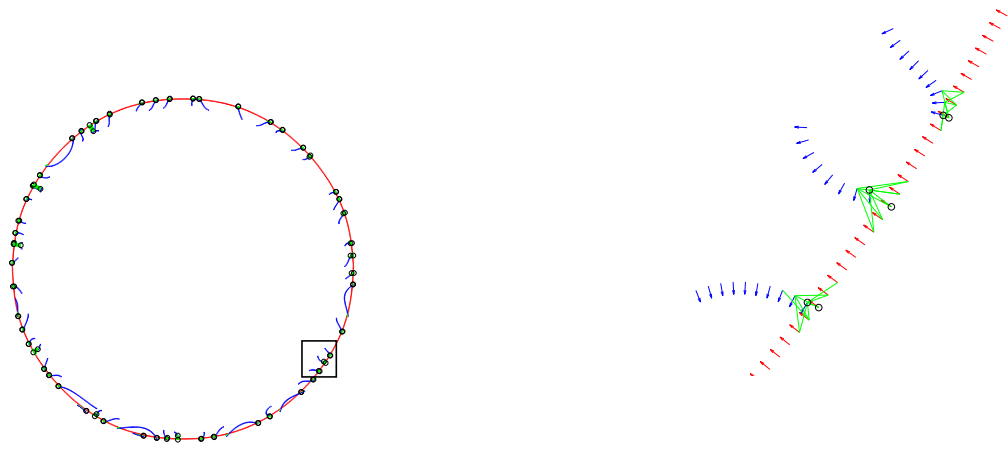


Figure 2.13: The unit sidewall (\mathbf{s}) and roll (\mathbf{n}) normal vectors, in a narrow band next to the sidewall, are shown for cold flow representation in Fig. 2.7(a). A square region is magnified for better visualization of the vectors. The closest pairs of \mathbf{n} (shown in blue) and \mathbf{s} (shown in red) vectors are identified. (Their locations are shown with open black circles.) For more accurate measurement, an additional closest 8 pairs of vectors are determined. (The pairs are connected with yellow lines.) The averaged obliqueness is measured via the dot product of the chosen vectors \mathbf{s} and \mathbf{n} .

CHAPTER III

DEPARTURES FROM THE OBERBECK-BOUSSINESQ APPROXIMATION

3.1 Introduction

The exact equations governing the fluid motion in natural convection are difficult to manage. In order to simplify the equations by reducing the nonlinearity, the Oberbeck [45] and Boussinesq [8] (OB) approximation approximation is frequently used in most theoretical and numerical studies of thermal convection, including RBC (see Appendix A). Physically, the OB approximation ignores the temperature-dependence of all fluid properties, except for the temperature-induced density variation retained in the buoyant force that drives the flow. Flows observed in nature or in the laboratory never fully commit to this approximation, and non-Oberbeck-Boussinesq (NOB) effects inevitably arise. Characterizing the strength of NOB effects in observed flows could lead to the development of improved models; however, heretofore, there has been no systematic way to quantify NOB effects using experimental data.

In this section of the thesis, we present the use of algebraic topology (computational homology) to characterize the departures from the OB approximation in RBC experiments. The homology analysis is performed on complex patterns in spatio-temporally chaotic data acquired from experiments where NOB effects are systematically varied. It is well-known that solutions to the OB equations exhibit reflection symmetry about the midplane of the layer. Characterization based on homology not only reveals the breakdown of reflection symmetry but also quantifies the strength of the asymmetries. We also show that conventional techniques, most often used to analyze the patterns in RBC, fail to uncover such asymmetries.

When the fluid's physical properties change little between the top and the bottom of the layer, the OB approximation describes the convective flow well; however, when the properties vary significantly over the layer depth, NOB effects should be taken into account. The departures from the OB approximation are characterized quantitatively by the non dimensional parameter Q introduced by Busse [9],

$$Q = \sum_{i=0}^4 \gamma_i \mathcal{P}_i \quad (3.1)$$

with

$$\begin{aligned} \gamma_0 &= -\frac{\rho_b - \rho_t}{\rho_m}, \quad \gamma_1 = \frac{\alpha_b \rho_b - \alpha_t \rho_t}{2\alpha_m \rho_m}, \quad \gamma_2 = \frac{\nu_b - \nu_t}{\nu_m}, \\ \gamma_3 &= \frac{\lambda_b - \lambda_t}{\lambda_m}, \quad \gamma_4 = \frac{c_{pb} - c_{pt}}{c_{pm}}, \end{aligned} \quad (3.2)$$

where ρ and c_p are density and specific heat at constant pressure, respectively, and $\lambda = \kappa \rho c_p$ is the thermal conductivity. (The subscripts b , t , m indicate fluid properties evaluated at bottom, top and mean temperature of the cell, respectively.) The coefficients \mathcal{P}_i are linear functions of σ^{-1} and first given by Busse [9] in the limit $\sigma \rightarrow \infty$. Bodenschatz et al. [7] reported recalculated and corrected values of \mathcal{P}_i and these coefficients were confirmed in a recent work by Ahlers et al. [1]. Typically, gases and liquids have positive and negative values of Q , respectively.

3.2 Experiments

We perform experimental runs in the spiral defect chaos (SDC) regime under different experimental conditions in order to study the departure from the OB approximation. Key parameter values for these conditions are shown in Tab. 3.1. We use gaseous SF₆ in three experiments (labeled as E-I, E-III and E-IV) with a plastic lateral boundary and gaseous CO₂ in one experiment (E-II) with a paper boundary. The aspect ratio Γ is held nearly constant for all experiments. The onset Busse parameter Q^c is calculated from Eq. 3.1 with the coefficients γ_i^c evaluated at the onset of convection ($\epsilon = 0$). The fluid properties necessary to calculate the coefficients γ_i in Eq. 3.2 for the range

Table 3.1: NOB effects with differing strengths are studied systematically by performing experiments under different conditions, E-I, E-II, E-III, and E-IV. As shown in the Table, each condition is characterized by a choice of fluid and lateral boundary along with key parameter values including the cell depth d , the aspect ratio Γ , the pressure P , the critical temperature difference across the cell ΔT_c , the vertical diffusion time $t_v = d^2/\kappa$, the Prandtl number σ , and the coefficients γ_i^c used to calculate the Busse parameter Q^c at onset.

EXPERIMENT	E-I	E-II	E-III	E-IV
Fluid	SF_6	CO_2	SF_6	SF_6
Boundary	Plastic	Paper	Plastic	Plastic
$d(\mu m)$	590	649	595	588
Γ	31.6	30.8	31.4	31.8
P(bar)	9.81	30.88	12.90	17.22
$\Delta T_c(^{\circ}C)$	12.37	5.49	5.01	1.70
$t_v(s)$	1.2	1.8	1.8	2.7
σ	0.84	0.99	0.88	0.95
γ_0^c	0.0605	0.0364	0.0294	0.0137
γ_1^c	-0.0830	-0.0567	-0.0447	-0.0243
γ_2^c	0.0975	0.0423	0.0440	0.0179
γ_3^c	0.0625	0.0141	0.0213	0.0045
γ_4^c	0.0106	-0.0360	-0.0032	-0.0107
Q^c	1.57	0.97	0.75	0.38

of experimental parameters are derived in Appendix B. The experimental conditions E-I and E-IV represent, respectively, the largest and the smallest departures from OB convection at onset.

The NOB effects near onset can affect the critical Rayleigh number R_c if they are strong enough. In a recent study by Ahlers et al. [1], the NOB corrections to $R_c = 1707.8$, i.e, $\delta R_c = R_c^{NOB} - R_c$, are computed numerically. The corrections are small in our experiments. For example, at onset $\delta R_c = 1.7$ in E-I and $\delta R_c \approx 0$ in E-IV (for calculations see Eq. 6.9 and Tab. 6 in [1]). We perform experiments at different ranges of ϵ by increasing the temperature difference ΔT at a constant mean temperature \bar{T} (measured at onset) between top and bottom plates. The correction to R_c used to estimate ϵ at larger ΔT is small even for the case where NOB effects are largest at onset, e.g, for $\epsilon = 0.8$ in E-I, the correction to R_c is 0.3%.

Away from the onset ($\epsilon > 0$), the NOB effects become stronger. The ϵ dependence of NOB effects, especially in numerical simulations, is usually characterized by the coefficients [41, 39]

$$\gamma_i \cong \gamma_i^\epsilon (1 + \epsilon), \quad (3.3)$$

which is obtained by keeping only the leading order temperature dependence in a Taylor expansion of all fluid properties. In experiments with real gases, Eq. 3.3 holds for order one values of ϵ . For instance, at $\epsilon = 0.8$, the values of γ_i evaluated from real gas properties, and the values of γ_i obtained via Eq. 3.3 agree with one another by a mean deviation of 0.8% and 0.3% for experiments E-I and E-II, respectively. σ evaluated at the top and the bottom temperature differs only slightly from σ evaluated at \bar{T} ; this variation of σ over increasing ϵ can be estimated from $(1/\sigma)(d\sigma/d\epsilon)$, which is equal to 0.015, 0.040, 0.010 and 0.009 for E-I, E-II, E-III and E-IV, respectively, for $\epsilon \leq 3.0$.

The temperature difference ΔT is increased in each experiment from onset at a constant \bar{T} to reach ϵ values, for which SDC is fully developed. Shadowgraph

Table 3.2: Key conditions are shown for experimental runs R-I, R-II, R-III, R-IV, R-V and R-VI to probe NOB effects in SDC. Q is estimated from Eq. 3.1 with the fluid properties (see Appendix) evaluated at ϵ values. The number of images N is acquired in experiments in observation times t_{obs} in units of the horizontal diffusion time t_h ($t_h = \Gamma^2 t_v$).

RUN	EXPERIMENT	Reduced Rayleigh Number	Busse Parameter	\bar{T} (°C)	$t_{obs}(t_h)$	N
R-I	E-I	$\epsilon = 0.8$	$Q = 2.80$	29.92	53	5000
R-II	E-II	$\epsilon = 0.8$	$Q = 1.75$	20.55	50	15000
R-III	E-III	$\epsilon = 0.8$	$Q = 1.35$	27.51	208	5000
R-IV	E-IV	$\epsilon = 0.8$	$Q = 0.65$	25.85	130	5000
R-V	E-III	$1.0 \leq \epsilon \leq 2.7$	$1.50 \leq Q \leq 2.79$	27.51	10	5000
R-VI	E-IV	$1.0 \leq \epsilon \leq 3.0$	$0.73 \leq Q \leq 1.44$	25.85	10	5000

image time series of spatio-temporally chaotic flow are acquired at a fixed frame rate for long observation time intervals, i.e., the intervals are large multiples of the horizontal diffusion time t_h ($t_h = \Gamma^2 t_v$ where t_v is the vertical diffusion time). Four different runs, indicated by R-I, R-II, R-III, and R-IV, are performed at $\epsilon = 0.8$ as summarized in Tab. 3.2. Sample images of patterns from these runs are shown in Fig. 3.1. Moreover, experimental runs R-V and R-VI are performed to probe the departure from the OB convection at higher Rayleigh numbers ($\epsilon > 1$). In all experimental runs, the shadowgraph images are preprocessed for the analysis by first subtracting a background image taken below the onset from images and then by normalizing each image by the background to reduce nonuniformities due to the illumination.

3.3 Homology Analysis

We first focus on the time-averaged values of the Betti numbers $\{\langle\beta_{0c}\rangle, \langle\beta_{0h}\rangle, \langle\beta_{1c}\rangle, \langle\beta_{1h}\rangle\}$ calculated from the time series of binary images in experimental runs at $\epsilon = 0.8$ (Fig. 3.2). The distinction between cold and hot flows based on the mean Betti numbers become more substantial as Q increases as seen in Fig. 3.3. The nearly equal number of components and holes point out the strong symmetry between cold and

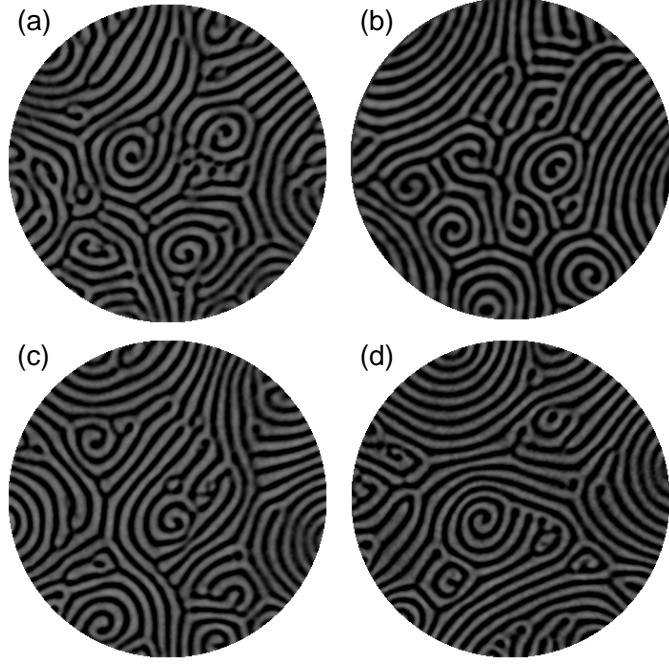


Figure 3.1: Shadowgraph patterns at fixed $\epsilon = 0.8$ and different Q illustrate that variations in NOB effects are indistinguishable by eye. The images are shown for experimental runs (a) R-I, (b) R-II, (c) R-III, and (d) R-IV (Tab. 3.2). Dark and bright regions in images represent hot and cold flows, respectively. Homology computations yield the following set of Betti numbers for these patterns $\{\beta_{0c}, \beta_{0h}, \beta_{1c}, \beta_{1h}\}$; (a) $\{54, 29, 1, 9\}$, (b) $\{42, 28, 3, 8\}$, (c) $\{43, 34, 0, 4\}$, (d) $\{43, 44, 4, 4\}$ (for details see Section 2.3).

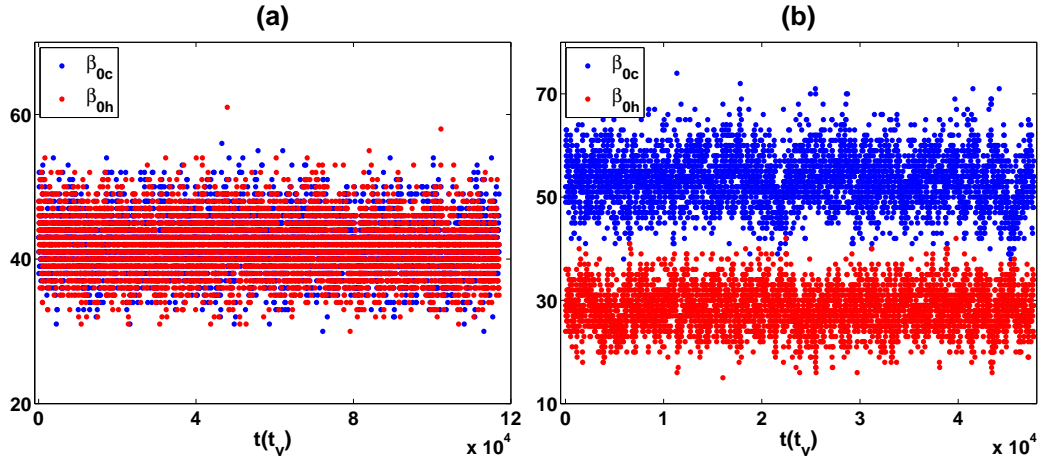


Figure 3.2: Time series of the zeroth Betti numbers are shown for (a) R-IV (b) R-I.

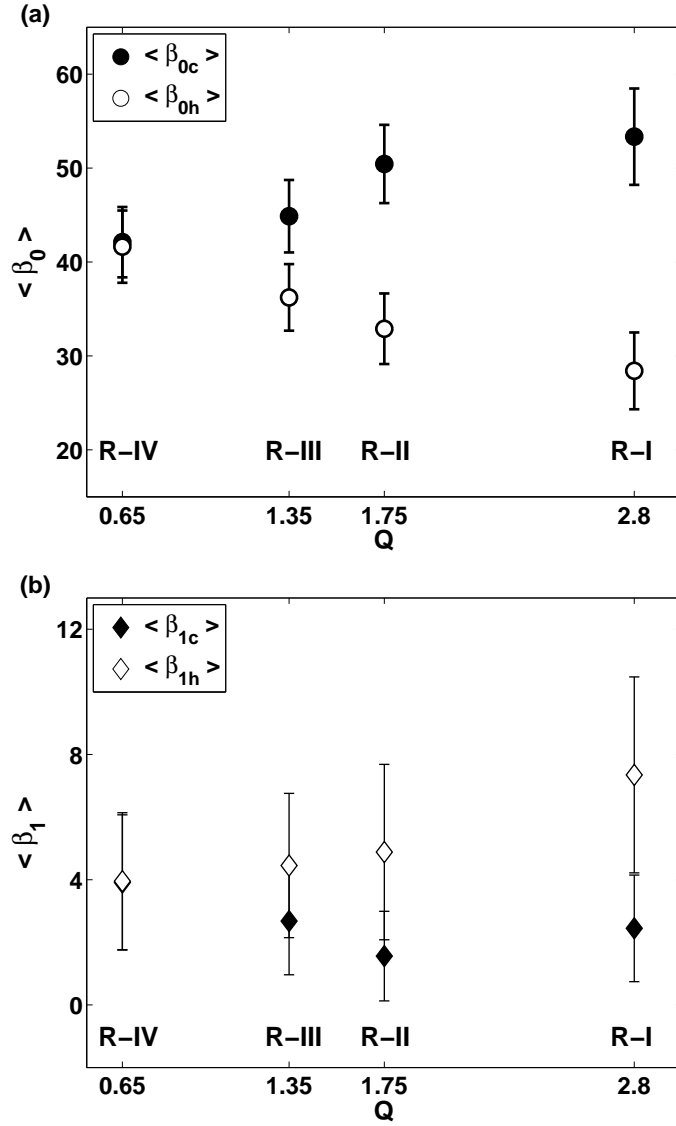


Figure 3.3: Topological asymmetries increase with the Busse parameter Q at constant ϵ . (a) The mean zeroth Betti numbers $\langle \beta_{0c} \rangle$ (filled circles) and $\langle \beta_{0h} \rangle$ (open circles); (b) the mean first Betti numbers $\langle \beta_{1c} \rangle$ (filled diamonds) and $\langle \beta_{1h} \rangle$ (open diamonds) are calculated from the time series of Betti numbers for the experimental runs (Tab. 3.2) at $\epsilon = 0.8$. In computations, 5000 images are analyzed for the runs R-I, R-III, and R-IV while 15000 images are used in computations for the run R-II.

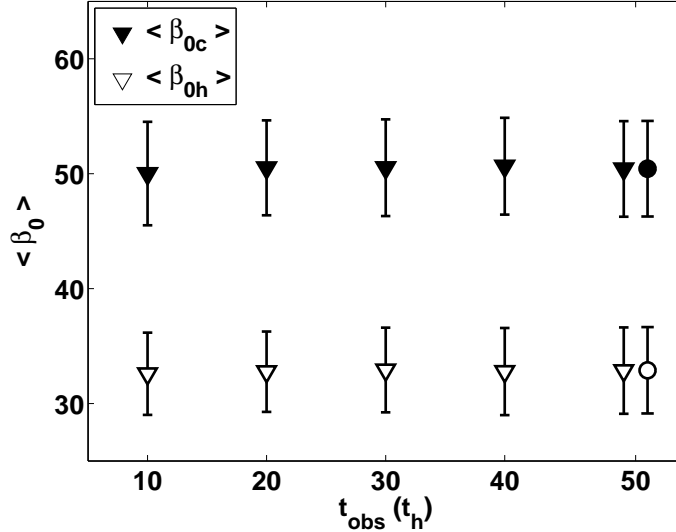


Figure 3.4: Temporal convergence of the mean zeroth Betti number in R-II. $\langle \beta_{0c} \rangle$ (filled triangles) and $\langle \beta_{0h} \rangle$ (open triangles) are shown as a function of observation time. Each data point corresponds to an average of Betti numbers from analysis of 3000 images. The results for the original data of 15000 images in $50t_h$ (Fig. 3.3(a)) are shown with circles.

hot flows for the run R-IV with the weakest NOB effects; nevertheless, the asymmetry $\langle \beta_{0c} \rangle > \langle \beta_{0h} \rangle$, $\langle \beta_{1h} \rangle > \langle \beta_{1c} \rangle$ are significant for the run R-I, which indicates a strong breakdown of the OB approximation. The asymmetry is also apparent for the run R-II, where a different type of convective fluid and of physical boundary are used. These results suggest that the outputs of homology, especially the zeroth Betti number β_0 , can be used to study the degree of departure from the OB convection.

The time averages of the Betti numbers are well-defined for a wide range of observation time intervals (Fig. 3.4). We demonstrate the temporal convergence of the mean zeroth Betti number in time by truncating the time series of β_{0c} and β_{0h} with different sampling rates in R-II. As shown in Fig. 3.4, the results obtained by averaging the Betti numbers of the same size are nearly constant with increasing observation time.

It is known that shadowgraph visualization can introduce nonlinearities depending on visualization conditions; these nonlinearities may affect the accuracy of the

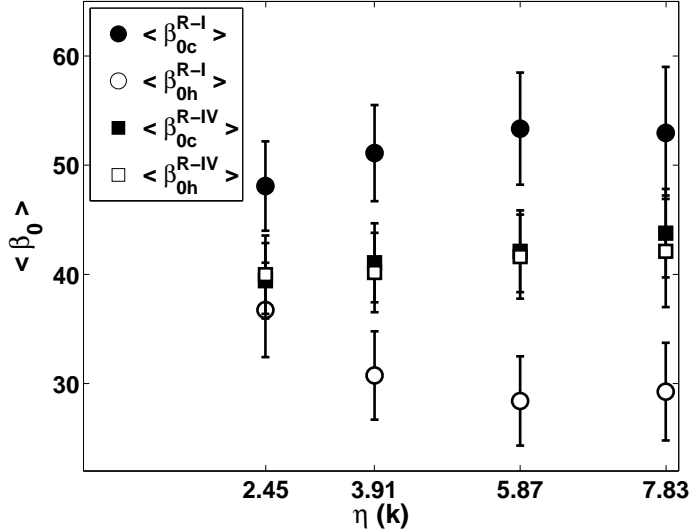


Figure 3.5: Robustness of the measurement of the mean zeroth Betti number with respect to wave number distribution. The zeroth Betti numbers, $\langle \beta_{0c} \rangle$ and $\langle \beta_{0h} \rangle$, computed for the images filtered with a two dimensional Gaussian filter of variance η in units of k . Computations are performed for two data sets, R-I (circles) and R-IV (squares). Filters with $\eta(k = 2.45)$ and $\eta(k = 7.83)$ keep %59 and %95 of the total power, respectively. k is measured in units of d^{-1} .

measurement. Robustness of the measurements of Betti numbers has been shown with respect to different effective optical distances resulting in different strength of the nonlinearities [38] (also see Fig. 2.8 in Section 2.3). These nonlinearities may also introduce higher harmonics in the wave vector (\mathbf{k}) distribution, where the strength of the harmonics increases with ϵ . Here, we investigate how the measurements of Betti numbers depend on the \mathbf{k} -distribution (see Section 2.5). For this purpose, a two dimensional Gaussian filter is centered at $\mathbf{k} = 0$ with a variance $\eta(k)$ and applied to the Fourier domain of the images to alter the distribution and to reduce the power in higher harmonics. Fig. 3.5 demonstrates $\langle \beta_{0c} \rangle$ and $\langle \beta_{0h} \rangle$ computed for the images filtered with different $\eta(k)$. The weak asymmetry for weakly NOB flows (R-IV) and the strong asymmetry for strongly NOB flows (R-I) are clearly evident even for the filter with $\eta(k = 2.45)$, which retains only 59% of the total power in the original images. Computations performed with a Gaussian filter centered at the peak of the

\mathbf{k} -distribution also yields similar results.

In order to demonstrate that the asymmetries, when they exist, extend throughout the cell, we performed computations in subregions of the flow, which are obtained by sampling the images spatially with a circular window of increasing radius r centered at the center of the convection cell. The zeroth Betti numbers are computed at each subregion. The scalings of $\langle\beta_{0c}\rangle$ and $\langle\beta_{0h}\rangle$, computed for many subregions for R-II and five subregions for R-IV, are displayed with increasing subregion area in Fig. 3.6(a). The circular regions for $r < 5d$ are too small to extract information since only a few convection rolls (in binary representation) can fit to such small regions. As soon as the subregion is large enough, the asymmetry is detected by Betti numbers. It is convenient to define an order parameter $\langle\Delta\beta_0\rangle = \langle\beta_{0c} - \beta_{0h}\rangle$ to examine the scaling of the asymmetry along the cell. As seen in Fig. 3.6(b), the asymmetry, $\langle\Delta\beta_0\rangle > 0$, grows with the area; it is noticeable in significantly different areas in R-II. On the other hand, the symmetry, $\langle\Delta\beta_0\rangle \approx 0$, is preserved along the cell in R-IV, i.e, the asymmetry between cold and hot flows is indistinguishable whether in a small region ($r = 5d$) or in a large region that almost covers the entire cell ($r = 30d$).

The more the system is driven away from the onset, the more NOB the fluid becomes as Q grows with the Rayleigh number. We analyze the data sets from R-V and R-VI described in Tab. 3.2 to investigate the departure from the OB approximation at higher Rayleigh numbers ($\epsilon \geq 1$). Fig. 3.7(a) exhibits $\langle\beta_{0c}\rangle$ and $\langle\beta_{0h}\rangle$ computed for 18 increasing ϵ values (with an increment .1 in ϵ) in R-V, and for 5 increasing ϵ values (with an increment .5 in ϵ) in R-VI. The difference between $\langle\beta_{0c}\rangle$ and $\langle\beta_{0h}\rangle$ starts to become more substantial as ϵ increases for each run. The different runs exhibit a different dependence on ϵ ; however, when plotted as a function of Q (Fig. 3.7(b)), a curve for $\langle\beta_{0c}\rangle$ and another curve for $\langle\beta_{0h}\rangle$ appear to describe the data from both runs.

Fig. 3.7(b) suggests that the zeroth Betti number data from all experimental

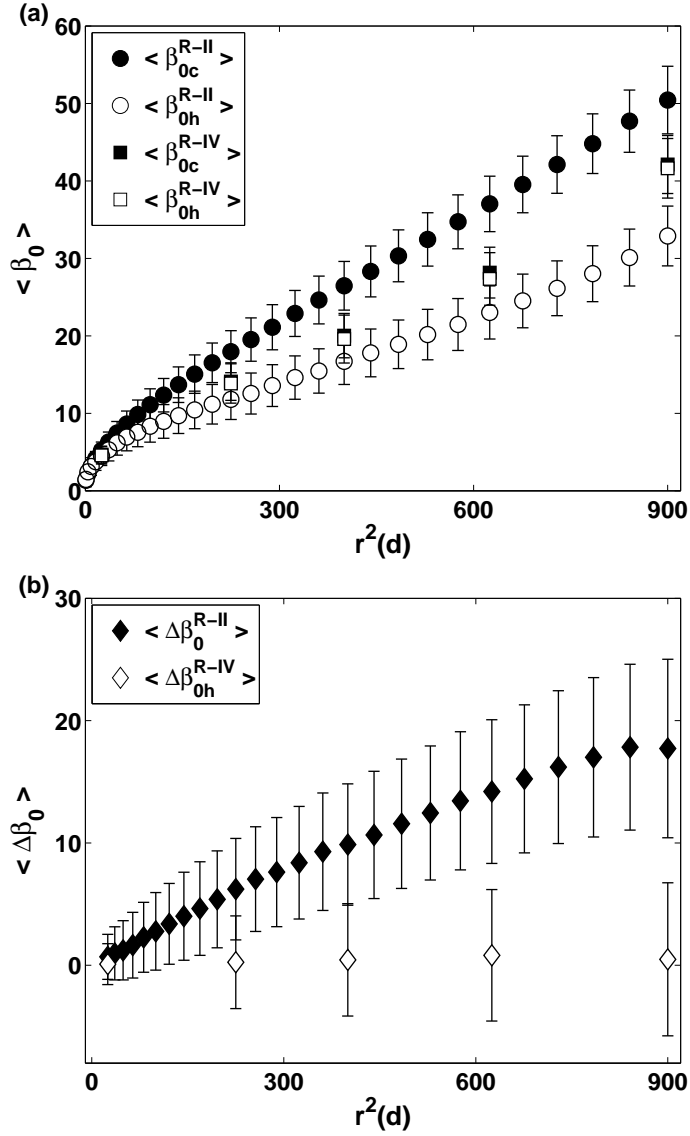


Figure 3.6: Scaling of the topological symmetry and asymmetry with system size. The zeroth mean Betti numbers are shown as a function of area of circular subregions of radius r (r is in units of the cell depth d). In run R-II ($Q = 1.75$) indicated by circles, $\langle \beta_{0c} \rangle$ and $\langle \beta_{0h} \rangle$ are obtained by analyzing 15000 images in increasing size of subregions formed by an increment d in r . In R-IV ($Q = 0.65$) indicated by squares, 5000 images are used to calculate the zeroth Betti numbers for five subregions of different sizes ($r = 5d, 15d, 20d, 25d, 30d$). (b) The order parameter $\langle \Delta \beta_0 \rangle = \langle \beta_{0c} - \beta_{0h} \rangle$ is shown as a function of subregion area for R-II (closed symbols) and R-IV (open symbols).

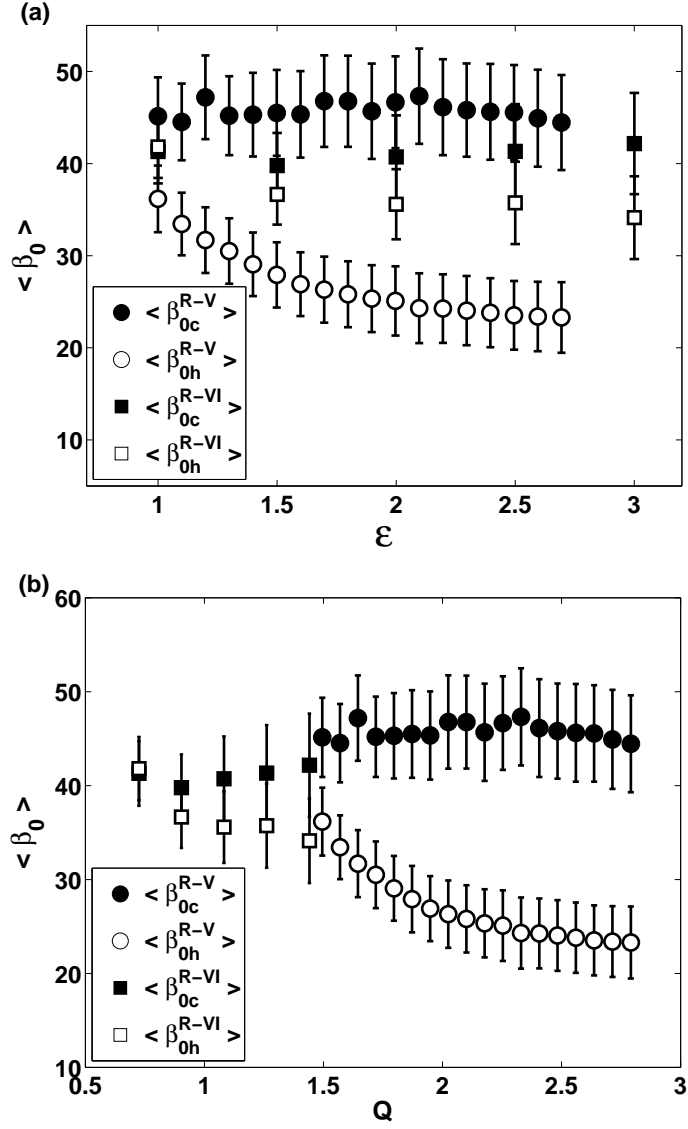


Figure 3.7: Topological asymmetries grow with the Rayleigh number. (a) $\langle \beta_{0c} \rangle$ (filled symbols) and $\langle \beta_{0h} \rangle$ (empty symbols) are shown as a function of ϵ for the run R-V (circles) and R-VI (squares). Each data point is obtained by averaging the Betti numbers from analysis of 5000 images corresponding to an observation time of $10t_h$ at each ϵ (b) The zeroth Betti numbers are shown as a function of Q estimated at the ϵ values in R-V and R-VI.

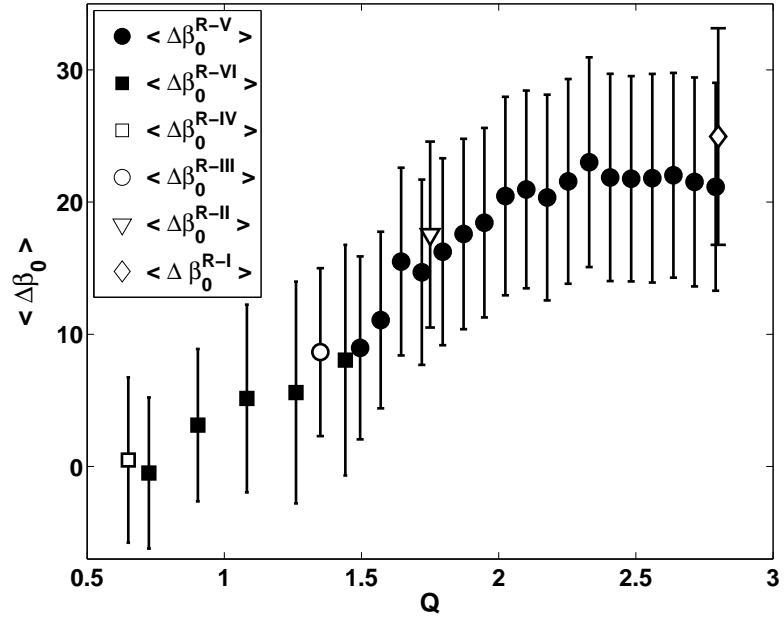


Figure 3.8: The zeroth Betti number data for *all* our experimental runs (Tab. 3.2) are represented by a single graph of $\langle \Delta\beta_0 \rangle = \langle \beta_{0c} - \beta_{0h} \rangle$ plotted solely as a function of the NOB parameter Q . Data are shown for experimental runs R-I (open diamond), R-II (open triangle), R-III (open square), R-IV (open circle), R-V (closed circles) and R-VI (closed squares).

runs may be represented by a plot of the order parameter $\langle \Delta\beta_0 \rangle$ as a function of Q (Fig. 3.8). The collapse of the data on a single curve suggests the strength of the topological asymmetry is solely dependent on NOB effects as characterized by Q . For a range of Q , $\langle \Delta\beta_0 \rangle$ monotonically increases with Q . However, for Q sufficiently large (here, $Q > 2$), $\langle \Delta\beta_0 \rangle$ is nearly constant at large Q , specifically, we find $\langle \beta_{0c} \rangle \approx 2\langle \beta_{0h} \rangle$ in R-V and R-I for $Q > 2$. This behavior at large Q could be aspect-ratio-dependent; for larger Γ the range of $\langle \Delta\beta_0 \rangle$ may increase. Further experimental studies performed with convection cell with different Γ are needed to provide a better understanding of this behavior.

3.4 Other Analysis Methods

We also apply alternative characterization techniques to analyze the same convection pattern data. Although these techniques provide a variety of information about the global features of the patterns, as we demonstrate next, they fail to identify the asymmetries that arise between cold and hot flows, even under the strong NOB effects.

The structure factor $S(\mathbf{k})$ (see Section 2.5) is most often used to extract spatial information about the patterns [43, 44, 32]. We perform an azimuthal average in wave vector (\mathbf{k}) space on each discrete Fourier transform of the image. The azimuthally and time averaged $S(\mathbf{k})$ is obtained from the time series of images. The average wave number $\langle k \rangle$ (Eq. 2.5) and the correlation length ξ (Eq. 2.8) are calculated from the distribution of $S(\mathbf{k})$. $S(\mathbf{k})$ computed for the data sets at $\epsilon = 0.8$ is shown in Fig. 3.9(a). Fig. 3.9(b) presents $\langle k \rangle$ as a function of Q , where the vertical extent is given by ξ^{-1} . The data produce nearly identical wave number distributions as Q is varied. In addition, the correlation area ($\propto \xi^2$) remains a constant percentage (nearly 1.5%) of the total cell area for all cases. We note that $S(\mathbf{k})$ does not provide quantitative characterization between cold and hot flows since it produces identical results for complementary images as dark (bright) pixels are transformed to bright

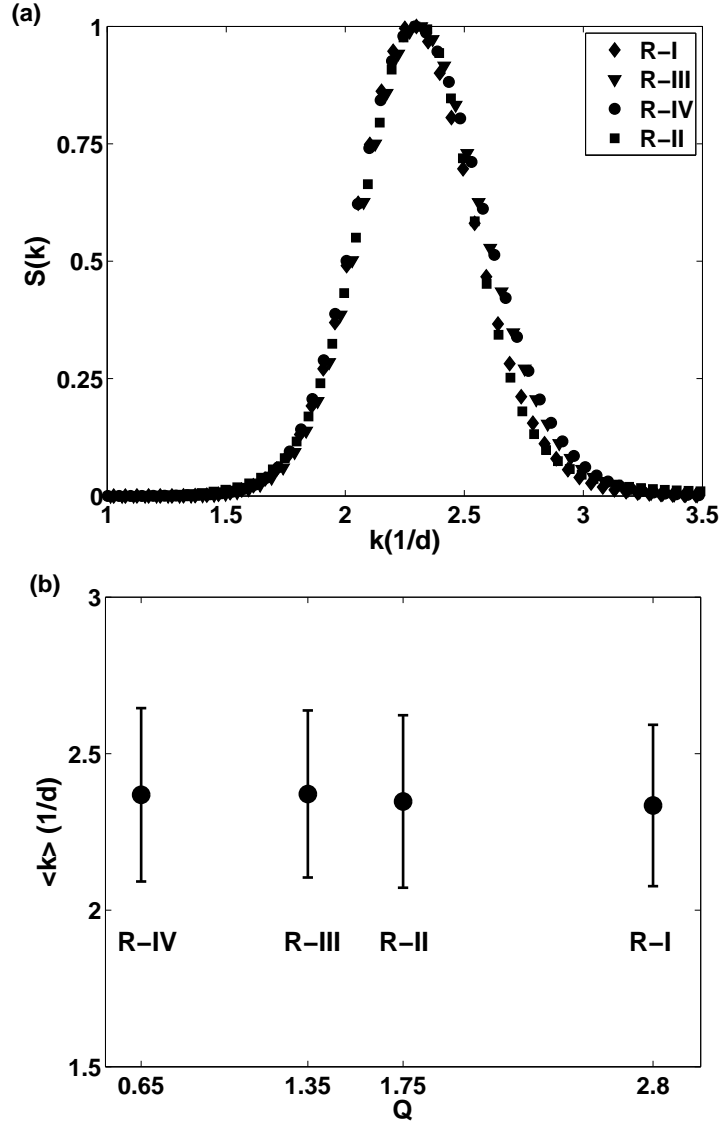


Figure 3.9: The analysis based on two-dimensional discrete Fourier transform produce nearly identical results for the patterns, on which NOB effects are varied. (a) The azimuthally and time-averaged structure factor $S(\mathbf{k})$ corresponding to the runs at $\epsilon = 0.8$. (b) the mean wave number $\langle k \rangle$ as a function of Q , the vertical bars extend by $\pm \xi^{-1}$.

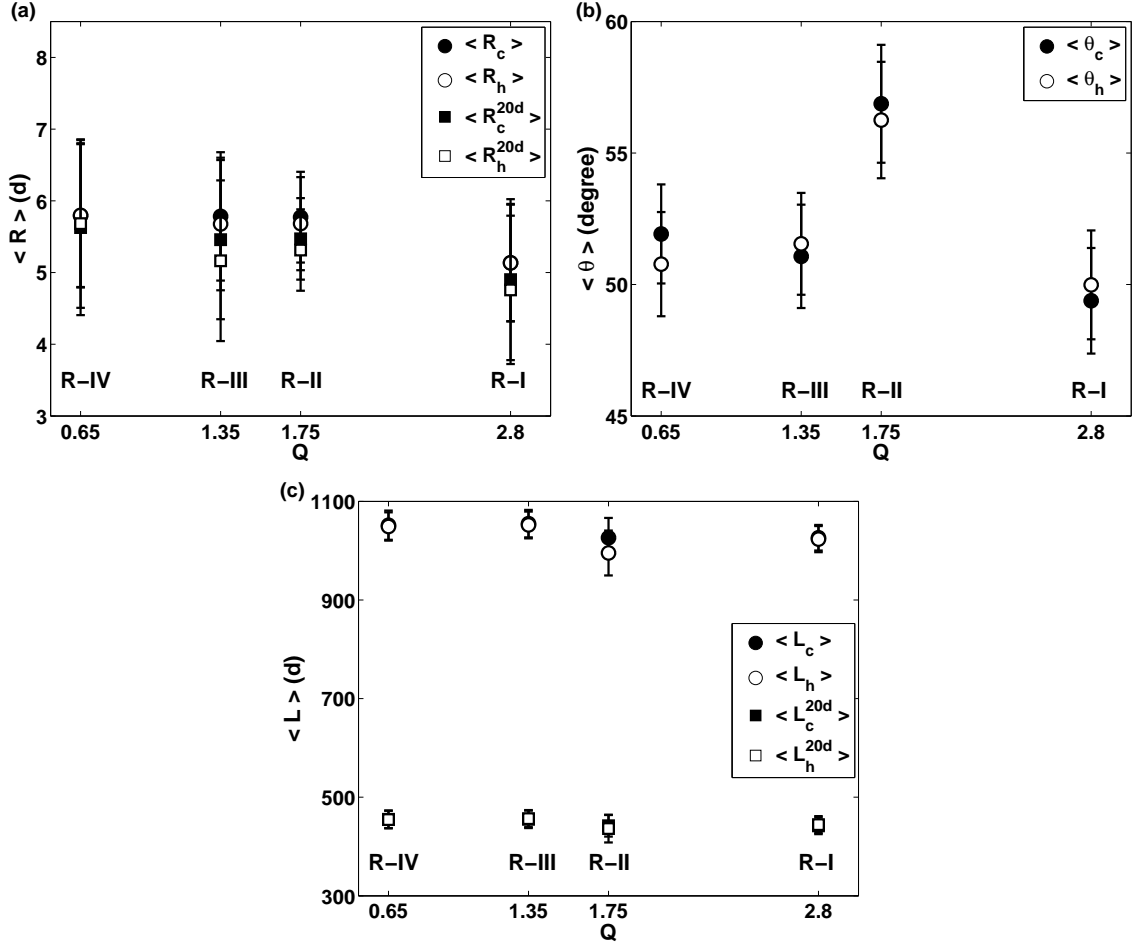


Figure 3.10: Measures calculated from the texture of the patterns for the runs at $\epsilon = 0.8$ show no distinction between cold and hot flow patterns as a function of Q . The number of images used at each point is given in Tab. 3.2. The subscripts c and h indicates the obtained quantities for cold and hot flows, respectively. (a) The time averaged radius of curvatures $\langle \mathcal{R} \rangle$ calculated for full system size and for a circular region of radius $r = 20d$ inside the cell (b) the time averaged angle of obliqueness $\langle \theta \rangle$ (c) the time averaged roll length $\langle L \rangle$ shown for full system size and for a circular region of radius $r = 20d$.

(dark) pixels.

Several important features can also be extracted from the textures of the patterns. We calculate the average spatially varying roll curvature $\mathcal{C} = |\nabla \cdot \mathbf{n}|/2$ and the average roll obliqueness $\cos(\theta) = |\mathbf{s} \cdot \mathbf{n}|$, where \mathbf{n} is the unit normal vector parallel to the local wave vector and \mathbf{s} is the sidewall normal vector (see Section 2.6 for details). \mathcal{C} is a measure of how much a roll bends per unit length. SDC relative to the states at lower ϵ is composed of highly curved rolls [33]. The rolls terminate perpendicular into the walls ($\theta = 90^\circ$) in a cell with a perfectly insulating sidewall. However, the sidewall forcing produced by a horizontal temperature gradient near the conducting wall exists in experiments and pushes the rolls to be parallel to the wall [31, 57]. We calculate the time averaged radius of curvature $\langle \mathcal{R} \rangle (\equiv 1/\langle \mathcal{C} \rangle)$, and the time averaged $\langle \theta \rangle$ as a measure of roll obliqueness, for the image data sets at $\epsilon = 0.8$. In Fig. 3.10(a) the values of $\langle \mathcal{R} \rangle$, obtained separately for cold ($\langle \mathcal{R}_c \rangle$) and hot ($\langle \mathcal{R}_h \rangle$) flow patterns, are shown as a function of Q . The curvatures of the rolls, calculated for the full circular region of the cell or a smaller circular region ($r = 20d$), stay quite close to each other even Q is increased by a factor of 4. Most importantly, no distinction between cold and hot flow patterns ($\langle \mathcal{R}_c \rangle \approx \langle \mathcal{R}_h \rangle$) is observed based on the curvature measure. This is also what is found similarly on the behavior of $\langle \theta \rangle$ with increasing Q as presented in Fig. 3.10(b). On the other hand, as a result of the lower conducting sidewall (paper) in R-II, both cold and hot rolls hit the sidewall with an acute angle that is lower for the runs performed with the higher conducting wall (plastic). We also calculated the time averaged roll length $\langle L \rangle$ from the textures of the cold and hot patterns. The value $\langle L \rangle$ estimated for each data set is close to each other while $\langle L_c \rangle \approx \langle L_h \rangle$ at different Q (Fig. 3.10(c)).

3.5 Numerical Simulations

In this section, we analyze the simulation data obtained by a direct numerical simulations of the Oberbeck-Boussinesq equations. The simulations were performed by Santiago Madruga at Universidad Politecnica de Madrid. Details of these simulations can be found extensively in Ref. [38, 41, 39]. The simulations were conducted under OB ($Q = 0$) and NOB ($Q = 4.5$) conditions. Both the temperature and the vertical velocity fields at $z = 0$, $z = -0.25$ and $z = 0.25$ are extracted from the simulations. ($z = 0$, $z = 0.5$ and $z = -0.5$ correspond to the location of midplane, the top and the bottom boundaries of the cell, respectively.) These fields are represented by 128×128 images. Sample images are shown for the midplane temperature and velocity field in Fig. 3.11. The homology analysis is performed on 400 images, corresponding to a $200t_v$ observation time, at each field. The median value of the field (temperature or vertical velocity) for each image is used as a threshold value to compute Betti numbers for the flow field. The time-averaged mean Betti numbers are extracted from time series of images at each field, sampled at $z = 0$ and $z = \pm 0.25$, for both OB and NOB conditions. As shown in Fig. 3.12, the mean zeroth and the mean first Betti numbers obtained from OB simulations show little distinction in both temperature and velocity fields. However, the analysis of the same fields in NOB simulations exhibits distinct differences in the mean Betti numbers, i.e., $\langle \beta_{0c} \rangle > \langle \beta_{0h} \rangle$, $\langle \beta_{1h} \rangle > \langle \beta_{1c} \rangle$. Our experimental results are qualitatively in agreement with the simulations where homology has revealed the asymmetries that arise in both temperature and velocity fields in the presence of NOB effects ($Q = 4.5$).

3.6 Discussion

Our results are consistent with well-known symmetries/asymmetries of convective flows that arise at onset [15]. Under Boussinesq conditions, gases exhibit straight-roll convection via a supercritical bifurcation. Homology simply yields $\beta_{0c} = \beta_{0h} = N$ and

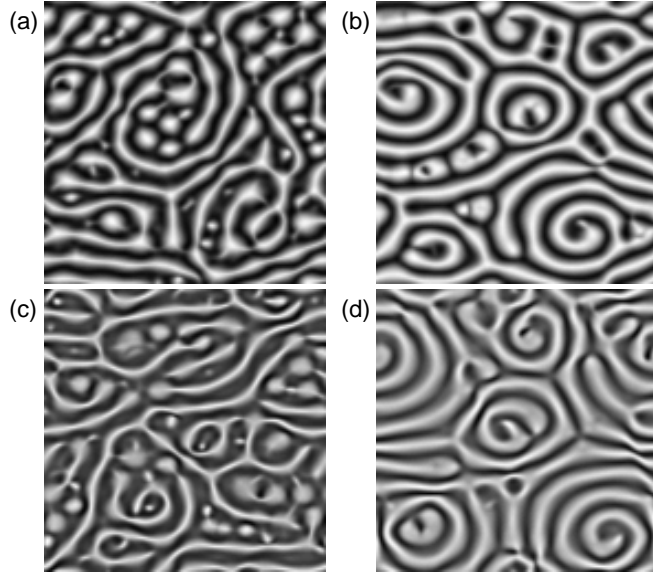


Figure 3.11: Simulations in a square domain are shown for the midplane temperature fields (a,b) and the midplane vertical velocity fields (c,d) at $\epsilon = 1.4$. In NOB simulations (a-c), all the γ_i^c are retained, while in OB simulations (b-d), all the γ_i^c are set to 0. The coefficients are $\gamma_0^c = 0.1714$, $\gamma_1^c = -0.2118$, $\gamma_2^c = 0.2836$, $\gamma_3^c = 0.1905$, $\gamma_4^c = 0.0624$ corresponding to $Q = 4.2$. The side length is equal to 16 times the pattern wavelength at onset. Computations, where the threshold is chosen as the median value of temperature or velocity field at each image, yield following set of betti numbers $\{\beta_{0c}, \beta_{0h}, \beta_{1c}, \beta_{1h}\}$; (a) $\{44, 12, 0, 22\}$, (b) $\{22, 22, 6, 6\}$, (c) $\{42, 14, 2, 19\}$, (d) $\{20, 21, 3, 3\}$

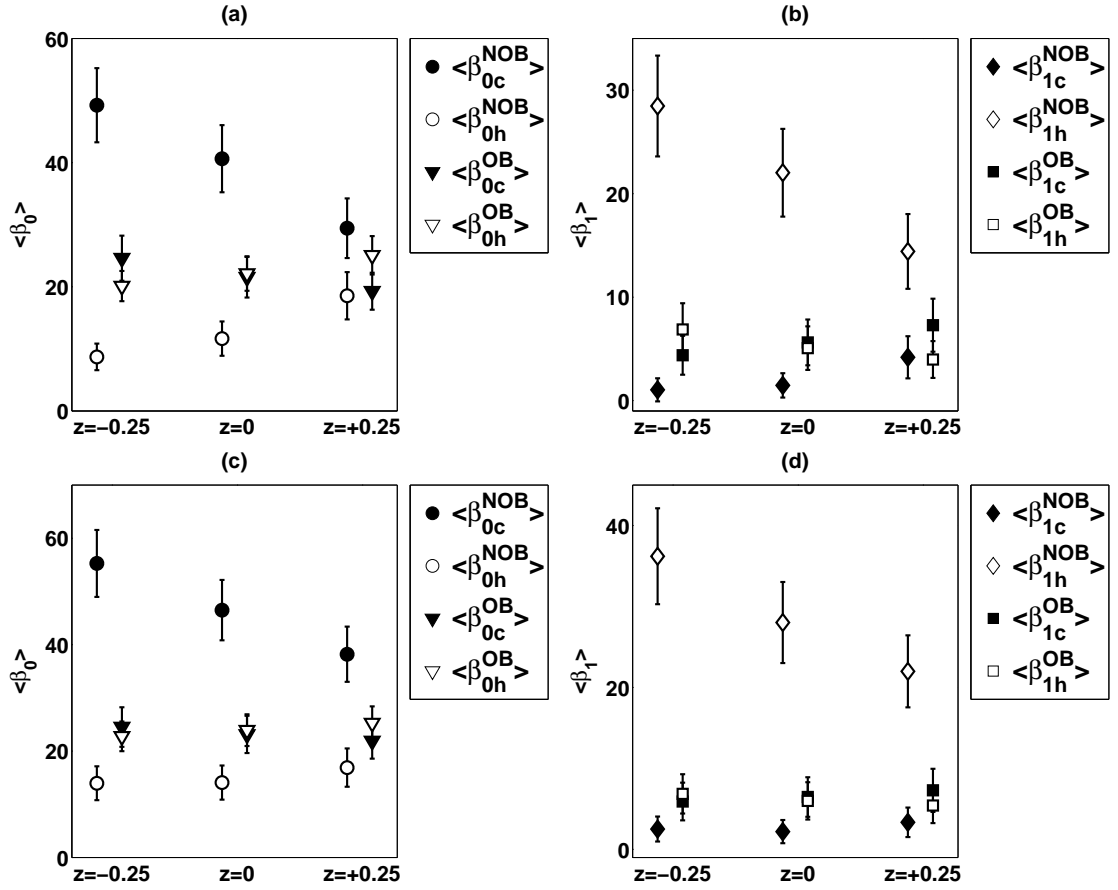


Figure 3.12: The temperature fields (a-b) and the vertical velocity fields (c-d) at $z = 0$ and $z = \pm 0.25$ from OB and NOB simulations are used to obtain the mean zeroth Betti numbers $\langle \beta_0 \rangle$ (a-c) and the mean first Betti numbers $\langle \beta_1 \rangle$ (b-d) for cold and hot flows. Each data point is obtained by averaging the Betti numbers from analysis of 400 images corresponding to an observation time of $200t_v$. The midplane, the top and the bottom boundaries of the cell is located at $z = 0$, $z = 0.5$ and $z = -0.5$, respectively.

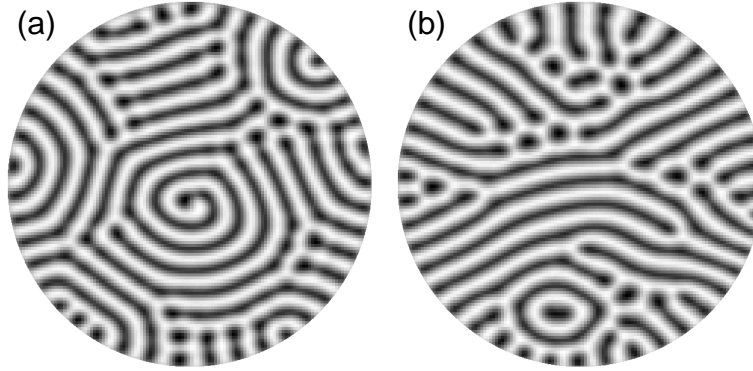


Figure 3.13: Contrary to convection in gases, patterns in liquids with negative Q have the asymmetry $\beta_{0h} > \beta_{0c}$, $\beta_{1c} > \beta_{1h}$. For instance, temperature fields from a NOB simulation in a circular cell of water are shown at (a) $\epsilon = 0.6$ and (b) $\epsilon = 1.0$, after [40]. All coefficients, $\gamma_0^c = 0.0036$, $\gamma_1^c = 0.2122$, $\gamma_2^c = -0.2725$, $\gamma_3^c = 0.0352$, and $\gamma_4^c = -0.0013$ corresponding to $Q^c = -1.84$, are retained. The diameter of the cell is equal to 16 times the pattern wavelength at onset. Computations yield the following set of Betti numbers $\{\beta_{0c}, \beta_{0h}, \beta_{1c}, \beta_{1h}\}$: (a) $\{11, 37, 6, 0\}$, (b) $\{5, 48, 10, 1\}$.

$\beta_{1h} = \beta_{1c} = 0$ for N straight rolls in a pattern (without sidewall forcing at onset). In the non-Oberbeck-Boussinesq case, the flow exhibits a subcritical bifurcation at onset where gases with positive Q (as in our experiments) display g-hexagons with (cold) downflow in the center (see sample patterns in Ref. [6]). Homology returns $\beta_{0c} = M > \beta_{0h} = 1$ and $\beta_{1h} = M > \beta_{1c} = 1$ for a pattern containing M g-hexagonal cells; in other words, the qualitative result of NOB effects leading to $\beta_{0c} > \beta_{0h}$, $\beta_{1h} > \beta_{1c}$ patterns at onset is consistent with the interpretation that NOB effects are responsible for our observations of $\beta_{0c} > \beta_{0h}$ well above onset. A further test of this consistency can be found by examining the case of NOB convection in liquids, where Q is typically negative and l-hexagons with hot upflow in the center is observed at onset (see a sample pattern in Ref. [13]). To examine the behavior of Betti numbers in liquids well above onset, we performed an analysis of the homology of temperature field images from numerical simulations of NOB convection in water reported in Ref. [40] and reproduced in Fig. 3.13. We find $\beta_{0h} > \beta_{0c}$, $\beta_{1c} > \beta_{1h}$, i.e., for NOB flows in liquids, the Betti number asymmetry far from onset is consistent with the Betti

number asymmetry for flows near onset.

CHAPTER IV

CHARACTERIZATION OF DYNAMICS

4.1 Extensive Chaos in Rayleigh-Bénard convection

4.1.1 Introduction

Characterizing data from experiments on spatially extended non-equilibrium systems is a challenge [14]. Methods devised to extract information from low-dimensional systems [56] fail as the number of dynamical degrees of freedom (DOF) increases. Recently, methods have been developed to determine the number of DOF in numerical simulations [48, 42, 18, 19, 46]; these methods suggest that the already large number of DOF grow still larger as the system size increases, i.e, the number of DOF in spatially extended systems is an extensive quantity. The techniques for measuring the number of DOF in simulations require very precise control of the initial conditions and, therefore, cannot be used in most experimental systems. What are needed are good, experimentally accessible methodologies to characterize the number of DOF efficiently in large experiment data sets not only to measure how DOF scale with system size, but also to detect the impact of finite size effects (always present in experiments) on the behavior of the number of DOF.

In this section of the thesis, we present a novel characterization method based on a topological dimension D_{CH} , which can readily be measured in experiments. We determine D_{CH} by applying the tools of algebraic topology (homology) [36] to a spatio-temporally chaotic system. We compare D_{CH} to the KLD dimension D_{KLD} [58] determined from the same experimental data using Karhunen-Loève decomposition [16]. Measurement of both dimensions not only shows the system is extensively chaotic but also provides evidence of the influence of boundaries leading to deviations from

extensive scaling. Specifically, D_{CH} and D_{KLD} exhibit similar scaling behavior that characterizes finite size effects in experiments.

The number of dynamical DOF in a chaotic system is defined by the Lyapunov dimension D_λ captured by the Lyapunov exponents [56]. Some numerical models of complex time-dependent patterns [24] have demonstrated that a positive Lyapunov exponent, indicating the existence of spatio-temporal chaos, can be extracted from homological data. A numerical study by Zoldi and Greenside [58] on a homogeneous extended chaotic system showed that D_λ and D_{KLD} demonstrate analogous extensivities. D_λ and D_{KLD} scale linearly at similar rates with either size of the entire system or size of a sufficiently large subsystem in a fixed system size. Recent direct simulations of RBC by Duggleby and Paul [17] yielded the relationship $D_{\text{KLD}} \approx 19.7D_\lambda$ from the variation of both dimensions with a range of system sizes $6 \leq \Gamma \leq 15$ in a cylindrical convection cell. Zoldi et al. [59] investigated the scaling of D_{KLD} with increasing subsystem sizes in RBC obtained by sampling the data with a spatial window of increasing size in a fixed Γ cell. They showed that SDC is extensively chaotic over a range of subsystem sizes in experiments although their measurements of D_{KLD} are not converged in large subsystem sizes. Experiments performed to observe all possible features of a chaotic system may produce enormous data sets; hence computationally establishing the convergence of D_{KLD} is often not possible with conventional KLD algorithms in today's computational power.

4.1.2 Experiments

We analyze the convection in the state of SDC. Three large sets of spatio-temporally chaotic data are acquired in different experiments as described in Table 4.1. D-I and D-II are taken in two different Γ cells where CO_2 (at 30 bars) is bounded by a lateral wall made of filter paper, while D-III is obtained in an experiment performed with

Table 4.1: SDC data taken in three different experimental cells at $\epsilon = 0.8$ with the aspect ratio $\Gamma = r/d$ (radius to depth ratio), the fluid and the sidewall used. Pr is the Prandtl number and t is the observation time in units of the horizontal diffusion time $t_h = \Gamma^2 t_v$. The vertical diffusion time t_v is order of seconds. N is the number of images captured for computations.

DATA	Γ	Fluid	Sidewall	Pr	t/t_h	$N/10^3$
D-I	35	CO_2	Paper	0.98	451	100
D-II	30	CO_2	Paper	0.98	50	15
D-III	30	SF_6	Plastic	0.95	130	105

SF_6 (at 13 bars) with a plastic (polyethersulfone) sidewall ¹. We could not perform experiments with CO_2 and the plastic in long observation times since it absorbs the gas and swells over time in high pressure [15]. Sample patterns are shown in Fig. 4.1.

4.1.3 Homology Dimension

We use the quartet $\{\beta_{0c}, \beta_{1c}, \beta_{0h}, \beta_{1h}\}$ to define the CH state of the convection pattern at the instant of time when the pattern's image is recorded. The time evolution of CH states is characterized by successive computations of Betti numbers from a time series of images; the number of distinct CH states are counted, thereby, yielding an estimate of p_k , the probability of occurrence for a given state. We introduce a positive integer D_{CH} :

$$D_{CH} = \min \left\{ k : \sum_{k=1}^{k+1} p_k > f \right\} \quad (4.1)$$

which defines the minimum number of CH states k needed to capture some fraction $f \leq 1$ of the total probability (Fig. 4.2). Here, we use D_{CH} to measure the spatio-temporal disorder of an extensively chaotic experimental system.

¹The thermal conductivities of the paper and of the plastic walls are about a factor of 4 and 10 times larger than the thermal conductivity of the fluid used.

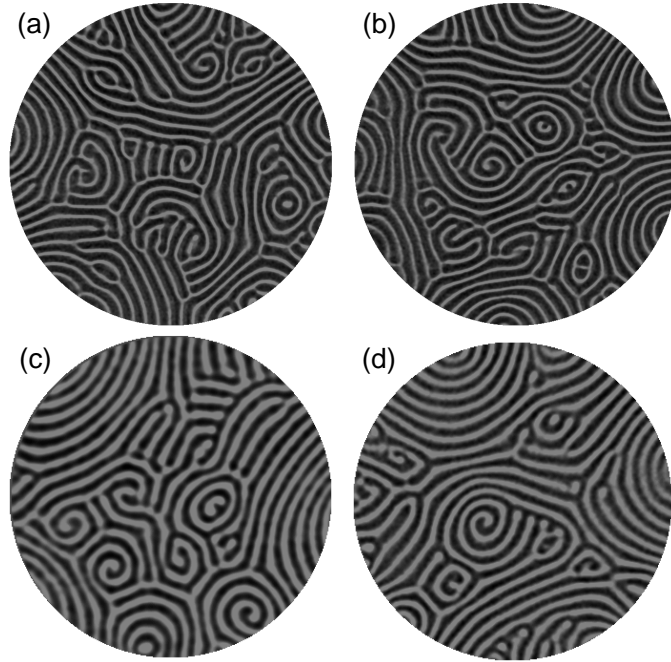


Figure 4.1: Shadowgraph patterns of SDC at $\epsilon = 0.8$. Bright and dark regions represent hot and cold flows respectively. (a)-(b) Two images from D-I separated by about $10t_h$, (c) from D-II and (d) from D-III. The median value of intensity in an image is used as a threshold value to form two distinct binary images that represent topological spaces for hot X_h and cold flows X_c , respectively. Homology, for instance, yields the following topological states for the images, $\{\beta_{0c}, \beta_{1c}, \beta_{0h}, \beta_{1h}\}$: (a) $\{64, 2, 29, 13\}$, (b) $\{65, 4, 36, 17\}$, (c) $\{42, 3, 28, 8\}$ and (d) $\{43, 4, 44, 4\}$.

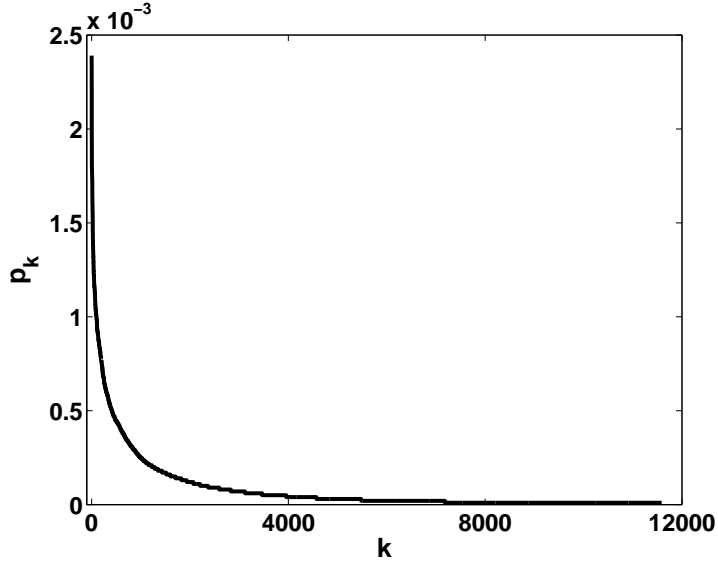


Figure 4.2: Probability distribution of CH states defined by $\{\beta_{0c}, \beta_{1c}, \beta_{0h}, \beta_{1h}\}$ is obtained from homology analysis of 100000 shadowgraph images in data set D-I. ($\sum_k p_k = 1$.) The first largest 1814 probabilities define 70% of the total probability, i.e, $D_{\text{CH}} = 1814$ for $f = 0.7$ (Eq. 4.1).

4.1.4 Karhunen-Loève Decomposition Dimension

To analyze shadowgraph data using KLD, an ensemble of space-time data $\mathbf{u}(\mathbf{x}, t)$ is first formed from the intensity arrays $\mathbf{u}(\mathbf{x}_i, t_j)$, which represent the pixel value recorded at position \mathbf{x}_i at time t_j . Conventional KLD algorithms given by Eq. 2.1 in Section 2.4 are computationally intensive on large data sets and generally done using a singular value decomposition and hence are of order n^3 where n is the number of pixels in both space and time (e.g, $n \sim 10^{10}$ space time pixels in D-I). In order to overcome this problem we implement a modified KLD algorithm proposed by Duggleby and Paul [17] for numerical data that exploits the azimuthal symmetry for a rotationally invariant experimental system. A KLD mode, specified by the pair (n, m) , is written as $\Phi_n^m(r, \theta) = \varphi_n^m(r)e^{in\theta}$ with an azimuthal wavenumber n and an eigen number m . This results in a small eigenvalue problem;

$$\int_0^{r_o} C_n(r, r')\varphi_n^m(r')r'dr' = \lambda_n^m\varphi_n^m(r), \quad (4.2)$$

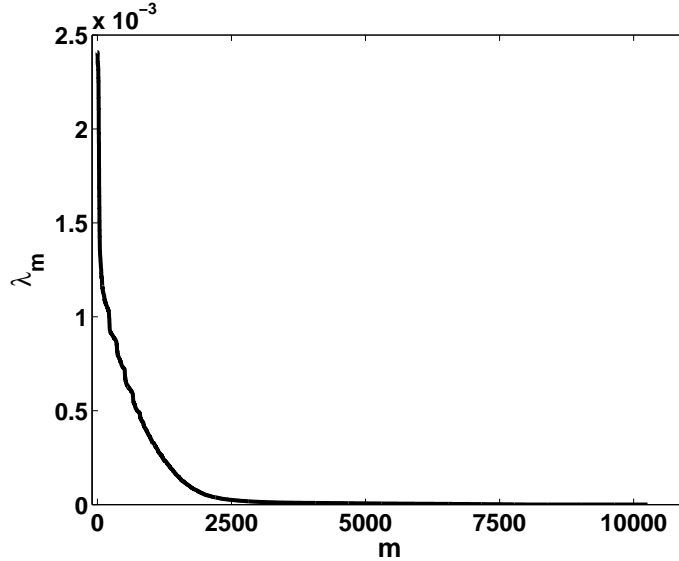


Figure 4.3: Eigenvalue spectrum is obtained from Fourier based KLD analysis applied on 100000 shadowgraph images in data set D-I. ($\sum_m \lambda_m = 1$.) The first largest 806 eigenvalues define 70% of the spectrum, i.e, $D_{\text{KLD}} = 806$ for $f = 0.7$ (Eq. 4.3).

for each wavenumber n one must analyze the tensor $C_n(r, r') = \langle \hat{\mathbf{u}}_n(r, t) \otimes \hat{\mathbf{u}}_n^*(r', t) \rangle$, where $\hat{\mathbf{u}}_n(r, t)$ is the Fourier transform of $\mathbf{u}(\mathbf{x}, t)$ in the azimuthal direction and $*$ denotes the complex conjugate. In computations the eigenvalues are ordered in descending order and normalized by the sum of all the eigenvalues. The KLD dimension D_{KLD} [58]

$$D_{\text{KLD}} = \min \left\{ m : \sum_{m=1}^{m+1} \lambda_m > f \right\} \quad (4.3)$$

defines the minimum number of KLD modes m required to capture some fraction $f \leq 1$ of the total eigenvalue spectrum (Fig. 4.3).

In order to show the clear advantage of computing D_{KLD} from Fourier based KLD, we perform two convergence tests. First, we form a series of images by rotating a single image, given in Fig. 4.1(a), azimuthally by the angles $\theta = k\Delta\theta$ with $\Delta\theta = 2\pi/180$, where $k = 1, 2, \dots, 360$. Thus, we obtain a set of 360 images from two complete rotations of the original image. In Fig. 4.4, the cumulative dimension D_{KLD} obtained from both methods are shown as a function of k . It is evident that Fourier based

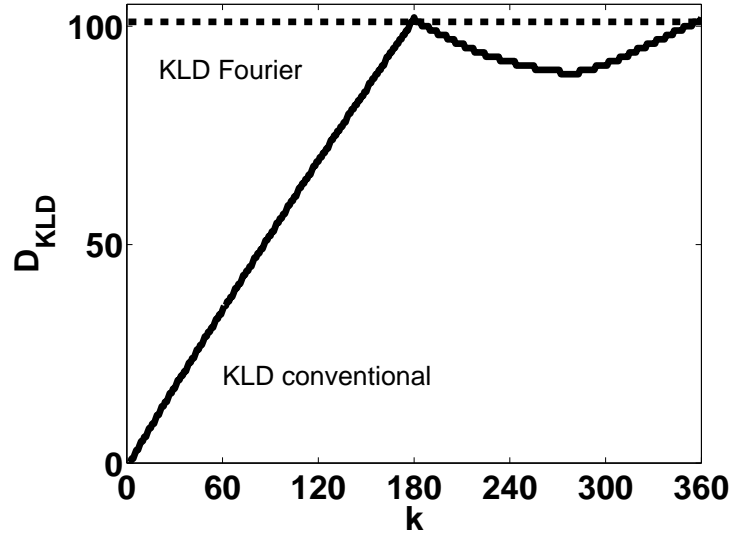


Figure 4.4: The cumulative D_{KLD} (for $f = 0.7$) obtained from conventional KLD (dashed line) and fourier based KLD (solid line) is shown as a function of the number of images k used in computations. The image data is created by rotating a single shadowgraph image by increments of $\Delta\theta = 2\pi/180$.

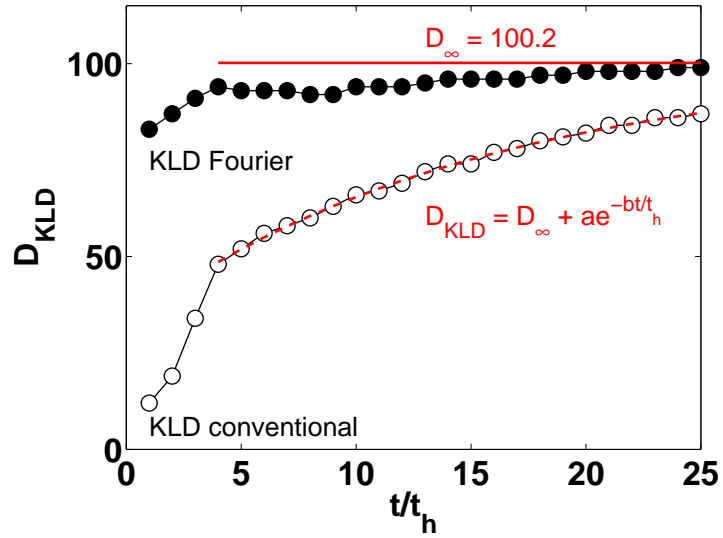


Figure 4.5: The cumulative D_{KLD} (for $f = 0.7$) acquired from conventional KLD (open circles) and Fourier based KLD (closed circles) are shown as a function of time. The red dashed line is the curve fit $D_{\text{KLD}} = D_{\infty} + ae^{-bt/t_h}$ ($a = -67.14$, $b = -0.0657$) for conventional KLD. The asymptotic value $D_{\infty} = 100.2$ for the conventional KLD is shown by the solid red line.

KLD takes advantage of the rotational invariance. Second, 5000 images in $25t_h$ are extracted from D-I and sampled spatially with a circular window of radius $12d$. We investigate the convergence of D_{KLD} from both methods in observation time. As seen Fig. 4.5, D_{KLD} from Fourier based KLD reaches an asymptotic value, to which D_{KLD} from conventional KLD fail to converge during the same time interval.

4.1.5 Extensive Scalings

CH and KLD provide very different methods for analyzing convection patterns; nevertheless, we find D_{KLD} and D_{CH} increase in a similar manner as new degrees of freedom are added. We explore extensivities of D_{CH} and D_{KLD} for different subsystems sizes in D-I, which are obtained by sampling the data spatially with a circular window of increasing radius r , measured in units of depth d from the cell center. We work with a fixed fraction $f = 0.7$ [59] to compute D_{CH} and D_{KLD} from the eigenvalue spectra and the probability distributions, respectively, for each subsystem. We find that, over a large range of subsystem sizes, D_{KLD} scales extensively with the area of the system $A \propto r^2$ (Fig. 4.6), consistent with the results of KLD analyses in previous numerical and experimental studies that strongly suggest that the state of SDC is extensively chaotic [58, 59]. We find that D_{CH} also provides strong evidence for extensive chaos; D_{CH} also scales extensively with r^2 over substantially the same broad range of subsystem sizes as D_{KLD} (Fig. 4.6).

Computational homology offers a way to measure dimensions that converge more rapidly than dimensions measured using KLD. Conventional KLD become prohibitively expensive to compute even for moderately large system sizes; as a result, measurements of D_{KLD} can fail to converge [59]. Fourier-based KLD (used in our analysis) provides faster and converged estimates of D_{KLD} in large subsystem sizes [17]; it is, however, only suitable for systems with rotational or translational invariance. CH has no such limitations and can be performed on sufficiently large systems with a

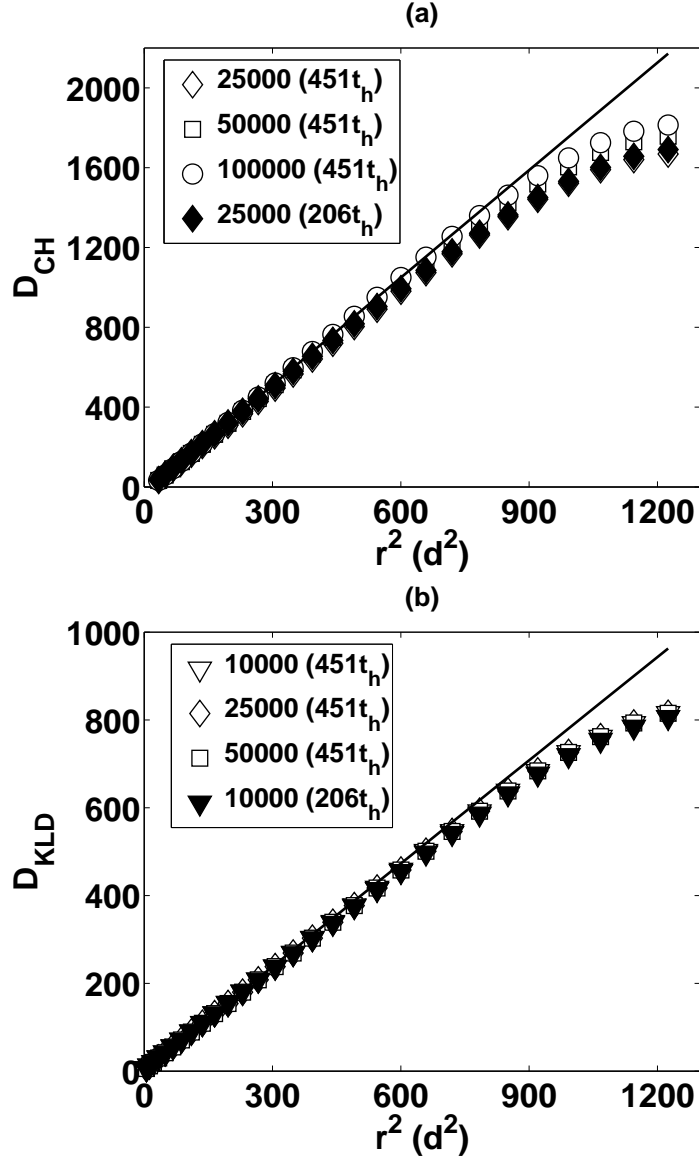


Figure 4.6: Extensive Scalings of D_{CH} and D_{KLD} for increasing subsystem sizes are obtained by computational homology (a) and a modified KLD algorithm based on a Fourier method (b), respectively for fraction $f = 0.7$ in D-I. The number of images, at given observation times, used at each data point in computations is labeled. The linear lines are drawn to guide the extensivities to eye. Choosing f very close to 1 may include experimental errors, whereas choosing it too small may exclude necessary modes and states necessary to describe the dynamics. But, for the range $0.5 \leq f \leq 0.9$, extensive scalings of dimensions normalized by the maximum dimension at each f nearly fall on a single curve.

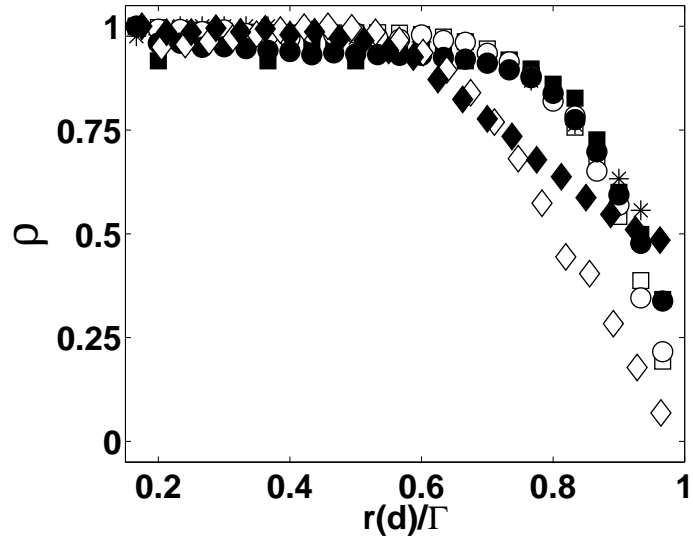


Figure 4.7: The rates of increase ρ estimated from extensive scalings of D_{CH} (open symbols) and D_{KLD} (closed symbols) are shown as a function of r/Γ to indicate the sidewall effects in the experiments, D-I (squares), D-II (circles), D-III (diamonds), at $\epsilon = 0.8$. The number of images used for computations in D-II and D-III is given in Table 4.1. Also, ρ as dimension per area is obtained from conventional KLD algorithm (asterisks) by sampling the data of 10,000 images in D-I with an annular window of inner r and outer $r + 2d$ radius ($5d \leq r$).

boundary of any shape. It is far easier to compute D_{CH} than D_{KLD} since the CH analysis is carried out separately for each snapshot.

We demonstrate the convergence for both KLD and CH analyses of our data by using different sampling methods. In one approach, we change the sampling rate, thereby changing both total observation time and the number of images in the analysis. We find both D_{KLD} and D_{CH} converge provided that sufficiently large data sets are used in computations [Fig. 4.6]. We also compute extensive scaling of D_{CH} by using samples randomly chosen from the data; D_{CH} exhibits exactly the same scaling with the subsystem sizes in data sets of 25,000 images selected either randomly or a fixed sampling period of $451t_h$.

As the analyzed subsystem size approaches the physical size of the experiment, both D_{CH} and D_{KLD} deviate from scaling in the same way (Fig. 4.7). To compare this deviation in both dimensions quantitatively, we use an intensive quantity $\rho = \partial D / \partial A$ measured as a function of the radial distance from the cell center. For each dimension, the values of ρ are normalized to remove parametric dependence on the choice of f ; moreover, the radial distance r is normalized by the aspect ratio Γ . In this representation (Fig. 4.7), $\rho = 1$ (for small r/Γ) indicates both D_{CH} and D_{KLD} scale linearly with the area; however, ρ becomes significantly less than one for both D_{CH} and D_{KLD} for r/Γ sufficiently large. Remarkably, the deviation of ρ from unity exhibits a similar functional dependence on r/Γ for both D_{CH} and D_{KLD} .

Our results suggest the deviation from scaling for D_{CH} and D_{KLD} measures the impact of lateral boundaries (sidewalls) on the chaotic flow (Fig. 4.7). Sidewalls affect convection patterns due to the mismatch in the thermal conductivities of the sidewall and the fluid; sidewall effects have previously been probed primarily at small ϵ near convection onset [15, 31]. Here, we examine the effect of sidewalls far from onset by comparing the behavior of ρ for experiments with different sidewall conditions at $\epsilon = 0.8$. We see that ρ for both D_{CH} and D_{KLD} exhibits the same deviation

from scaling for experiments in different sized convection cells, as long as the lateral boundary conditions are similar (experiments D-I and D-II in Fig. 4.7). However, in experiments where the (plastic) lateral boundaries increase sidewall forcing of the convective flow (D-III in Fig. 4.7) ρ for both D_{CH} and D_{KLD} deviates from scaling at smaller r/Γ than for experiments with (paper) lateral boundaries where sidewall forcing is weaker (D-II in Fig. 4.7). More specifically, for both D_{CH} and D_{KLD} , ρ decreases by 25% (from unity) at $r/\Gamma = 0.83d$ in D-I and D-II and at $r/\Gamma = 0.70d$ in D-III (at $r = 21d$). Moreover, our measurements are robust with respect to nonlinearities associated with shadowgraph imaging do not alter our results; measurements of D_{CH} and D_{KLD} , computed for the full circular system and a circular region ($r = 15d$) from long time series of shadowgraph images, fluctuate only 3% and 10%, respectively, as the effective optical distance is varied over an order of magnitude in experiments [38].

4.2 *Transition to Spiral Defect Chaos*

4.2.1 Introduction

In this section, we present the use of Karhunen-Loève decomposition (KLD) and computational homology (CH) to obtain quantitative information (entropy) about the pattern dynamical complexity as a function of thermal driving (ϵ) in Rayleigh-Bénard convection (RBC) experiments. Information is obtained from the probability distributions constructed from the outputs of CH in order to identify different spatio-temporal states at different control parameters in experiments. We obtain analogous information content at the same parameter values captured by normalized eigenvalue spectra obtained by the KLD from the same experimental data. In particular, CH entropy S_{CH} and KLD entropy S_{KLD} are used to detect the transition to the state of spiral defect chaos (SDC). Converged estimates of both information entropies can be achieved in moderate amount (a couple of thousand images) of experimental data, in which, however, the homology dimension D_{CH} and the KLD dimensions D_{KLD} (see

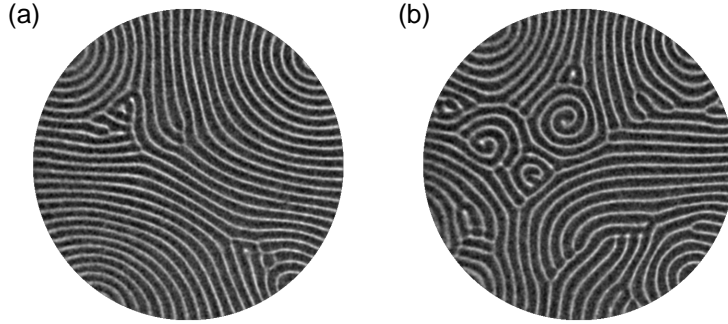


Figure 4.8: Shadowgraph snapshots of convective patterns in the experiment taken at (a) $\epsilon = 0.625$ (below the onset of spiral defect chaos) and (b) $\epsilon = 0.75$ (above the onset of spiral defect chaos).

Section 4.1.3 and see Section 4.1.4) most likely fail to converge. (Both dimensions require large number of experimental data in long experimental observation times.)

The experimental data is acquired in a cylindrical convection cell of aspect ratio $\Gamma = 35$, where convective gas CO_2 is confined. The Prandtl number Pr is near 1 and the vertical diffusion time t_v is approximately 1.7 s in the experiment. Time series of 15000 shadowgraph images are captured at five increasing ϵ values in $50t_h$ ($t_h = \Gamma^2 t_v$). As we will demonstrate by the information entropy, the transition to SDC occurs for $\epsilon > 0.625$ (See Fig. 4.8) in our experiment. Before we apply entropy analysis on the experimental data, we first apply a variety of statistical measures, previously proposed to detect the onset of SDC [33, 7], on the same data to verify the value of ϵ for which the transition to SDC occurs. Although these measures do not provide a complete description of the complex state, they are sensitive to the changes in the global features of the pattern.

4.2.2 Other Analysis Methods

First, we calculate the spatially varying roll curvature \mathcal{C} (see Section 2.6) as a measure of the structure of the pattern in the experimental data. In Fig. 4.10 (a), \mathcal{C} over many patterns is shown as a function of ϵ . The increase in the slope at $\epsilon = 0.75$

indicates a change in the curvature due to the presence of the spirals and the center defects. We note that cold and hot flows have nearly the same κ at a given value of ϵ . Second, we compute the time averaged structure factor $S(\mathbf{k})$ by a moderate amount of uncorrelated space-time data. We averaged the structure function azimuthally to obtain a wave-number distribution from which we calculated the skewness S_3 and the excess kurtosis K_4 (see Section 2.5). As seen in Fig. 4.10 (b), the appearance of spirals triggered a sudden jump both in S_3 and K_4 . Furthermore, we averaged the structure function radially for each image to obtain the angular power distribution as a function of time. Fig. 4.9 represents the power spectra as angle-time plots for five increasing ϵ values. At each ϵ , 1000 images corresponding to roughly $4000t_v$ are used to produce the plots. The horizontal and the vertical axes are the angle from 0 to π and the time, respectively. For $\epsilon \leq 0.625$, there is a single orientation in the distribution indicating that the pattern is mostly composed of slightly curved rolls. On the other hand, for larger ϵ ($\epsilon \geq 0.750$) the distribution is more uniform due to the presence of spirals in the pattern. We quantify the angle-time plots using the intermittency fraction F_I [33] defined as the fraction of time in which the standard deviation of the distribution is greater than 30° . As demonstrated in Fig. 4.10 (c) showing F_I as a function of ϵ , the existence of spirals causes the roll orientations to have a more azimuthally symmetric distribution.

4.2.3 Information Entropy

We investigate the evolution of the homology states (Section 4.1.3) from the time series of Betti numbers constructed from successive computations in the time series of shadowgraph images. We record the probabilities p_i of the CH states, observed in five different sets of ϵ in the experiment, in descending order. Fig. 4.11 demonstrates the behavior of the probability distributions as a function of ϵ . The distribution shows lower decays with increasing ϵ , meaning that the CH states are getting more

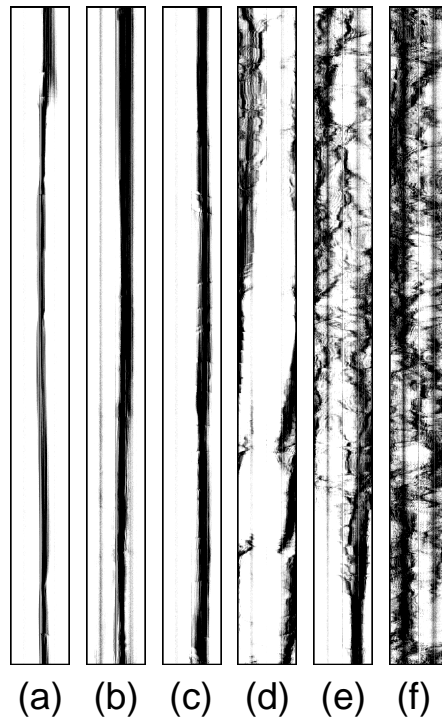


Figure 4.9: Angle-time plots of radially-averaged structure function: (a) $\epsilon = 0.375$, (b) $\epsilon = 5$, (c) $\epsilon = 0.625$, (d) $\epsilon = 0.750$, (e) $\epsilon = 0.875$, (f) $\epsilon = 1.0$. The power is greyscale coded with black corresponding to maximum power.

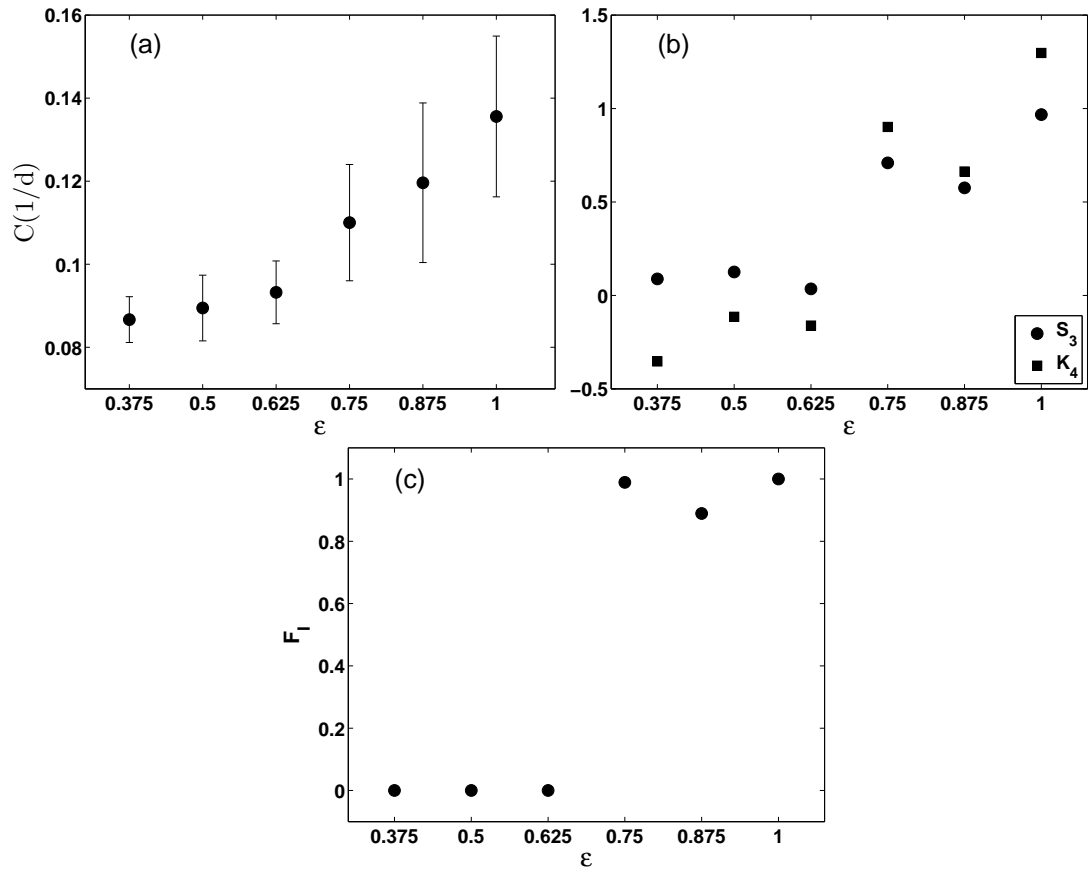


Figure 4.10: (a) the average roll curvature κ (b) the skewness S_3 and the excess kurtosis K_4 (c) the intermittency fraction F_I , as a function of ϵ detect the transition to SDC.

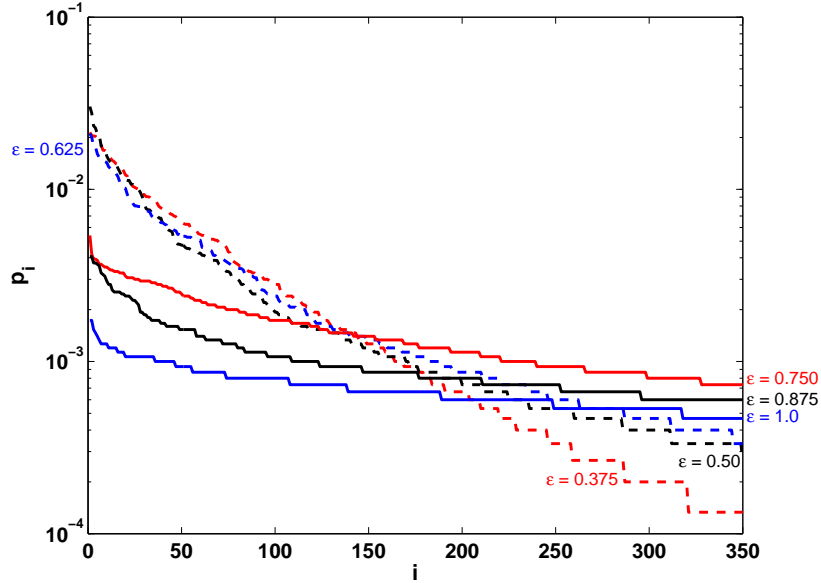


Figure 4.11: The 350 first largest probabilities p_i are shown on a logarithmic scale for five different increasing ϵ . 15,000 images corresponding to $50t_h$ have been used in computations at each ϵ .

equiprobable. At $\epsilon = 0.375$, the distribution exhibits a decay over 2 orders of magnitude (forming 98% of the total probability; $f = .98$) for the $D_{\text{CH}} = 350$ (see Eq. 4.1) first largest probabilities. The decay is less than an order of magnitude at $\epsilon = 1.0$, where the same number of probabilities ($D_{\text{CH}} = 350$) now only defines 25% of the probability ($f = .25$).

We apply KLD analysis (Section 4.1.4) to the same experimental data used in CH analysis. We obtain the eigenvalues λ_k in descending order for five values of ϵ . Fig. 4.12 demonstrates the behavior of eigenvalue spectra at the same ϵ values shown in Fig. 4.11. The spectrum displays lower decays with increasing ϵ , implying that more KLD modes are required to describe the dynamics accurately in the data. By keeping the $D_{\text{KLD}} = 350$ (see Eq. 4.3) first largest eigenvalues, the spectrum shows a decay over 3 orders of magnitude ($f = .97$) at $\epsilon = 0.375$. At $\epsilon = 1.0$, the same number of 350 eigenvalues specifies only 63% ($f = .63$) of the total spectrum, and the decay is less than an order of magnitude.

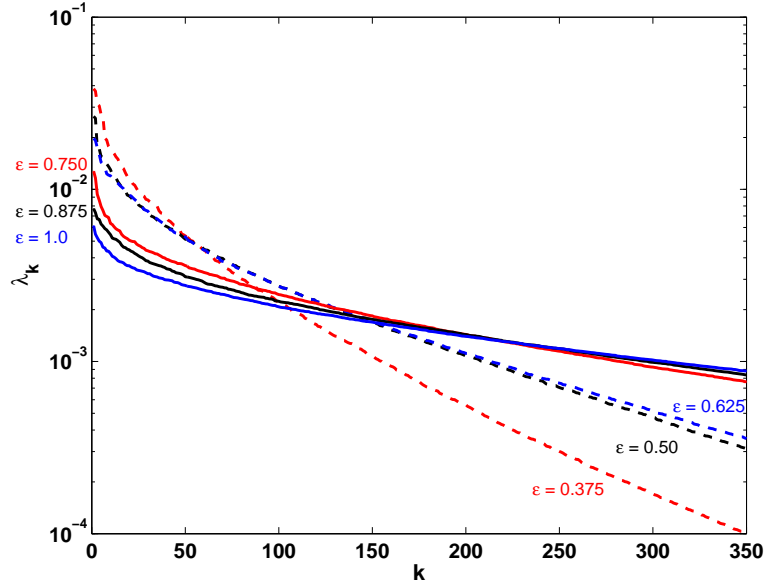


Figure 4.12: The 350 first largest eigenvalues λ_k are shown on a logarithmic scale for five different increasing ϵ . 15,000 images corresponding to $50t_h$ have been used in computations at each ϵ .

The variations in the number of KLD modes can be used as an indicator to detect changes in the dynamics. It is advantageous to obtain a measure that quantitatively characterizes eigenvalue spectra at different fractions. We use Shannon's information entropy [52] as a measure of the compressibility of complex data, which proportionally quantifies dynamical complexity present in data. By considering the normalized eigenvalues λ_k as the probabilities being in state k [22], the entropy is given by

$$S_{\text{KLD}} = - \sum_k \lambda_k \log \lambda_k, \quad (4.4)$$

measured in nats. A similar connection between the information entropy and CH can also be made to quantify probabilities constructed from the Betti numbers;

$$S_{\text{CH}} = - \sum_i p_i \log p_i. \quad (4.5)$$

In Fig. 4.13, the behavior of S_{KLD} and S_{CH} are shown as a function of five different ϵ values for different values of f . The monotonically increasing behavior of entropies

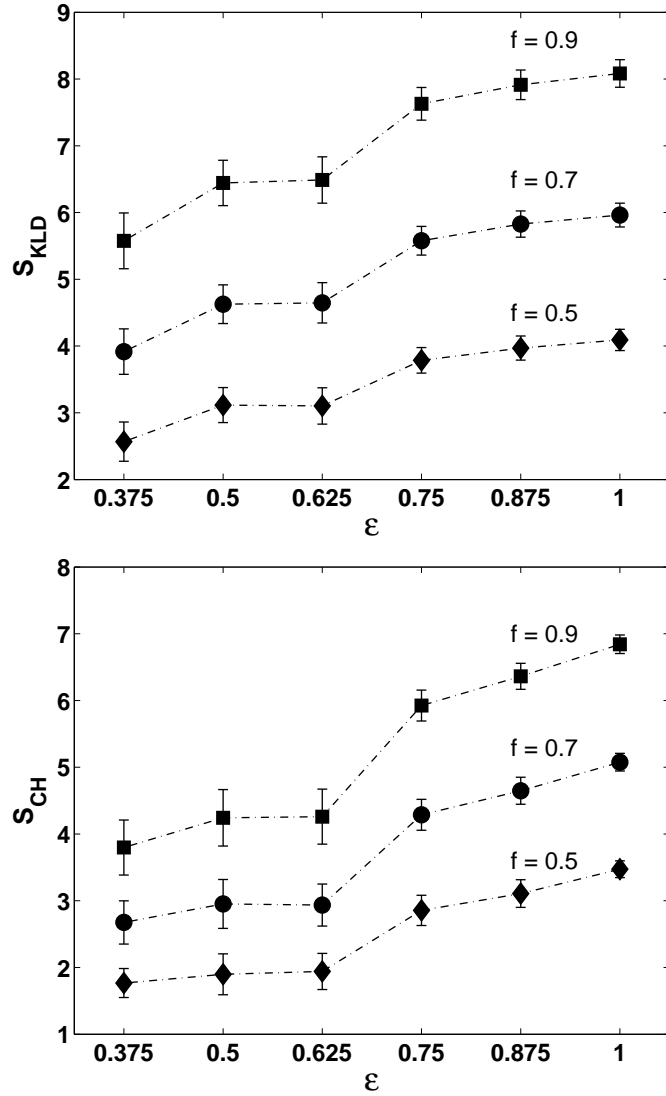


Figure 4.13: Information entropies S_{KLD} and S_{CH} are shown as a function of ϵ in the experiments at different f . At each ϵ , 15,000 images recorded in $50t_h$ are used to compute the entropies. The error bars are the statistical standard error based on the eigenvalue spectra and the probability distributions.

appears not to depend on the choice of f . The jumps in both entropy values between $\epsilon = 0.625$ and $\epsilon = 0.75$ correspond to the transition to SDC observed in the experiments. S_{CH} is more sensitive to this transition. Alterations in the roll curvature and orientation can effect the number of required KLD modes for accurate description of the system. Homology of a pattern, on the other hand, does not necessarily change unless the connectivity within the pattern changes under the influence of the defects. SDC is an interplay between spirals and other roll defects. After the transition, S_{KLD} and S_{CH} increase approximately linearly with ϵ , expressing that the states defined by the outputs of both methods become more and more equally likely as the complexity of the pattern increases. S_{CH} and S_{KLD} have similiar responses below the transition; both show a slight increase between $\epsilon = 0.375$ and $\epsilon = 0.5$, where the nonspiral defects start to appear in more interior regions of the pattern.

CHAPTER V

CONCLUSION

We have studied chaotic hot and cold flow patterns acquired from Rayleigh-Bénard convection (RBC) experiments performed under well-controlled conditions. By means of the output of computational homology (Betti numbers), we have efficiently measured not only the spatial structures of the patterns but also their spatio-temporally chaotic dynamics in large experimental data sets. We have compared homology results to other well-known pattern characterization techniques, and showed that homology reveals essential quantitative features of the patterns that other methods fail to detect. We have also demonstrated that similar information about the dynamics of the patterns captured by other techniques can be extracted more rapidly and effectively from computational homology.

In chapter 3, we showed that homology is a quantitatively useful tool to investigate the breakdown of the Oberbeck-Boussinesq (OB) approximation (the breaking of the reflection symmetry) in laboratory and numerical studies of thermal convection. We analyzed the data acquired under a range of experimental conditions where non-Oberbeck-Boussinesq effects (NOB), measured by the Busse parameter Q ($0.65 \leq Q \leq 2.80$), are systematically varied. The asymmetries between cold and hot flows due to the NOB effects were measured by the difference between time-averaged Betti numbers, i.e, by the order parameter $\langle \Delta\beta_0 \rangle = \langle \beta_{0c} - \beta_{0h} \rangle$. (These asymmetries are not observable by conventional statistical measures (Section 3.4)). We obtained a single curve of the order parameter $\langle \Delta\beta_0 \rangle$ as solely a function Q (Fig. 3.8), showing that the strength of NOB effects can be readily measured by homology analysis of patterns. The question still remained unanswered is what physical mechanism is responsible

for the dependence of $\langle \Delta\beta_0 \rangle$ on Q , especially in the state of spiral defect chaos. We believe that the topological asymmetry is caused by a defect mechanism intrinsic to NOB convection. Our results suggest that homology can be used in a wide variety of cases in fluid dynamics where NOB effects play an important role, for example, in the atmospheric sciences where OB approximation is extensively used. Furthermore, homology may offer new insights in other pattern forming complex systems which exhibit symmetry breaking.

In chapter 4, we introduced the dimension D_{CH} of computational homology (CH) to measure the number of degrees of freedom (DOF) of extensively chaotic systems from large experimental data sets. We attained D_{CH} at given control parameters in experiments from the probability distribution of homology states constructed from long time series of Betti numbers. We acquired analogous dimension D_{KLD} at the same parameter values from normalized eigenvalue spectrum obtained by a modified Karhunen-Loève decomposition (KLD). (Computing D_{KLD} from conventional KLD is impractical in large data sets like ours; the modified KLD is only applicable to the systems with translational or rotational symmetries). Despite the fact that both methods quantify the dynamics in a different manner, we demonstrated that D_{CH} and D_{KLD} scale at similar rates with system size as new chaotic DOF enter the dynamics. In particular, from converged estimates of D_{KLD} and D_{CH} , we showed that the state of spiral defect chaos (SDC) is extensively chaotic (Fig. 4.6), i.e, the number of DOF scales linearly with the system size; moreover, we found the presence of physical boundaries in experiments leads to deviations from extensive scaling that are similar for both methodologies (Fig. 4.7). Relating experimentally accessible measures of the number of DOF (e.g., D_{CH} and D_{KLD}) to more direct measures (e.g., the Lyapunov dimension D_λ) remains an open question. Recent direct simulations of RBC by Duggleby and Paul [17] yielded the relationship $D_{\text{KLD}} \approx 19.7D_\lambda$ from the variation of both dimensions with a range of system sizes $6 \leq \Gamma \leq 15$ in a cylindrical



Figure 5.1: A space-time block formed from a time series of binary images for hot flows and a slice taken from the block are shown. The homology for the space-time block yields the number of distinct components ($\beta_{0h} = 32$), the number of tunnels through the block ($\beta_{1h} = 55$), and the number of cavities enclosed ($\beta_{2h} = 10$).

convection cell. The creation and annihilation of defects, as a global signature of the complex spatio-temporal behavior of SDC, are the primary reasons for the variations in topological states, and D_λ may be closely related to their statistics [19]. Our results suggest that examining the effect of finite system size on D_λ may provide a way to link D_λ quantitatively to D_{CH} and D_{KLD} . In this regard, future studies that couple RBC laboratory experiments with numerical simulations with realistic boundary conditions at the same parameter values would be of greatest value.

Furthermore, in chapter 4, information entropy S_{CH} was obtained from the probability distributions constructed from a time series of Betti numbers to identify different spatio-temporal states at different control parameters in experiments. Specifically, we used S_{CH} to detect the value of the control parameter ϵ for which a distinct transition to SDC occurs in experiments (Fig. 4.13). SDC is subjected to different selection mechanisms based on the aspect ratio Γ [7]. The value of ϵ measured at the onset of SDC is different for different values of Γ . We found the state of SDC for $\epsilon > 0.625$ in an experiment with $\Gamma = 35$. In previous experimental studies, the state of SDC was observed for $\epsilon > 0.24$ and $\epsilon > 0.55$ in larger cells with $\Gamma = 78$ [43] and $\Gamma = 40$ [33], respectively. The origin of this Γ dependence is still unknown. S_{CH} might provide

further understanding for the lateral size dependence on the SDC transition observed in experiments as a function of Γ . Moreover, these measures can also be used to study transitions from a more ordered state to a complex state in other systems; for example, they can be used to investigate different mechanisms of spiral wave breakup in cardiac arrhythmia [21].

Homology can be extended to higher dimensions by performing an analysis on space-time blocks formed from time series of two-dimensional shadowgraph images. Fig. 5.1 shows a space-time block formed by subsequent images describing the evolution of hot flows. In addition to the zeroth and the first Betti numbers, the computation yields the second Betti number representing the number of enclosed cavities within the hot space-time block. Although the homology analysis, in this dissertation, is only based on the Betti numbers obtained from individual images, space-time homology analysis, in the future, may offer further insights into the chaotic dynamics in Rayleigh-Bénard convection.

APPENDIX A

NONDIMENSIONALIZED BOUSSINESQ EQUATIONS

Here, we derive well-known nondimensionalized Oberbeck-Boussinesq equations which are widely used to study Rayleigh-Bénard convection [10]. We consider a horizontal layer of convective fluid of depth d , which is laterally unbounded in the xy -plane and confined in the z -direction by two solid plates. The state of a fluid is described by two scalars and one vector field: pressure $P(\mathbf{x}, t)$, temperature $T(\mathbf{x}, t)$, and velocity $\mathbf{V}(\mathbf{x}, t)$. The equations describing the state of an incompressible convective fluid are the Navier-Stokes equation

$$\frac{D\mathbf{V}}{Dt} = \partial_t \mathbf{V} + (\mathbf{V} \cdot \nabla) \mathbf{V} = \frac{1}{\rho} \mathbf{F} - \frac{1}{\rho} \nabla P + \nu \nabla^2 \mathbf{V} \quad (\text{A.1})$$

with the incompressibility condition

$$\nabla \cdot \mathbf{V} = 0 \quad (\text{A.2})$$

, and the heat equation

$$\frac{DT}{Dt} = \partial_t T + (\mathbf{V} \cdot \nabla) T = \kappa \nabla^2 T \quad (\text{A.3})$$

where D indicates the material (Lagrangian) derivative, $\mathbf{F} = -g\rho(T)\hat{\mathbf{z}}$ is the gravitational force per unit volume, ν the kinematic viscosity, ρ the density, κ the thermal diffusivity, and g the acceleration of gravity. In the Boussinesq approximation, ν , κ and the thermal expansion coefficient α are assumed to vary little within the layer. The density is considered to be constant in the equations except in the buoyancy term which drives the convective flow. For small temperature difference $\Delta T = T_b - T_t$ (T_b and T_t are the bottom and the top layer temperature, respectively) between the layers and for small α , we can write the density as a linear function of the temperature

$$\rho = \tilde{\rho}(1 - \alpha(T - \bar{T}))$$

where the reference density $\tilde{\rho}$ is measured for the mean temperature $\bar{T} = (T_b + T_t)/2$ of the cell.

In the uniform base state, e.g, heat is only transported by conduction, there is no fluid motion in the convectionless state, i.e,

$$\mathbf{V}^{cond} = 0 \quad (\text{A.4})$$

We choose the coordinate along the z-direction such that the top and the bottom layer of the fluid is at $z = d/2$ and $z = -d/2$, respectively. The steady state solution for Eq. A.3 with the boundary conditions $T^{cond}(z = d/2) = T_t^{cond}$ and $T^{cond}(z = -d/2) = T_b^{cond}$ yields

$$T^{cond}(z) = \frac{\Delta T^{cond}}{d}z + \bar{T}^{cond} \quad (\text{A.5})$$

and from Eq. A.1 we get

$$-g\tilde{\rho}^{cond}(1 - \alpha(T^{cond} - \bar{T}^{cond}))\hat{\mathbf{z}} = \nabla P$$

from which we obtain an expression for the steady state pressure with the help of Eq. A.5

$$P^{cond}(z) = -g\tilde{\rho}^{cond}\left(z + \frac{\alpha\Delta T^{cond}}{2d}z^2\right) + \tilde{P}^{cond}$$

Next, we examine the behavior of infinitesimal disturbances to the base state solutions. We define $\Sigma = \mathbf{V} - \mathbf{V}^{cond}$, $\Theta = T - T^{cond}$ and $\Psi = P - P^{cond}$, and we linearize the equations with respect to the perturbed quantities $\Sigma = (\Sigma_x, \Sigma_y, \Sigma_z)$, Θ and Ψ . From Eq. A.1, Eq. A.2 and Eq. A.3, we reach the following linearized equations with the use of Eq. A.4, Eq. A.5, and Eq. A.6

$$\begin{aligned} \partial_t \Sigma + (\Sigma \cdot \nabla) \Sigma &= g\alpha\Theta\hat{\mathbf{z}} - \frac{1}{\rho}\nabla\Psi + \nu\nabla^2\Sigma \\ \nabla \cdot \Sigma &= 0 \\ \partial_t \Theta + (\Sigma \cdot \nabla)\Theta &= \kappa\nabla^2\Theta + \Sigma_x \frac{\Delta T}{d} \end{aligned} \quad (\text{A.6})$$

where the system is perturbed while \bar{T} is kept constant and the fluid properties are evaluated at \bar{T} .

We can further simplify the equations by non-dimensionalizing them. In non-dimensionalization, a natural choice for the length scale is the depth of the fluid layer d . On the other hand, there are two possible choices for the time scale based on the viscous time scale d^2/ν or the diffusive time scale d^2/μ . Both may have different implications in terms of reducing the nonlinearities in the equations for the fluids having large or small Prandtl number $\sigma = \nu/\mu$. For gases, σ is near one so all nonlinear terms are important in the equations describing the fluid state. We rescale Eq. A.6 with the non-dimensional variables \mathbf{x}' , t' , Σ' , Θ' , and Ψ'

$$\mathbf{x} = d \mathbf{x}', t = \frac{d^2}{\nu} t', \Sigma = \frac{\nu}{d} \Sigma', \Theta = \frac{\nu^2}{g\alpha d^3} \Theta', \Psi = \frac{\rho\nu^2}{d^2} \Psi'$$

, then Eq. A.6 takes the form

$$\partial_t \Sigma + (\Sigma \cdot \nabla) \Sigma = \Theta \hat{\mathbf{z}} - \nabla \Psi + \nabla^2 \Sigma \quad (\text{A.7})$$

$$\nabla \cdot \Sigma = 0 \quad (\text{A.8})$$

$$\sigma(\partial_t \Theta + (\Sigma \cdot \nabla) \Theta) = \nabla^2 \Theta + R \Sigma_x \quad (\text{A.9})$$

where we dropped the primes and introduced two dimensionless number; the Rayleigh number R and the Prandtl number σ

$$R = \frac{\alpha g \Delta T d^3}{\nu \kappa}, \sigma = \frac{\nu}{\kappa}$$

Eq. A.7, Eq. A.8 and Eq. A.9 are known as the nondimensionalized Oberbeck-Boussinesq equations.

APPENDIX B

GAS PROPERTIES

In order to extract more information about the convective state in experiments, it is required to know some of the thermophysical properties of the convective fluids. Mainly, we use two convective single phase gaseous; carbon dioxide (CO_2) and sulfur hexafluoride (SF_6). In the following, we derive some important fluid properties for these gaseous.

The virial equation of state defining the deviation of a real gas from an ideal gas state with intermolecular interactions at pressure P and temperature T with specific gas constant R can be written as

$$\frac{P}{RT} = \rho + C_1(T)\rho^2 + C_2(T)\rho^3 + C_3(T)\rho^4 + \dots \quad (\text{B.1})$$

where, the first virial coefficient is set to one, C_1 is the second virial coefficient, C_2 the third, C_3 is the fourth, and so on. We neglect higher order corrections which are insensitive to density calculations. Specific gas constants for CO_2 and SF_6 are $R_{\text{CO}_2} = 1.889245$ and $R_{\text{SF}_6} = 0.569268$ in $\text{bar cm}^3/\text{K gr}$, respectively.

B.1 Carbon Dioxide

For the density calculations we obtain virial coefficients from Eq. 5.68 of Vukalovich and Altunin [54], where coefficients are defined up to eighth order, i.e, $C_7(T)$. However, first four coefficients are good enough for an accurate description of the state in

single phase region. These coefficients in Ref. [54] can be rewritten as

$$C_1(T) = 0.486590 + 47.199230 (96 + 0.003287310980T)^{-1} - 304.20 \frac{1.90843 + 5.3510e^{-0.003805391190T}}{T} - 58315340550T^{-8} \quad (\text{B.2a})$$

$$C_2(T) = 2.39169 - 304.20 \frac{6.96190 - 12.1824e^{-0.003805391190T}}{T} + 635643.8252T^{-2} - 94095430.63T^{-3} \quad (\text{B.2b})$$

$$C_3(T) = -1.69007 + 304.20 \frac{10.2469 - 6.38963e^{-0.003805391190T}}{T} - 1363421.826T^{-2} + 206257780.7T^{-3} \quad (\text{B.2c})$$

where T is in Kelvin and P is in bar. And their derivatives with respect to temperature can be obtained,

$$\begin{aligned} \frac{d}{dT}C_1 &= -0.1551585470 (96 + 0.003287310980T)^{-2} + 6.194317601 \\ &\frac{e^{-0.003805391190T}}{T} + 304.20 \frac{1.90843 + 5.3510e^{-0.003805391190T}}{T^2} + \\ &4.665227244 \times 10^{19} T^{-9} \end{aligned} \quad (\text{B.3a})$$

$$\begin{aligned} \frac{d}{dT}C_2 &= 304.20 \frac{6.96190 - 12.1824e^{-0.003805391190T}}{T^2} - \\ &14.10234624 \frac{e^{-0.003805391190T}}{T} - 1271287.650T^{-3} + \\ &282286291.9T^{-4} \end{aligned} \quad (\text{B.3b})$$

$$\begin{aligned} \frac{d}{dT}C_3 &= -304.20 \frac{10.2469 - 6.38963e^{-0.003805391190T}}{T^2} + \\ &7.396635688 \frac{e^{-0.003805391190T}}{T} + 2726843.652T^{-3} - \\ &618773342.1T^{-4} \end{aligned} \quad (\text{B.3c})$$

We solve Eq.(B.1) numerically with the coefficients in Eq.(B.2) for the density values $\rho < .2 \text{ gr/cm}^3$, which is more than twice the maximum density value that could be observed in experiments for the range of pressure (20 to 40 bar) and temperature (10 to 60 °C). Density values obtained by this way produce the data of Iwasaki and Takahaski [35] ($298.15 \text{ K} \leq T \leq 323.15 \text{ K}$ and $23.89 \text{ bar} \leq P \leq 41.05 \text{ bar}$) with a

mean deviation of less than .9% and the data of Altunin and Gadetskii [2] (304.20 K $\leq T \leq$ 323.15 K and 25 bar $\leq P \leq$ 35 bar) with less than .02% for gaseous CO₂.

To obtain the specific heat capacities c_v at constant volume V and c_p at constant pressure P , we use the following well-known thermodynamic equation;

$$c_p - c_v = -T \left(\frac{\partial V}{\partial T} \right)_P^2 \left(\frac{\partial V}{\partial P} \right)_T^{-1} = \frac{T}{\rho^2} \left(\frac{\partial P}{\partial T} \right)_\rho^2 \left(\frac{\partial \rho}{\partial P} \right)_T, \quad (\text{B.4})$$

which can be rewritten using Eq.(B.1)

$$c_p - c_v = R \left(1 + C_1\rho + C_2\rho^2 + C_3\rho^3 + T\rho \frac{d}{dT}C_1 + T\rho^2 \frac{d}{dT}C_2 + T\rho^3 \frac{d}{dT}C_3 \right)^2 (1 + 2C_1\rho + 3C_2\rho^2 + 4C_3\rho^3)^{-1} \quad (\text{B.5})$$

where c_v is generally defined as

$$c_v - c_v^o = \int_0^\rho \frac{-T}{\rho^2} \left(\frac{\partial^2 P}{\partial T^2} \right)_\rho d\rho \quad (\text{B.6})$$

and taking the integration with the use of Eq.(B.1) yields

$$\begin{aligned} \frac{c_v - c_v^o}{R} = & \left(-2/3 T \frac{d}{dT}C_3 - 1/3 T^2 \frac{d^2}{dT^2}C_3 \right) \rho^3 + \\ & \left(-T \frac{d}{dT}C_2 - 1/2 T^2 \frac{d^2}{dT^2}C_2 \right) \rho^2 + \\ & \left(-2T \frac{d}{dT}C_1 - T^2 \frac{d^2}{dT^2}C_1 \right) \rho. \end{aligned} \quad (\text{B.7})$$

c_v^o is given in a functional form in Eq.(6.6) of Vukalovich and Altunin [54], we write it an explicit form as a function of temperature only;

$$\begin{aligned} \frac{c_v^o}{R} = & 5/2 + 1843200 e^{960 T^{-1}} T^{-2} \left(e^{960 T^{-1}} - 1 \right)^{-2} + \\ & 3956121 e^{1989 T^{-1}} T^{-2} \left(e^{1989 T^{-1}} - 1 \right)^{-2} + \\ & 11336689 e^{3367 T^{-1}} T^{-2} \left(e^{3367 T^{-1}} - 1 \right)^{-2}. \end{aligned} \quad (\text{B.8})$$

Therefore, at a given temperature and pressure and with a known density ρ , c_v and c_p in J/gr K can be calculated with the help of Eq.(B.2) and Eq.(B.3).

Table B.1: Coefficients a_{ij}^λ for carbon dioxide are obtained from a fit of the polynomial in Eq.(B.10) to the data in Ref. [54] with 31 points. The max and mean percent deviations between the data and the conductivities acquired from Eq.(B.10) are 0.054% and 0.014%, respectively.

$a_{ij}^\lambda \times 10^0$	0	1	2	3
0	0.014687705810562	0.000081952374639	0.000000008008702	-0.000000000303030
1	0.000122955979942	-0.000001427975840	0.000000003805913	0.000000000056818
2	-0.000001666125508	0.000000074206346	-0.000000000566017	-0.000000000000505
3	0.000000069953105	-0.000000002494048	0.000000000029690	-0.000000000000114

Table B.2: Coefficients a_{ij}^μ for carbon dioxide are obtained from a fit of the polynomial in Eq.(B.11) to the data in Ref. [54] with 39 points. The max and mean percent deviations between the data and the shear viscosities acquired from Eq.(B.11) are 0.493% and 0.138%, respectively.

$a_{ij}^\mu \times 10^4$	0	1	2	3
0	0.137327946387131	0.000380303947705	0.000002935099576	-0.000000027036114
1	0.000311238325553	0.000023913239482	-0.000001014429920	0.000000009348695
2	0.000013337193922	-0.000001929682463	0.000000068026423	-0.000000000622282
3	0.000000069918894	0.000000020944756	-0.000000000943756	0.000000000009249

The isobaric thermal expansion coefficient

$$\alpha = -\frac{1}{\rho} \left(\frac{\partial \rho}{\partial T} \right)_P \quad (\text{B.9})$$

can be obtained either from a high order polynomial fitting or from a numerical differentiation. We use the later with a central differencing scheme for ρ .

We obtain the thermal conductivity λ and shear viscosity μ from polynomial fittings

$$\lambda = \sum_{i=0}^{i=3} \sum_{j=0}^{j=3} a_{ij}^\lambda P^i T^j \quad (\text{B.10})$$

$$\mu = \sum_{i=0}^{i=3} \sum_{j=0}^{j=3} a_{ij}^\mu P^i T^j \quad (\text{B.11})$$

to the data given in Table 10.5 and Table 9.10 of Ref. [54], respectively, for the range of pressure in bar (10 to 40 bar) and temperature in °C (0 to 70 °C). The empirical coefficients a_{ij}^λ and a_{ij}^μ are given in Table B.1 and B.2. We can therefore obtain the

Prandtl number σ from the kinematic viscosity ν and the thermal diffusivity κ :

$$\nu = \frac{\mu}{\rho} \quad (\text{B.12})$$

$$\kappa = \frac{\lambda}{\rho c_p} \quad (\text{B.13})$$

$$\sigma = \frac{\nu}{\kappa}. \quad (\text{B.14})$$

Conductivities obtained by Eq.(B.10) agrees well with the experimental data of Ulybin and Bakulin [53] ($280 \text{ K} \leq T \leq 300 \text{ K}$ and $10 \text{ bar} \leq P \leq 40 \text{ bar}$) by less than 2.5%. Shear viscosities obtained by Eq.(B.11) agrees by 4.6% with the data of Iwasaki and Takahashi [35] ($298.15 \text{ K} \leq T \leq 323.15 \text{ K}$ and $23.89 \text{ bar} \leq P \leq 41.05 \text{ bar}$). Furthermore, kinematic viscosities obtained by Eq.(B.12) agrees by less than 4.4% with the data of Alexanders and Hurly [20] ($285 \text{ K} \leq T \leq 330 \text{ K}$ and $27.08 \text{ bar} \leq P \leq 31.45 \text{ bar}$). Some thermophysical properties of CO_2 are shown in Table B.3 at a given temperature and pressure.

B.2 Sulfur Hexafluoride

For density calculations, we only keep virial coefficients $C_1(T)$ and $C_2(T)$ and ignore higher ones in Eq.(B.1). We obtain virial coefficients as a function of T ($270 \text{ K} \leq T \leq 340 \text{ K}$) from polynomial fits to the coefficient data of Funke et al. [23]

$$C_k(T) = \sum_{i=0}^{i=6} c_{ik} T^i, \quad k = 1, 2 \quad (\text{B.15})$$

where $C_1(T)$ and $C_2(T)$ are given in cm^3/mol and $(\text{cm}^3/\text{mol})^2$, respectively. The coefficients c_{ik} are given in Table B.4. Similar to the carbon dioxide case, we obtain the density at given T and P by solving Eq.(B.1) numerically. Density values we obtain reproduce the data of Scalabrin et al. [49] ($275 \text{ K} \leq T \leq 325 \text{ K}$ and $5 \text{ bar} \leq P \leq 20 \text{ bar}$) with a mean deviation of less than .0005% and the data of Guder and Wagner [27] ($275 \text{ K} \leq T \leq 340 \text{ K}$ and $5 \text{ bar} \leq P \leq 20 \text{ bar}$) with less than .009% for single phase region.

Table B.3: Thermophysical Properties of CO₂ at given temperature and pressure.

P(bar)	T(°C)	$\rho(\text{kg}/\text{m}^3)$	$c_p(\text{J}/(\text{kg}\cdot\text{K}))$	$\mu(\text{Pa}\cdot\text{s}) \times 10^5$	$\nu(\text{m}^2/\text{s}) \times 10^7$	$\lambda(\text{W}/\text{mK}) \times 10^3$	$\kappa(\text{m}^2/\text{s}) \times 10^7$	$\alpha(1/\text{K}) \times 10^3$	σ
25.00	20.00	52.92	1107.31	1.58	2.99	18.96	3.24	5.70	0.92
25.00	30.00	50.13	1068.75	1.61	3.22	19.59	3.66	5.16	0.88
25.00	40.00	47.72	1043.13	1.65	3.45	20.24	4.07	4.73	0.85
30.00	20.00	66.17	1198.07	1.62	2.45	19.69	2.48	6.50	0.99
30.00	30.00	62.25	1137.33	1.64	2.64	20.24	2.86	5.75	0.92
30.00	40.00	58.94	1097.16	1.67	2.84	20.84	3.22	5.19	0.88
40.00	20.00	97.38	1471.38	1.71	1.76	21.51	1.50	9.00	1.17
40.00	30.00	89.77	1324.68	1.71	1.91	21.81	1.83	7.41	1.04
40.00	40.00	83.82	1235.63	1.73	2.06	22.23	2.15	6.38	0.96

Table B.4: Coefficients c_{ik} are obtained from a fit of the polynomial in Eq.(B.15) to the virial coefficient data in Ref. [23].

	$c_{i1} \times 10^{-3}$	$c_{i2} \times 10^{-9}$
0	-9.493116566185545	-1.679567477438810
1	0.105170488343965	0.033047448102228
2	-0.000466725700421	-0.000270562967620
3	0.000000949472287	0.000001179747489
4	-0.000000000735768	-0.000000002889438
5	0.000000000000000	0.000000000003769
6	0.000000000000000	-0.000000000000002

We acquire heat capacities c_v and c_p from bilinear interpolations in the data of Guder and Wagner [27] for the range of pressure 5 to 20 bar and temperature 270 to 350 K with 68 points for each heat capacities. We also check validation of Eq.(B.5), i.e. deriving c_p from c_v . However, it introduces roughly 10% error which we believe due to the absence of higher order virial coefficients in calculations.

We derive the thermal conductivity λ from a polynomial fit in Eq.(B.10) to the data of Tanaka et al. [51] and of Bakulin and Ulybin [3] for the range of pressure in bar (4.90 to 20.60 bar) and temperature in K (268.60 to 348.15 K). The shear viscosity is also acquired from a polynomial fit in Eq.(B.11) to the data of Hurly et al. [34] and of Wilhelm et al. [55] for the range of pressure in bar (4.85 to 20.43 bar) and temperature in K (298.15 to 350.00 K). The coefficients obtained a_{ij}^λ and a_{ij}^μ are given in Table B.5 and B.6. Conductivities obtained agrees with the data of Kestin and Imaishi [37] ($297.66 \text{ K} \leq T \leq 297.71 \text{ K}$ and $7.99 \text{ bar} \leq P \leq 22.00 \text{ bar}$) by 3.9%. Shear viscosities agrees by 0.17% with the data of Hoogland et al [29] ($298.11 \text{ K} \leq T \leq 333.17 \text{ K}$ and $1.04 \text{ bar} \leq P \leq 22.27 \text{ bar}$). Kinematic viscosity derived by extrapolation agrees by 1.85% with the data of Alexanders and Hurly [20] ($T = 273.16 \text{ K}$ and $4.92 \text{ bar} \leq P \leq 10.00 \text{ bar}$). Some thermophysical properties of SF₆ are shown in Table B.7 at a given temperature and pressure.

Table B.5: Coefficients a_{ij}^λ for sulfur hexafluoride are obtained from a fit of the polynomial in Eq.(B.10) to the data in Ref. [51] and Ref. [3] with 33 points. The max and mean percent deviations between the combined data and the conductivities acquired from Eq.(B.10) are 1.651% and 0.425%, respectively.

$a_{ij}^\lambda \times 10^0$	0	1	2	3
0	0.000042484300260	0.000292256061780	0.001721854423803	-0.000046172772550
1	0.000107395927164	-0.000034470624355	-0.000013095202822	0.000000372564981
2	-0.000000519101832	0.000000214849321	0.000000030691498	-0.000000000943400
3	0.000000001004146	-0.000000000340530	-0.000000000020780	0.000000000000729

Table B.6: Coefficients a_{ij}^μ for sulfur hexafluoride are obtained from a fit of the polynomial in Eq.(B.11) to the data in Ref. [34] and Ref. [55] with 174 points. The max and mean percent deviations between the combined data and the shear viscosities acquired from Eq.(B.11) are 0.161% and 0.028%, respectively.

$a_{ij}^\mu \times 10^7$	0	1	2	3
0	0.005802216552301	0.000177451595046	0.007659856682402	0.170292955119589
1	0.623383021287037	-0.012890441326356	-0.001644234942827	-0.001424879790229
2	-0.000547832044993	0.000082574337738	0.000009382411101	0.000004001750561
3	0.000000569018434	-0.000000126893967	-0.000000013224966	-0.000000003769547

Table B.7: Thermophysical Properties of SF₆ at given temperature and pressure.

P(bar)	T(°C)	$\rho(\text{kg}/\text{m}^3)$	$c_p(\text{J}/(\text{kg}\cdot\text{K}))$	$\mu(\text{Pa}\cdot\text{s}) \times 10^5$	$\nu(\text{m}^2/\text{s}) \times 10^7$	$\lambda(\text{W}/\text{mK}) \times 10^3$	$\kappa(\text{m}^2/\text{s}) \times 10^7$	$\alpha(1/\text{K}) \times 10^3$	σ
10.00	25.00	67.15	727.19	1.55	2.31	13.28	2.72	5.14	0.85
10.00	35.00	63.93	733.23	1.60	2.50	13.96	2.98	4.72	0.84
10.00	45.00	61.09	740.92	1.64	2.69	14.70	3.25	4.38	0.83
15.00	25.00	110.06	789.72	1.59	1.44	13.95	1.60	6.94	0.90
15.00	35.00	103.19	779.84	1.63	1.58	14.49	1.80	6.01	0.88
15.00	45.00	97.50	777.30	1.68	1.72	15.15	2.00	5.36	0.86
20.00	25.00	165.67	921.60	1.66	1.00	15.18	0.99	10.73	1.01
20.00	35.00	150.88	859.89	1.69	1.12	15.51	1.20	8.23	0.940
20.00	45.00	140.01	832.58	1.73	1.24	16.01	1.37	6.84	0.90

REFERENCES

- [1] AHLERS, G., DRESSEL, B., OH, J., , and PESCH, W., “Strong non-Boussinesq effects near the onset of convection in a fluid near its critical point,” *J. Fluid Mech.*, vol. 642, pp. 15–48, 2009.
- [2] ALTUNIN, V. V. and GADETSKII, O. G., “Equation of state and thermodynamic properties of liquid and gaseous carbon dioxide,” *Teploenergetika*, vol. 18, no. 3, pp. 81–84, 1971.
- [3] BAKULIN, S. S. and ULYBIN, S. A., “Thermal conductivity of sulfur hexafluoride at temperatures of 230–350 K and pressures up to 50 MPa,” *High Temperature*, vol. 16, no. 1, pp. 46–52, 1978.
- [4] BÉNARD, H., “Les tourbillons cellulaires dans une nappe liquide,” *Rev. Gen. Sciences Pure Appl.*, vol. 11, pp. 1261–1271, 1309–1328, 1900.
- [5] BÉNARD, H., “Les tourbillons cellulaires dans une nappe liquide transportant de la chaleur par convection en regime permanent,” *Ann. Chim. Phys.*, vol. 23, pp. 62–144, 1901.
- [6] BODENSCHATZ, E., DE BRUYN, J. R., AHLERS, G., and CANNELL, D. S., “Transition between patterns in thermal convection,” *Phys. Rev. Lett.*, vol. 67, pp. 3078–3081, 1991.
- [7] BODENSCHATZ, E., PESCH, W., and AHLERS, G., “Recent developments in Rayleigh-Bénard convection,” *Annu. Rev. Fluid Mech.*, vol. 32, pp. 709–778, 2000.
- [8] BOUSSINESQ, J., *Théorie Analytique de la Chaleur*, vol. 2. Paris: Gauthier-Villars, 1903.
- [9] BUSSE, F. H., “The stability of finite amplitude cellular convection and its relation to an extremum principle,” *J. Fluid Mech.*, vol. 30, pp. 625–649, 1967.
- [10] BUSSE, F. H., “Non-linear properties of thermal convection,” *Rep. Prog. Phys.*, vol. 41, pp. 1929–1967, 1978.
- [11] CHANDRASEKHAR, S., *Hydrodynamic and hydromagnetic stability*. Oxford: Clarendon Press, 1961.
- [12] CHOMP, *Computational Homology Project*, 2010. <http://chomp.rutgers.edu>.
- [13] CILIBERTO, S., PAMPALONI, E., and PERÉZ-GARCÍA, C., “Competition between different symmetries in convective patterns,” *Phys. Rev. Lett.*, vol. 61, pp. 1198–1201, 1988.

- [14] CROSS, M. C. and HOHENBERG, P. C., "Pattern formation outside of equilibrium," *Rev. Mod. Phys.*, vol. 65, pp. 851–1112, 1993.
- [15] DE BRUYN, J. R., BODENSCHATZ, E., MORRIS, S. W., TRAINOFF, S. P., HU, Y., CANNELL, D. S., and AHLERS, G., "Apparatus for the study of Rayleigh-Bénard convection in gases under pressure," *Rev. Sci. Instrum.*, vol. 67, pp. 2043–2067, 1996.
- [16] DEANE, A. E. and SIROVICH, L., "A computational study of Rayleigh-Bénard convection. part 1. Rayleigh number dependence," *J. Fluid Mech.*, vol. 222, pp. 231–250, 1991.
- [17] DUGGLEBY, A. and PAUL, M. R. *submitted to Computers and Fluids, arXiv:0905.4847v1*, 2009.
- [18] EGOLF, D. A. and GREENSIDE, H. S., "Relation between fractal dimension and spatial correlation length for extensive chaos," *Nature*, vol. 369, pp. 129–131, 1994.
- [19] EGOLF, D. A., MELNIKOV, I. V., PESCH, W., and ECKE, R. E., "Mechanism of extensive spatiotemporal chaos in Rayleigh-Bénard convection," *Nature*, vol. 404, pp. 733–736, 2000.
- [20] ESTRADA-ALEXANDERS, A. F. and HURLY, J. J., "Kinematic viscosity and speed of sound in gaseous CO , CO_2 , SiF_4 , SF_6 , C_4F_8 and NH_3 from 220 K to 375 K and pressures up to 3.4 MPa," *J. Chem. Thermodynamics*, vol. 40, pp. 193–202, 2008.
- [21] FENTON, F. H., CHERRY, E. M., HASTINGS, H. M., and EVANS, S. J., "Multiple mechanisms of spiral wave breakup in a model of cardiac electrical activity," *Chaos*, vol. 12, p. 852, 2002.
- [22] FRANZ, A. L., ROY, R., SHAW, L. B., and SCHWARTZ, I. B., "Changing dynamical complexity with time delay in coupled fiber laser oscillators," *Phys. Rev. Lett.*, vol. 99, pp. 053905–053905, 2007.
- [23] FUNKE, M., KLEINRAHM, R., and WAGNER, W., "Measurement and correlation of the (p, ρ, t) relation of sulphurhexafluoride (SF_6). i.the homogeneous gas and liquid region in the temperature range from 225 K to 340 K at pressures up to 12 MPa," *J. Chem. Thermodynamics*, vol. 34, pp. 717–734, 2002.
- [24] GAMEIRO, M., MISCHAIKOW, K., and KALIES, W., "Topological characterization of spatial-temporal chaos," *Phys. Rev. E*, vol. 70, p. 035203, 2004.
- [25] GETLING, A. V., *Rayleigh-Bénard convection: structures and dynamics*. Singapore: World scientific, 1998.
- [26] GOLDSTEIN, R. J., *Fluid mechanics measurements*. Pennsylvania: Taylor and Francis, 1996.

- [27] GUDER, C. and WAGNER, W., “A reference equation of state for the thermodynamic properties of sulfur hexafluoride SF_6 for temperatures from the melting line to 625 K and pressures up to 150 MPa,” *J. Phys. Chem. Ref. Data*, vol. 38, no. 1, pp. 33–94, 2002.
- [28] HEUTMAKER, M. S. and GOLLUB, J. P., “Wave-vector field of convective flow patterns,” *Phys. Rev. A*, vol. 35, pp. 242–260, 1987.
- [29] HOOGLAND, J. H. B., VANDENBERG, H. R., and TRAPPENIERS, N. J., “Measurements of the viscosity of sulfur hexafluoride up to 100 bar by a capillary-flow viscometer,” *Physica A*, vol. 134, no. 1, pp. 169–192, 1985.
- [30] HOOK, S. J. V., *Long-wavelength instability in surface-tension-driven Benard convection*. PhD thesis, The university of Texas at Austin, 1996.
- [31] HU, Y., ECKE, R., and AHLERS, G., “Convection near threshold for Prandtl numbers near 1,” *Phys. Rev. E*, vol. 48, pp. 4399–4413, 1993.
- [32] HU, Y., ECKE, R. E., and AHLERS, G., “Convection for Prandtl numbers near 1: Dynamics of textured patterns,” *Phys. Rev. E*, vol. 51, pp. 3263–3279, 1995.
- [33] HU, Y., ECKE, R. E., and AHLERS, G., “Transition to spiral-defect chaos in low Prandtl number convection,” *Phys. Rev. Lett.*, vol. 74, pp. 391–394, 1995.
- [34] HURLY, J. J., GILLIS, K. A., MEHL, J. B., and MOLDOVER, M. R., “The viscosity of seven gases measured with a greenspan viscometer,” *Int. J. Thermophys.*, vol. 24, no. 6, pp. 1441–1474, 2003.
- [35] IWASAKI, H. and TAKAHASHI, M., “Viscosity of carbon dioxide and ethane,” *J. Chem. Phys.*, vol. 74, no. 3, pp. 1930–1943, 1981.
- [36] KACZYNSKI, T., MISCHAIKOW, K., and MROZEK, M., *Computational Homology*. Newyork: Springer-Verlag, 2004.
- [37] KESTIN, J. and IMAISHI, N., “Thermal conductivity of sulfur hexafluoride,” *Int. J. Thermophys.*, vol. 6, no. 2, pp. 107–118, 1985.
- [38] KRISHAN, K., KURTULDU, H., SCHATZ, M. F., MADRUGA, S., GAMEIRO, M., and MISCHAIKOW, K., “Homology and symmetry breaking in Rayleigh-Bénard convection,” *Phys. Fluids*, vol. 19, p. 117105, 2007.
- [39] MADRUGA, S. and RIECKE, H., “Re-entrant hexagons in non-Boussinesq convection,” *J. Fluid Mech.*, vol. 548, pp. 341–360, 2006.
- [40] MADRUGA, S. and RIECKE, H., “Reentrant and whirling hexagons in non-Boussinesq convection,” *Eur. Phys. J. Special Topics*, vol. 146, pp. 279–290, 2007.

- [41] MADRUGA, S. and RIECKE, H., “Hexagons and spiral defect chaos in non-Boussinesq convection at low Prandtl numbers,” *Phys. Rev. E*, vol. 75, p. 026210, 2007.
- [42] MANNEVILLE, P., “Liapunov exponents for the Kuramoto-Sivashinsky model,” *Lecture Notes in Physics*, vol. 280, pp. 319–326, 1994.
- [43] MORRIS, S. W., BODENSCHATZ, E., CANNEL, D. S., and AHLERS, G., “Spiral defect chaos in large aspect ratio Rayleigh-Bénard convection,” *Phys. Rev. Lett.*, vol. 71, pp. 2026–2029, 1993.
- [44] MORRIS, S. W., BODENSCHATZ, E., CANNEL, D. S., and AHLERS, G., “The spatio-temporal structure of spiral-defect chaos,” *Physica D*, vol. 97, pp. 164–179, 1996.
- [45] OBERBECK, A., “Über die wärmeleitung der flüssigkeiten bei der berücksichtigung der strömungen infolge von temperaturdifferenzen,” *Ann. Phys. Chem.*, vol. 7, pp. 271–292, 1879.
- [46] PAUL, M. R., EINARSSON, M. I., FISCHER, P. F., and CROSS, M. C., “Extensive chaos in Rayleigh-Bénard convection,” *Phys. Rev. E*, vol. 75, p. 045203(R), 2007.
- [47] RAYLEIGH, L., “On convection currents in a horizontal layer of fluid, when the higher temperature is on the underside,” *Phil. Mag.*, vol. 32, pp. 529–546, 1916.
- [48] RUELLE, D., *Turbulence, Strange Attractors, and Chaos*. Singapore: World Scientific, 1995.
- [49] SCALABRIN, G., BETTIO, L., MARCHI, P., and STRINGARI, P., “A fundamental equation of state for sulfur hexafluoride (SF_6) in extended equation of state format,” *J. Phys. Chem. Ref. Data*, vol. 36, no. 2, pp. 617–662, 2007.
- [50] SETTLES, G. S., *Schlieren and shadowgraph techniques: visualizing phenomena in transparent media*. New York: Springer, 2001.
- [51] TANAKA, Y., NOGUCHI, M., KUBOTA, H., and MAKITA, T., “Thermal conductivity of gaseous methane and sulfur hexafluoride under pressure,” *J. Chem. Eng. Jpn.*, vol. 12, no. 3, pp. 171–176, 1979.
- [52] TOGNERI, R. and DESILVA, C. J. S., *Fundamentals of Information Theory and Coding Design*. Florida: Chapman and Hall/Crc, 2003.
- [53] ULYBIN, S. A. and BAKULIN, S. S., “The thermal conductivity of carbon dioxide at temperatures of 220–1300 K and at pressures up to 300 MPa,” *Teploenergetika*, vol. 24, no. 1, pp. 85–89, 1977.
- [54] VUKALOVICH, M. P. and ALTUNIN, V. V., *Thermophysical Properties of Carbon Dioxide*. London: Collet’s, 1968.

- [55] WILHELM, J., SEIBT, D., BICH, E., VOGELAND, E., and HASSEL, E., “Viscosity measurements on gaseous sulfur hexafluoride,” *J. Chem. Eng. Data*, vol. 50, pp. 896–906, 2005.
- [56] WOLF, A., SWIFT, J. B., SWINNEY, H. L., and VASTANO, J. A., “Determining Lyapunov exponents from a time series,” *Physica D*, vol. 16, pp. 285–317, 1985.
- [57] XI, H. and GUNTON, J. D., “Spatiotemporal chaos in a model of Rayleigh-Bénard convection,” *Phys. Rev. E*, vol. 52, pp. 4963–4975, 1995.
- [58] ZOLDI, S. M. and GREENSIDE, H. S., “Karhunen-Loève decomposition of extensive chaos,” *Phys. Rev. Lett.*, vol. 78, pp. 1687–1690, 1997.
- [59] ZOLDI, S. M., LIU, J., BAJAJ, K. M. S., GREENSIDE, H. S., and AHLERS, G., “Extensive scaling and nonuniformity of the Karhunen-Loève decomposition for the spiral-defect chaos state,” *Phys. Rev. E*, vol. 58, pp. R6903–R6906, 1998.